Strontium Mineralogy of the Ivigtut Cryolite Deposit, South Greenland

New insight into the isostructural minerals jarlite and jørgensenite

Per Alexander E. Danielsen

Master Thesis in Geosciences
Mineralogy, Petrology and Geochemistry
60 credits

Natural History Museum
Department of Geosciences
Faculty of Mathematics and Natural Sciences
UNIVERSITY OF OSLO

09/2023

Year 2023

Title: Strontium Mineralogy of the Ivigtut Cryolite Deposit.

Author: Per Alexander E. Danielsen

Supervisors: Henrik Friis (Natural History Museum, University of Oslo)

Tom Andersen (Natural History Museum, University of Oslo)

http://www.duo.uio.no/

Printing: Reprosentralen, Universitetet i Oslo

Acknowledgements

I would like to thank my supervisors, Henrik Friis and Tom Andersen, for their continuous support and their helpful guidance. I am especially grateful towards Henrik Friis, for introducing me to Ivigtut, a place that will forever hold my interest, both in terms of its mineralogy, but also in its cultural history. I will follow the future scientific development with sincere interest.

I would also like to thank Muriel Marie Laure Erambert for all the help and guidance with the electron-microprobe, and for helping me understand some of the problems which occur when analysing complex fluorides. Thanks to Nelia Castro for providing the necessary training for the SEM-EDS. Additional thanks to Hans Arne Nakrem, who showed me how to capture photographs of my thin-sections.

Lastly, I would like to thank my friends and family. My girlfriend Eini have been of tremendous moral support during the work on this thesis. My mother also deserves a special mention.

Abstract

On the southern shores of the Arsuk Fjord, lies Ivigtut, the home to what used to be the largest deposit of cryolite in the world. The locality was first discovered by western scientists in the early 19th century, and it immediately sparked the interest of research and industrialization. Throughout the late 19th century and early 20th century, the Ivigtut cryolite mine formed the basis for the global aluminium industry. The mining activity uncovered several rare aluminofluoride-minerals, with several of these being different types of Sr-aluminofluorides.

The goal of this thesis has been to enhance our understanding of the two isostructural Sr-aluminofluorides, jarlite and jørgensenite. The paragenesis and crystallization sequence of these two minerals have been investigated with the use of optical microscopy and scanning electron microscopy. This also provided the means to positively identify the two minerals. A more precise chemistry was obtained by electron probe microanalyzer, although the minerals proved to be highly chemically heterogenous. The $^{87}Sr/^{86}Sr$-ratio of stenonite and jørgensenite was measured with a multi-collector inductively coupled plasma mass spectrometer. The crystal structure of jørgensenite and jarlite was determined by single crystal X-ray diffraction and refined to a Final R_1 between 0.2 and 0.4 for 8 different samples.

The SXRD results were used to conduct a detailed site-assignment for jørgensenite and jarlite, which made it possible to propose a new general formula for the two minerals. A new definition of jørgensenite and jarlite is also proposed, based on their respective content of Mg at the *Na2*/*Mg*-site. This made the original Ba-criteria obsolete, and a Ba-analogue of jørgensenite is therefore proposed to be recognized as its own mineral. The petrological study proved that jørgensenite and jarlite formed due to the breakdown of celestine and/or strontian baryte, which alters the previously suggested crystallization sequence and mode of formation for these minerals. The $^{87}Sr/^{86}Sr$-signatures of stenonite and jørgensenite indicate that the cryolite deposit can be treated as a closed system during its evolution.

List of Abbreviations

Å, Angstrom, 10^{-10} m

BSE, Backscatter Electrons

BVS, Bond Valence Sum

CN, Coordination Number

CSS, Calculated Site Scattering

EDS, Electron Dispersive X-Ray Spectroscopy

EPMA, Electron-Probe Micro-Analyzer

GDB, Gardar Brown Dyke

OIB, Ocean-Island Basalt

PPL, Plane-Polarized Light

PV, Polyhedron Volume

REE, Rare Earth Element

RSS, Refined Site Scattering

SCLM, Sub-Continental Lithospheric Mantle

SEM, Scanning Electron Microscope

SXRD, Single Crystal X-Ray Diffractometer

WDS, Wavelength Dispersive X-Ray Spectroscopy

XPL, Cross-Polarized Light

Contents

1 Introduction

Within the time period between 1856 and 1987, scientist working on the cryolite deposit at Ivigtut faced the challenge of conducting research on a deposit which was slowly mined away. Today, the cryolite deposit is completely removed and the only remains of it found, are the empty quarry from which cryolite was extracted and waste rock dispersed around the former mining village. As a consequence, researchers working on this deposit today, face one of the greatest geological challenges there is; that of describing a quite unique deposit which no longer exists, and which have few true equivalents known in the world.

Most contemporary research have been focused on placing the deposit within the timeframe and within the evolution model of the Gardar alkaline igneous province. As a result, no true petrological and mineralogical work has been done on the deposit since the early 1990s. However, there still exists a lot of research potential related to petrological and mineralogical investigations, even though the deposit no longer exists.

The mineral jarlite was first described in 1933 by the Danish mineralogist Richard Bøgvad, and now, 90 years later, its crystal chemistry has not been completely defined. An important aspect of discovering new minerals is to describe them with such a level of detail, that we can with confidence, acknowledge that we understand them, and not only know of them. Our knowledge of jarlite, and its isostructural Na- and Ba-analogue jørgensenite, cannot be considered satisfactory, and these minerals are in need of a new, and detailed study. The purpose of this thesis is therefore to provide new insight into these minerals, and hopefully be able to establish a more detailed understanding of their crystal structure and crystal chemistry. Additionally, the intention is to bring into light some of the conditions that control the crystallization of these minerals, and to answer the question as to why these isostructural minerals often occur within the same paragenesis.

2 The History of Ivigtut

2.1 Introduction

Ivittuut is located in a valley on the southern shore of the Arsuk fjord in southwestern Greenland, with coordinates 61° 12´7´´ N and 48° 10´25´´ (Elbo, 1948; Ball, 1923). The name, Ivigtut or Ivittuut, stems from the Greenlandic language, and translates to “the place that is green” or “the place with plenty of vegetation” (Lloyd, 1953; Nordenskiöld, 1885). The name Ivigtut refers to the geological site, while Ivittut is the name of the place. The locality is foremost known for the occurrence of cryolite (Na_3AlF_6) and the industry which emerged, following its discovery in 1806. The occurrence of cryolite was from a geological perspective quite unique, especially considering the size of the deposit. However, cryolite have been reported from several deposits worldwide, with notable examples being; the Maderia deposit, Pitinga mining district, Brazil (Bastos Neto et al. 2009) and Katugin rare-metal deposit, Russia (Gladkochub et al. 2017), and Bailey (1980) gives examples of several more.

2.2 Description of the Deposit

The cryolite deposit occurred as a distinct oval-shaped, delineated pegmatitic body in relation with a granitic intrusion (Pauly and Bailey, 1999). The deposit was composed of multiple zones of different mineralogical compositions and was in its entirety 70 metres deep and 140 to 170 metres in diameter along its E-W and N-S axis, respectively. Figure 2.1 gives a description of the assumed shape and extent of the orebody, as viewed along a E-W axis. A small lens of pure cryolite, measuring approximately 50 meters in length, was originally exposed on the eastern part of the deposit (Pauly and Bailey, 1999). This lens, rested on a deeper and broader zone of siderite and cryolite, which was the main constituent of the orebody. Another zone of pure cryolite was located in the western part of the deposit at a depth of approximately 30 metres. It measured 150 metres in length and had an average thickness of 40 metres in width and 25 metres in height. This zone occurred between the siderite-cryolite zone and a lower lying zone of fluorite-cryolite. The cryolite-siderite and fluorite cryolite zone, rested on a zone of quartz and siderite (Pauly and Bailey, 1999).

Due to intensive mining in the timespan between 1865 and 1962, the cryolite deposit was completely mined out, and the former mine is now filled with water (Kruse, 2016). All that is left is the remains of waste piles and buildings. The following pages will contain a brief summary of the history of discovery and mining at Ivittut. This part is not intended to give the reader a thorough understanding of the historical relations between Denmark and Greenland, or the scientific evolution of the 19th century, but some aspects of it has been included for the sake of continuity in the storytelling. The intention behind this historical chapter is to give the reader an understanding of how the scientific research on Ivigtut developed in the early years and to provide the reader with the necessary foundation for understanding some of the difficulties occurring when doing geological work on the deposit.

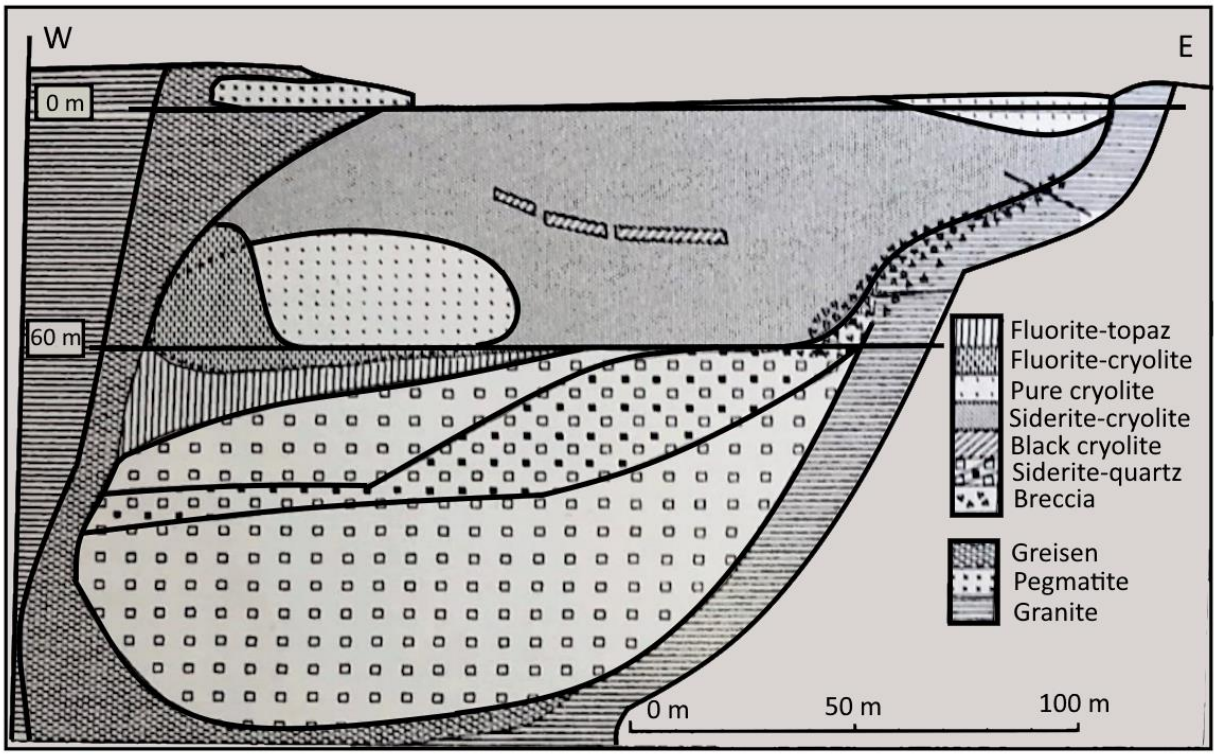

Figure 2.1: A simplified geological cross section of the deposit, as it may have looked before mining started in 1856. The originally exposed lens of cryolite, which was first discovered by Karl Ludwig Giesecke in 1806, can be seen at the easternmost part of the cross section. The dark-spotted zone on the westernmost part of the cross section is a small pegmatitic zone and should not be confused with the two zones of pure cryolite. Modified from Pauly and Bailey (1999).

2.3 The Discovery

The deposit was first discovered by Europeans in 1806 when it was visited by Karl Ludwig Giesecke (1761-1833) during his travels in Greenland (Johnstrup 1878; Pauly and Bailey, 1999). Cryolite had previously been known to the Eskimos of Greenland, who had used cryolite both as a fishing sinker and as dilutant of snuff (Nordenskiöld, 1885). Giesecke had been hired as a consultant to the Royal Greenland Trading Company to investigate the geology and search for interesting mineral occurrences in the southwestern part of Greenland (Kragh, 1995). Due to escalating tension between Britain and Denmark-Norway during the Napoleonic wars, Giesecke was stranded in Greenland for seven years and most of his collected material was sieged by British cruisers (Johnstrup, 1878). His collection was auctioned off in Edinburgh and bought by the Scottish mineralogist Thomas Allan (1777-1833) who recognized several samples of cryolite. During the early nineteenth century, cryolite was worth its weight in gold among collectors and Allan may have believed that he had made a good deal when he bought the collection for £ 40 (approximately £ 2,500 today), (Jonhstrup, 1878; Nordenskiold, 1885). However, when Giesecke returned to Scotland in 1813, he could report that he had found a massive occurrence of cryolite, measuring 100 times 50 fathoms (182 times 91 metres), (Nordenskiöld, 1885). Since then, cryolite has not been considered a mineralogical rarity.

Cryolite had been discovered prior to Gieseckes travels, but he was the first to correlate the Greenlandic mineral with its place of origin (Johnstrup, 1878). The mineral that was to become known as cryolite had first arrived in Europe in the early 1790's when it was transported to Denmark as a part of a shipment of Greenlandic goods by the Royal Greenland Trading Company. Due to its peculiar appearance, it was shown to Heinrich Christian Friedrich Schumacher (1757- 1830), a prominent professor at the Royal Chirurgical Academy in Copenhagen, who upon examination where in doubt whether it was a new mineral or just a piece of baryte (Ball, 1923; Kragh, 1995).

A closer examination of the mineral was undertaken by the Portuguese-Brazilian mineralogist José Bonifacus D'Andrada e Silva (1763-1838), accompanied by the Danish chemist and veterinarian Peter Christian Abildgaard (1740-1801), (Kragh, 1995). D'Andrada described the new mineral and named it after its whiteness, transparency and ice-like appearance, cryolite or "ice-stone" (Ball, 1923). Abildgaard tried to determine the chemistry of the mineral, and concluded that it contained fluorspar acid, aluminium oxide and potassium, which was soon proven to be wrong (Nordenskiöld, 1885). The correct chemical composition of cryolite was

first determined in 1823 when the Swedish chemist Jöns Jakob Berzelius (1779-1848) took an interest in it (Kragh, 1995). He determined the composition to be 24.4 % aluminium oxide, 44.25 % sodium oxide and 31.35% fluorspar acid (Berzelius, 1824), which result in the chemical formula Na_3AlF_6.

2.4 Commercial Exploitation

It would take another twenty years before experiments regarding the commercial use of cryolite began at full. In 1847, the Danish professor of Mineralogy at the polytechnic High School in Copenhagen, Johan Georg Forschammer (1794-1865), obtained a shipment of half a ton of cryolite. Having worked as a chemist in the porcelain industry, he wanted to investigate if cryolite could be used as a porcelain glaze (Kragh, 1995). His experiments failed, and the remaining cryolite was given to his assistant Julius Thomsen (1826-1909). Thomsen realized that cryolite could be used in the manufacturing of soda crystals (sodium-carbonate), a necessary component in the glass and soap industries. His experiments with production of soda from cryolite succeeded in 1849 and the Thomsen process was patented in 1852 (Kragh, 1995). The idea of Thomsen was to design a process of soda manufacturing that did not involve the use of sulphuric acid, as was the case with the already established Leblanc process. Thomsen's first step was to cause a reaction between cryolite and lime, which removed the fluorine through the precipitation of fluorite. The remaining sodium-aluminium-oxide was then carbonized by the introduction of carbon dioxide, and soda precipitated (Thomsen, 1862). The process proved to be effective, but Thomsen was unsure of its industrious potential, due to the believed scarcity of cryolite (Kragh, 1995). Fortunately for Thomsen, the geographer Hinrich Rink had recently returned from a geological expedition to Ivituut (Pauly and Bailey, 1999). Rink concluded in his report from 1852, that both the size of the exposed lens of cryolite and its purity was quite favourable for mining (Rink, 1852). Upon reading the report, Thomsen realised the potential of industrializing his process (Kragh, 1995).

Even though a potential mining operation at Ivittuut seemed profitable, the proposed soda-industry would still need a reliant supply of cryolite, and so far, no company could satisfy that demand. The Royal Greenland Trading Company had proven to be too unreliable, due to the insufficient amount of cryolite they were able to mine and sell (Kragh, 1995). Thomsen decided that he would have to equip his own mining expedition, with the financial backing of the businessman Carl Fredrik Tietgen, whom he had met in 1855 (Kragh, 1995). The first proper

mining expedition left Denmark on the schooner *Sønderjylland* in the summer of 1856 and extraction of cryolite at Ivittuut began the following August (Jarl, 1909; Pauly and Bailey, 1999).

The first shipment of cryolite was bought by the company Theob. Weber & Co., who needed soda to manufacture mirror glass, a newly established industry in Denmark (Jarl, 1909). Weber & Co. had also bought the right to use the patented Thomsen process from Tietgen in 1857 (Kragh, 1995). Due to technical problems regarding Weber & Co.'s factory in Southern Jutland, it was decided that a modernized factory had to be built (Kragh, 1995). The new factory, located in Copenhagen, was finished in 1859, and was named *Kryolithselskabet Öresund* (Jarl, 1909). Julius Thomsen was appointed technical director and shared the ownership with Weber & Co (Kragh, 1995). *Kryolithselskabet Öresund*, had been awarded a monopoly on the extraction of cryolite at its foundation in 1859, and with the new factory, they could process up to 2000 tons of cryolite each year (Kragh, 1995). Construction of a permanent mining camp at Ivituut began in the same period, and a permanent workforce was established (Pauly and Bailey, 1999).

During these early years, mining was concentrated on the exposed zone of pure cryolite (Pauly and Bailey, 1999). The purity of the raw material and the simplicity of the Thomsen process was the reason behind the profitable nature of the entire operation. The zone of pure cryolite became exhausted during the mid-1860's and the mining operation had to switch to the underlying ore-zone of siderite-cryolite (Pauly and Bailey, 1999). As a result, the workforce had to start selective mining and introduce new sorting procedures (Pauly and Bailey, 1999).

It was during the same time period, the company changed its name to *Cryolite Mine and Trading Company* (1864), and became a stock enlisted company (Ussing, 1908). Two thirds of the cryolite they mined were sold to *Öresund,* who held the monopoly on cryolite-refinement and trade in Europe, while the remaining one third were sold *Pennsylvania Salt Manufacturing Company*, who held the North American monopoly (Elbo, 1948). The price of soda fell during the late 1860's, because of the newly introduced Solvay process (Ussing, 1908). The Solvay process was developed in the early 1860s by the Belgian chemist Ernst Solvay (1838-1922) and proved to be a more efficient and economical way of producing soda, than both the Leblanc process and the Thomsen process. The main principle of the Solvay process is to carbonate a mixture of brine, limestone and ammonia, to give the products calcium chloride and soda (ammonia acts as a catalyst), (Kiefer, 2002). The invention of the Solvay process caused increasing concern for the future of the cryolite industry, something which led Weber & Co. to

put *Kryolithselskabet Öresund* up for auction in 1869 (Jarl, 1909). The company was bought by Gustav Adolph Hagemann and Vilhelm Jørgensen, two chemists that both had worked with the company in the years prior to the sale (Jarl, 1909). The new administration changed the name to *Öresund Chemical Factories*, as to open the possibility for expansion within the chemical industry.

Following the challenges caused by the falling soda market, *Öresund Chemical Factories* had to restructure its factory from the production of soda to the production of cryolite enamel (Kragh, 1995). The future of the Danish cryolite industry may have looked bleak, but only for a short period of time. In 1886, a patent for a newly developed method of producing aluminium was filed both in the US and in France simultaneously. The developers were the American chemist Martin Hall (1863-1914) and the French scientist Paul Louis Toussaint Héroult (1863-1914), and the method became known as the Hall-Héroult process (Ratvik et. al., 2022). This process was based on the electrolytic dissociation of bauxite in a bath of molten cryolite as a way to produce pure aluminium, where the cryolite acted as a flux. For each kilo of cryolite, ten kilos of aluminium could be produced (Jarl, 1909). This process revolutionized the production of aluminium, and the demand for cryolite slowly started to increase (Pauly and Bailey, 1999).

To achieve the transition into the new aluminium industry, *Öresund Chemical Factories* had to re-renew their factory. The effectiveness of the Hall-Héroult process was based on the purity of the cryolite. Great care had to be taken not to crush the cryolite into a too fine powder, which would render the separation of impurities, impossible (Jarl, 1909). This proved difficult due to the softness of the mineral, and it became necessary to install machinery that could extract impurities from the cryolite at a higher efficiency than the previous hand-sorting procedures (Ussing, 1908). Large investments were made in order to restructure the factory, and *Öresund Chemical Factories* evolved into one of the most modern mineral sorting facilities in the world (Jarl, 1909). Both magnetic separation of metallic minerals, and density separation using vibrating water-trays were installed (Ussing, 1908; Jarl, 1909). As a result of these investment, *Öresund* would also start selling silver-bearing galena as a by-product of the cryolite refining. From 1937 and 1964, about 500 tons of galena were sold (Pauly and Bailey, 1999).

2.5 The last years of the cryolite mine

During the early 20th century, aluminium had gone from being a metallic curiosity to an important commodity in the newly developed airplane industry. Aluminium had proven to be an excellent material for the construction of airplane hulls, due to both its strength and weight. With the rising airplane industry, both the value of cryolite and the production of it increased (Ball, 1923; Sørensen, 2007). With the rising demand of cryolite, several drilling programs were carried out during the 1910s and the 1920s, with the aim of determining the remaining content of cryolite and contribute to research regarding the geological nature of the deposit (Pauly and Bailey, 1999). The first drilling program, carried out between 1912 and 1915, found that a large body of presumably pure cryolite was located within the siderite-cryolite ore on the western side of the deposit (Pauly and Bailey, 1999). Initially, the find looked promising, but soon proved to be useless because of inclusions of fluorite and topaz. These minerals could not be separated from the cryolite in an economical way at the plant in Copenhagen. The zone was still mined, but most of the material was stockpiled or used as road-fillings.

The mining town developed and expanded during the early 20th century, and the community received its first telegraph station and electrical power plant in the 1920s (Sejersen, 2014). By 1948 the town had grown to contain 80 buildings, among these were shops, a hospital, barracks, store houses, two fire houses and a cinema (Elbo, 1948; Lloyd, 1953). They were all concentrated around the mining pit, which had reached a depth of 60 metres (Elbo, 1948). The workplace was hazardous, due to the intensive blasting procedures. Rock slabs, ejected from the blast, would fall all over the mining town and could cause serious harm to both the workforce and the buildings (Lloyd, 1953).

In 1940, *Öresund Chemical Factories* and *Cryolite Mine and Trading Company*, merged to form the partially state-owned company, *Kryolithselskabet Öresund A/S* (Elbo, 1948). The merger marked the end of a 75-year period of which Ivittuut had been regarded as an independent part of Greenland (Sejersen, 2014). From this time on, all the Danish governments profits would be funnelled back into the Greenlandic Society and the mining area was opened to the Greenlanders. The company stores started paying taxes to the Greenlandic government, and the inhabitants of Ivittuut became enlisted as Greenlandic citizens and was given voting rights in local elections (Lloyd, 1953). Before 1940, Greenlanders had been strictly forbidden from entering the premise (Lloyd, 1953). This socio-political and socioeconomic transition was caused by the outbreak of the second world war and 1940 also marks the year in which Germany

invaded Denmark. With the invasion of Denmark and with increasing submarine warfare in the Atlantic, trade to and from Greenland diminished. As a consequence, the mine had to be opened to the Greenlanders, so that the mine could be fully operational during the war.

Contrary to the abrupt end in communications between Greenland and Denmark, trade between North America and Greenland flourished. Approximately 250,000 tons of raw cryolite was sold to the US during the second world war (Elbo, 1948). The revenue earned from the US-Greenlandic trade of cryolite, ended up paying for all of the Greenlandic domestic expenses, practically shielding the Greenlandic economy from the war (Strøm Tejsen, 1977). In contrast to the US, most of Europe lost its source of cryolite and a synthetic version had to be introduced to meet the demands of the wartime industries (Elbo, 1948).

The introduction of synthetic cryolite, marked the beginning of the end of the Danish cryolite adventure. Natural cryolite was still in demand after the war, mostly due to the high cost of its synthetic equivalent, but the quantity of remaining cryolite was quickly diminishing (Lloyd, 1953). Mining at Ivittuut ended in 1962 after almost a hundred years of operation. The cryolite trade continued for another 25 years, with the extraction and processing of the lower ore grades that had been stockpiled, as well as mine-tailings (Kruse, 2016). The mine finally closed in 1987 after having produced 3.8 million tons of cryolite since 1865 (Pauly and Bailey, 1999; Sejersen, 2014).

3 The Geology of Southwestern Greenland

3.1 Introduction

The former Ivigtut cryolite deposit was hosted in the pegmatitic core of a metasomatized alkali, A-type granitic intrusion (Pauly and Bailey, 1999; Köhler et al., 2008). The Ivigtut granite was emplaced at a time when Southwestern Greenland experienced extensive magmatism, which is today found as a series of central-type igneous complexes. These complexes are collectively called the Gardar igneous province. Located along the southern coast of Greenland, the Gardar province is found between the North Atlantic Craton (Archean basement rocks) to the north, and the Paleoproterozoic mobile belt to the south (see Fig. 3.1).

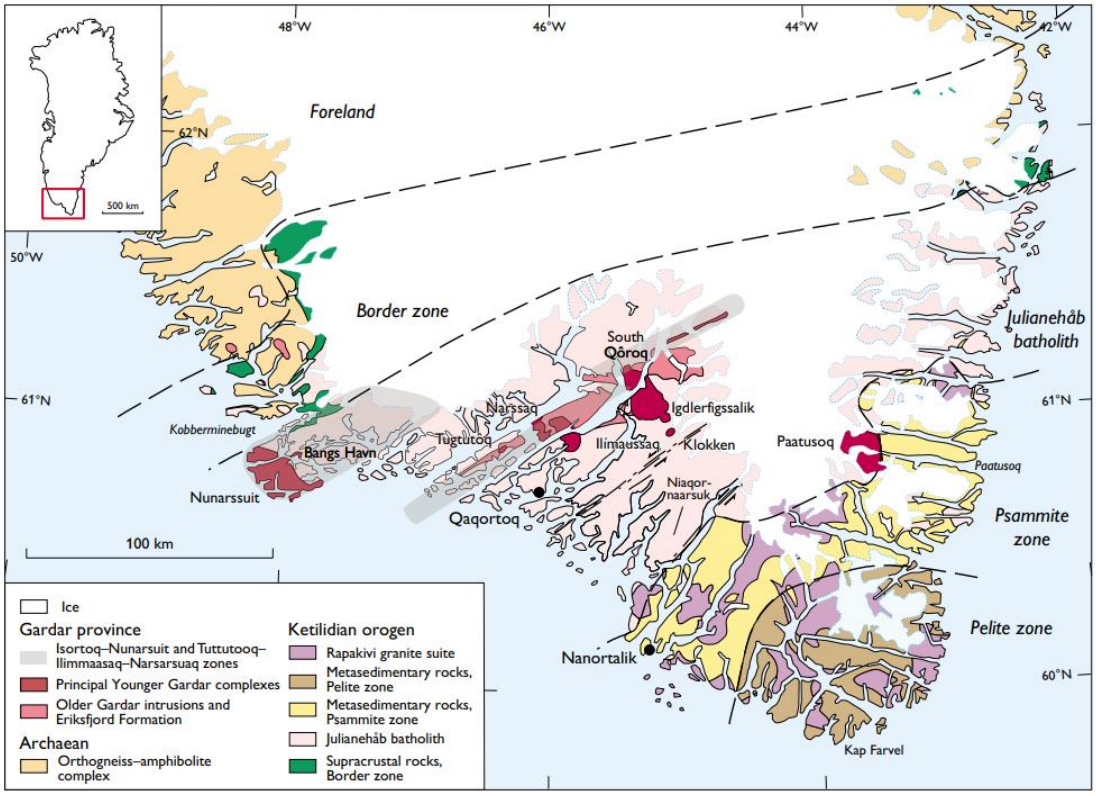

Figure 3.1. The Southwestern part of Greenland is made up of three distinct geological regions. The southernmost part is made up of the Psammite and Pelite zones of the Ketilidian orogeny, in addition to the Julianehåb batholith. This region lies adjacent to the border zone, which marks the transition to the Archean gneisses of Western Greenland. The Gardar province (red) is hosted within the Julianehåb batholith (pink). The figure is reused from Upton (2013).

3.2 The North Atlantic Craton

The North Atlantic Craton (NAC) consists of several subduction-related, Archean trondhjemite-tonalite-granodiorite terranes with ages between 3000 - 2800 Ma (Wittig et al., 2010). During the Phanerozoic, the NAC was dispersed and today fragments of it can be found along the Labrador-coast of Canada, in Southwest and East Greenland and in Northern Scotland (Bridgewater et al., 1973). The NAC has undergone several events of granulite- and amphibolite-facies metamorphism, meaning that most of the Archean basement is today recognized as orthogneisses and amphibolites (Bridgewater et al., 1973; Garde et al., 2002). The NAC of Southwest Greenland is found between the Naggsugtoqidian, Rinkian and Ammassalik mobile belts to the north and the Ketilidian mobile belt in the south, with the oldest rocks being the gneisses of the Godthåb region (Bridgewater et al., 1973; Chadwick and Garde, 1996).

3.3 The Ketilidian Orogeny

The Paleoproterozoic mobile belt was formed during the late Paleoproterozoic, between 1850 and 1720 Ma (Orosirian/Statherian period) and it is the remnants of the Ketilidian orogeny. The Ketilidian orogen is the youngest of three orogenic belts to have effected Greenland in the Paleoproterozoic (Lathinen et al., 2008). It was caused by the convergent plate-collision and subsequent subduction between the Archean basement of South-Greenland and an unknown oceanic plate (Garde et al., 2002). This event occurred as a part of the consolidation of the supercontinent Columbia, which is proposed to have existed until the early Mesoproterozoic (about 1500 Ma), (Meert and Santosh, 2017).

The peak of the Ketilidian Orogeny and subduction related magmatism, is marked by the emplacement of the Julianehåb batholith, located adjacent to the metasedimentary psammite- and pelite zones in the southernmost part of Greenland (see Fig. 3.1), (Garde et al., 2002; Upton, 2013). The Julianehåb batholith is a wedge-shaped, “Andean”-type, calc-alkaline continental arc, which grew in the timespan between 1855 - 1795 Ma. It is 100-200 km wide, and it covers an outcrop area of approximately 30,000 km^2 (Garde et al., 2002). The batholith is mainly composed of medium grained, granitic and granodioritic rocks, but it has a minor content of monzodiorites, tonalites and anorthosites. The magmatic origin of the plutonic rocks has been studied by Sr, Nd and Pb isotopes, and the magma was foremost mantle-derived but with an

uncertain addition of an Archean component, that varies throughout the batholith (Garde et al., 2002).

Lodged between the Julianehåb batholith and the foreland of the Archean craton is a 50 km wide region known as the Border Zone (Garde et al., 2002). This region is geologically composed of Ketilidian supracrustal, metasedimentary and metabasaltic rocks that has experienced varying degrees of metamorphism. These rocks lie unconformably on top of the Archean basement. The region experienced ductile deformation due to thrusting of the cover sequence during the Ketilidian, but the degree of deformation decreases northwards along a NW-SE-axis (Chadwick and Garde, 1996). As a result, well preserved supracrustal rocks of Ketilidian origin occur along the Northern border, in Midternæs and Grænseland area towards the Archean craton (Kalsbeek et al. 1990).

3.4 Geological overview of the Gardar Province

3.4.1 Introduction to the Gardar Province

The term “Gardar Formation” was first introduced by C. E. Wegmann in 1938, to describe the exposed unmetamorphosed, intrusive alkaline rocks and subaerial lavas mapped in southwestern Greenland (Wegmann, 1938). The first pioneering work on the province was however conducted 30 years prior, by the Danish mineralogist and geologist Niels Viggo Ussing (Ussing, 1912). Today, Gardar is no longer restricted to a single formation, but to a complex, rift-related, alkaline igneous province.

The Mesoproterozoic Gardar province developed due to a series of failed rifting-events in the timespan between 1350 and 1160 Ma, related to the breakup of the supercontinent Columbia (Upton, 2013). The rift-related magmatism caused the emplacement of 14 major central-type complexes, and several smaller intrusions and dyke swarms of variable compositions (Upton et al., 2003; Upton, 2013; Hutchinson et al, 2021). The rocks of the Gardar province have a variety of compositions, from alkali gabbros to silica-saturated peralkaline alkali-feldspar granites and silica-undersaturated agpaitic assemblages but sparse in rocks of intermediate compositions (Finch et al., 2001; Upton et al., 2003; Upton 2013;). Most of the Gardar magmatism occurred south of the border between the Border Zone and the Ketilidian basement rocks, except for the

Ivigtut granite and the Kûngnât- and Grønnedal-Ika complexes, which was emplaced within the Border Zone.

3.4.2 Eriksfjord Formation

The beginning of the Gardar period is still somewhat disputed. The oldest recognized rocks of Gardar period are the supracrustal lavas of the Eriksfjord Formation. The formation itself contains an approximately 3.4 km thick succession of aeolian and fluvial/lacustrine sandstones, and volcanic lavas, deposited on top of the Julianehåb Batholith (Upton et al., 2003; Andersen, 2013). The basalts of the Eriksfjord formation range from basaltic to tholeiitic to alkaline phonolitic and carbonatitic in composition and they are some of the geochemically more primitive rocks of the Gardar province (Halama et al., 2004). The sediments of the sandstones were most likely derived from the Julianehåb granite and were deposited in fluvial/lacustrine settings, related to graben formation that occurred during the Gardar rifting (Poulsen, 1964).

The age of the Eriksfjord formation is disputed. The lower lavas of the Mussartût group (Qassiarsuk) have been dated with Rb-Sr and Pb-Pb isochrons to around 1200 Ma, which contradict the field relationship between said lavas and early Gardar intrusions (Andersen, 1996; Andersen 2013). Two of the oldest Gardar complexes, North Qôroq and Motzfeldt, have both intruded the Eriksfjord formation and they both contain xenoliths which originates from the Eriksfjord formation (Upton et al., 2003). The Motzfeldt complex has been dated to 1,273 ± 6 Ma (McCreath et al. 2012), which means that the Mussartût group must have been emplaced much earlier. The difficulty of determining the age of the Eriksfjord formation stems from the fact that it has undergone low-grade thermal metamorphism, which is evident from the presence of epidote, and it has been subject to alteration due to post-magmatic hydrothermal processes (Piper, 1999; Andersen, 2008).

3.4.3 Gardar Magmatism

Two distinct phases of intrusive magmatism within the Gardar period have been identified based on U-Pb radiometric dating (Upton et al., 2003). Phase one occurred between 1330 and 1260 Ma and is referred to as the early phase (or older Gardar), while the late phase (younger Gardar) occurred between 1180 and 1140 Ma (Hutchison et al., 2021). The early Gardar phase is represented by the nepheline-syenites of the Grønnedal-Ika complex and the Igaliku complex, as well as the evolved A-type granite at Ivittuut and the rocks of the Eriksfjord formation (Pauly

and Bailey, 1999; Hutchison et al., 2021). The age of the Ivigtut intrusion has been determined to be around 1.27 Ga old (Köhler et al. 2007). The complexes of later Gardar are all found within the Ketilidian orogenic belt and comprises the highly alkaline complexes of Ilímaussaq and Nunarsuit, and most of the larger alkaline plutons (Hutchison et al., 2021). The two phases of magmatism differ not only in age but also into two separate rift-zones with different orientation. The mafic dykes of younger Gardar seem to have been emplaced along a NE-SW (also reported as E-W) oriented fault-system, while the mafic dykes of older Gardar follow a WNW-ESE trend (Upton et al., 2003; Upton, 2013; Hutchinson, et al., 2021).

3.4.4 The origin of the Gardar magmatism

The magmas of the Gardar alkaline province are believed to have been formed by the differentiation of partial melts derived from a heterogeneously enriched, sub-continental lithospheric mantle source (SCLM), (Upton et al., 2003; Köhler et al., 2009; Upton, 2013; Bartels et al., 2015; Hutchinson et al., 2021). During the breakup of the supercontinent Columbia, the crustal fracturing caused by the transtensional plate motion would have reduced the pressure acting on the underlying peridotite mantle (Upton, 2013). The reduced pressure initiated partial melting of the effected mantle rocks, which would have risen upwards through the crust. Even though this is a classical mechanism of alkaline magmatism, evident from modern examples such as the East-African Rift, it is not enough to explain the highly evolved character of some of the Gardar complexes (Marks and Markl, 2017). It has been argued that the strong enrichment of HFSE, LILE, REE and volatiles in the Gardar rocks (especially evident at Illímaussaq), may have been due to a pre-enriched mantle source, which was metasomatically altered during the Ketilidian orogeny (Köhler et al., 2009; Bartels et al., 2015). The mantle source could have experienced metasomatic alteration due to released fluids and melt fractions from the descending oceanic slab and caused crystallization of F-apatite, F-phlogopite and (Cl, F)-amphiboles (Köhler et al., 2009). These minerals would also have acted as sinks for HFSE, REE and LILE, and upon partial melting of the SCLM, the alkalis and volatiles contained in these minerals, would have been essential in controlling the solubility of HFSE in the melt fraction (Köhler, et al. 2009; Hutchinson et al., 2021).

Alternatively, several major and trace element studies of the Eriksfjord basalts and intrusive carbonatites and lamprophyres, have shown contrasting Sr and Nd isotope signatures to that expected of a SCLM-type magma source (Halama et al. 2003; Coulson et al., 2003). In both

cases, the isotope signatures resemble that of an enriched mantle plume similar to an OIB-type magma source. Based on these results, Coulson et al. (2003) suggested that the evolution of the early Gardar magmas could have developed during a two stage-process, in which partial melts originating from the asthenosphere was enclosed as metasomites within the SCLM, and then reactivated/remobilized during the rifting process. These results could point towards two different magma sources for the two distinct phases of Gardar magmatism. However, when working on the doleritic "brown dykes" of early Gardar age, Bartels et al. (2015), found that the isotope signatures of LILE and LREE correlate with a major influence of a SCLM-type component in the magma source.

3.5 The Geology of Ivittuut

3.5.1 Introduction

Nowhere is the F-rich nature of the Gardar magmatism as evident as at the former cryolite deposit in Ivituut. The deposit contained 12.3 million tons of cryolite ore and hosted a range of rare aluminofluorides, which had until their discovery at Ivigtut, not been known to science (Pauly and Beiley, 1999). The former cryolite deposit in Ivittuut was hosted in the pegmatitic-central part of an intrusive sodium-rich alkali, A-type granite. The intrusion was emplaced within the Ketilidian Ivigtut gneisses of the Border Zone, which can be further subdivided into three gneiss series, Fladland-, Nordland-, and Ikerasak gneiss series (Berthelsen, 1962).

3.5.2 Geological Setting

The Ivigtut granite is surrounded by an intrusion breccia, which in some parts are up to 60 metres wide (Berthelsen and Henriksen, 1975). The intrusion breccia contains angular fragments of the surrounding hornblende-biotite gneiss, trapped within a fine-grained matrix of granite (Berthelsen, 1962). The hornblende-biotite gneiss lies on top of older gabbro-anorthosite-bearing gneisses which is a part of the Nordland Gneiss series (Berthelsen and Henriksen, 1975). The gabbro-anorthosite gneisses are exposed about 100 metres east of the intrusion breccia, and in close vicinity to a second breccia. This second breccia is a cylindrical, cataclastic explosion breccia, named the Bunkebreccia, and it is connected with the Ivigtut granite at depth of 500 m (Berthelsen, 1962; Goodenough et al., 2000). The intrusion breccia was halted by the overlying segment of hornblende-biotite gneisses, which caused the latter to

deposit xenoliths within the intrusive body (Berthelsen, 1962). The Ivigtut granite would later penetrate the breccia and was emplaced according to the already established intrusive shape of the pipe (Pauly and Bailey, 1999).

The Ivigtut granite can be divided into three main segments. The top part of the granite is characterized by a chilled, porphyritic fine-grained granitic roof, which was the first part to solidify (Bailey, 1980). The underlying granite stock is divided into two segments, the top granite, which contained the cryolite deposit, and the deep granite, which continues downwards for at least 550 metres (Pauly and Bailey, 1999). The top granite has been extensively altered due to post-magmatic, metasomatizing fluids, but it can be recognized in unaltered parts as a porphyritic, hornblende-biotite, hypersolvus leucogranite (Bailey, 1980; Pauly and Bailey, 1999; Goodenough et al., 2000). The unaltered parts of the top granite were located along the walls of the intrusion, and evolved inwards into metasomatized, sericitized, albitized and greisenized variants, which surrounded the cryolite deposit (Bailey, 1980). The deep granite is a two-feldspar leucogranite and show the same type of alteration as the top granite, at all depths (Pauly and Bailey, 1999). It has been suggested that the Ivigtut granite evolved from a larger underlying, anorthositic complex, originating from a mantle derived magma source slightly contaminated by a crustal component (Goodenough et al., 2000)

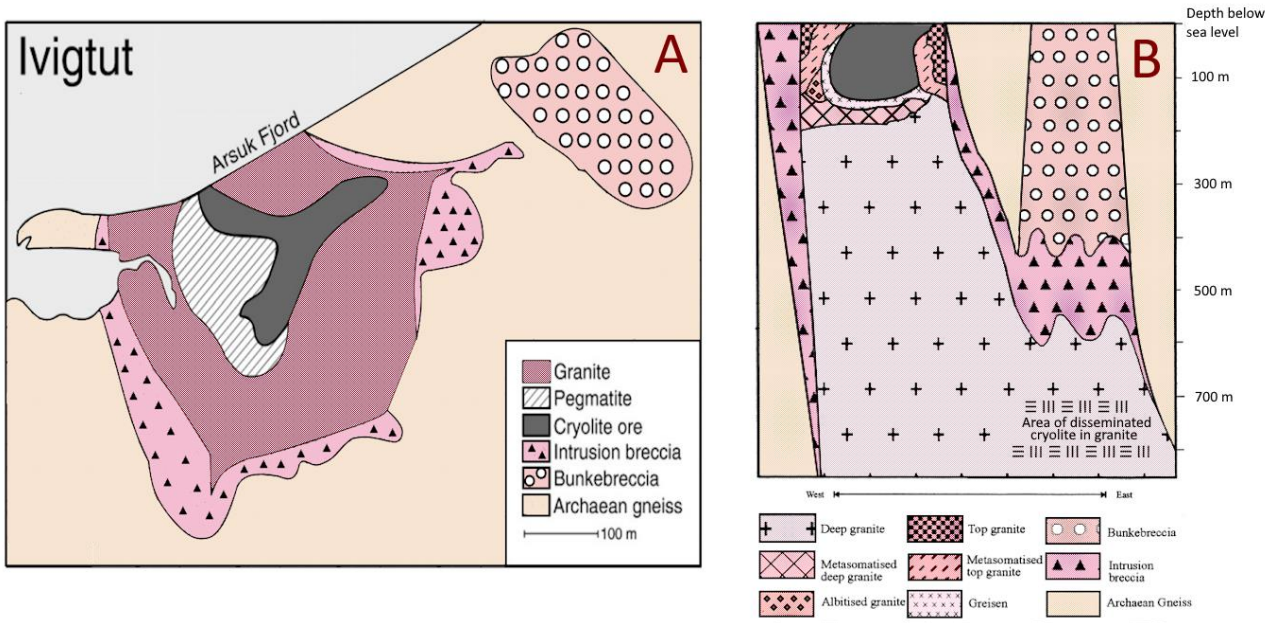

Figure 3.2: Presents cross-sections of the cryolite deposit. Fig. 3.2A present a horizontal cross-section, which shows the extent of the cryolite ore (dark grey colour) and the surrounding granite (dark pink) and intrusion breccia (pink). Fig. 3.2B presents a vertical cross-section, from sea level to a depth of 800m. The same colour scheme used in A have been used in B, with additional nuances for the different metasomatized parts of the granite. This figure shows that the Bunkebreccia is connected with the main granitic stock at a depth of around 500 m. 3.2A is modified and colorised after Köhler et al. (2008), and 3.2B is modified and colorized after Goodenough et al (2000). The colour scheme used is loosely taken from Upton (2013).

3.5.3 The formation of the cryolite deposit

The formation of the cryolite deposit began with the metasomatic alteration of the top granite, which is proposed by Pauly and Bailey (1999) to have been caused by cogenetic post-magmatic fluids which would have risen from a lower lying magma chamber. These post-magmatic fluids would have been trapped within the top-granite, due to the fine-grained roof-section. This proposal is however somewhat disputed, and Köhler et al. (2008) found when working on fluid inclusion and stable isotope data, that $\delta^{18}O$ and δD measured from fluid inclusions correspond to values expected from a meteoric fluid source. Regardless of the fluid source, the metasomatic alteration of the top granite caused extensive albitization, followed by greisenization, which released large amounts of Na into the system. The extensive metasomatism is also believed to have caused the formation of a hydrous aluminoflouride rich melt, which separated into siliceous, and fluoride melt fractions (Pauly and Bailey, 1999). The F-rich melt fraction in combination with the released Na from the greisenization, developed into the cryolite deposit.

This formation hypothesis is however somewhat disputed, and Goodenough (2000), Köhler et al. (2008) and Hutchinson et al. (2019), argue that it seems more likely that the origin of the cryolite deposit can be attested to the mixing between a reduced CO_3^{2-} and F-bearing fluid, with a highly saline, meteoric brine. Their arguments rest on a wide variety of evidence, which will be further discussed in Section 7.7.

3.5.4 Pauly and Baileys three stage formation theory

Pauly and Bailey (1999) proposed that the cryolite deposit evolved during three separate stages.

The first stage can be identified as the stage in which the main units of the deposit formed, the siderite-quartz and the siderite-cryolite units. These units consolidated from the released fluids/melt fractions generated during the metasomatic alteration of the top granite (Pauly and Bailey, 1999). The formation of these units caused significant brecciation of the wall-rock, which is evident from the granitic xenoliths entrapped within. The xenoliths showed no evidence of having reacted with the host material, which was interpreted to be due to the plastic and viscous nature of the siderite-cryolite mass. This idea is further elaborated by the presence of a banded/layered structure within the siderite-cryolite unit (Pauly and Bailey, 1999).

Stage two is distinguished by a series of pneumatic explosions that caused the collapse of the already crystallised cryolite roof and the crystallization of cryptocrystalline topaz and colloform/botryoidal fluorite (Pauly and Bailey, 1999). This resulted in the formation of two additional units within the deposit, the fluorite-topaz and the fluorite-cryolite units. The topaz is believed to have been formed by the breakdown of chiolite ($Na_5Al_3F_{14}$), in combination with the residual fluids from stage 1 (Pauly, 1992). The residual fluids are believed to have been especially rich in Ca, which in combination with F from the breakdown of chiolite, caused the crystallization fluorite (Pauly, 1992). As a result of the precipitation of fluorite and topaz, the remaining fluids became increasingly fractionated and enriched in LILE, and began precipitating complex hydrous aluminoflourides such as jørgensenite, jarlite, bøgvadite and weberite (Pauly and Bailey, 1999). The crystallization of these minerals both occurred within the fluorite units and in fissures generated during the explosions (Pauly, 1993).

The third stage is marked by filling of cavities and fissures by secondary aluminofluorides such as pachnolite ($NaCaAlF_6 \cdot H_2O$), thomsenolite ($NaCaAlF_6 \cdot H_2O$), and hydrokenoralstonite

($Na_{0.5}(Al, Mg)_2(F,OH)_6 \cdot H_2O$) (Pauly and Bailey, 1999). The cavities and fissures developed during the last part of the second stage, as a consequence of both crystallization/cooling induced contraction related to the consolidation of the fluorite-cryolite unit, and a sudden release of water vapour. The released fluid carried debris and fragments from the surrounding units, and it caused the crystallization of prosopite and a new generation of cryolite in several vertical fissures throughout the deposit, which was found as brecciated veins (Pauly, 1992; Pauly and Bailey, 1999).

4 Sr-Mineralogy

4.1 Introduction

Mindat.org list 17 minerals as having the Ivigtut cryolite deposit as their type-locality. Out of these 17 minerals, six are rare Sr-aluminofluorides that, with the exception of jarlite, have never been found anywhere else in the world. These minerals are acuminite ($Sr[AlF_4(OH)(H_2O)]$), bøggildite ($Na_2Sr_2Al_2(PO_4)F_9$), bøgvadite ($Na_2SrBa_2Al_4F_{20}$), jarlite ($Na_2(Na, Sr, \square)_{14}Al_{12}(Mg, \square)_2F_{64}(OH, H_2O)_4$), jørgensenite ($Na_2(Sr, Ba)_{14}Na_2Al_{12}F_{64}(OH, F)_4$) and stenonite ($Sr_2Al(CO_3)F_5$). These minerals are not only interesting, mineralogical oddities but could also be crucial to understanding the complex evolutionary history of the former cryolite deposit.

Table 4.1. The six Sr-aluminofluorides from Ivittuut presented with their chemical formula and principal sources.

Mineral	Chemical Formula	Principal Source(s)
Acuminite	$Sr[AlF_4(OH)(H_2O)]$	Pauly and Petersen (1987); Andersen and Ploug-Sørensen (1991)
Bøggildite	$Na_2Sr_2Al_2(PO_4)F_9$	Pauly (1956); Hawthorne (1982)
Bøgvadite	$Na_2SrBa_2Al_4F_{20}$	Pauly and Petersen (1988); Balić-Žunić (2014)
Jarlite	$Na_2(Na, Sr, \square)_{14}Al_{12}(Mg, \square)_2F_{64}(OH, H_2O)_4$	Bøgvad (1933); Hawthorne (1983); Pauly and Nielsen (1992)
Jørgensenite	$Na_2(Sr, Ba)_{14}Na_2Al_{12}F_{64}(OH, F)_4$	Pauly et al. (1997); Hawthorne and Burns (1997)
Stenonite	$Sr_2Al(CO_3)F_5$	Pauly (1962); Hawthorne (1984)

The following pages are intended to give a short introduction and description of the four Sr-minerals jørgensenite, jarlite, stenonite and bøgvadite, as they have been described in the literature. A thorough introduction of acuminite and bøggildite have been left out, since these minerals will not be important for this thesis.

4.2 Jarlite

Jarlite is a strontium aluminofluoride mineral, with the chemical formula $Na_2(Na, Sr, □)_{14}Al_{12}(Mg, □)_2F_{64}(OH, H_2O)_4$, (Hawthorne 1983). It was first described in 1933 by Richard Bøgvad as a result of a close examination of some previously discovered columnar aggregates of an unknown mineral. From material provided by Carl Fredrik Jarl, an engineer who worked at Øresunds Chemiske Fabriker, Bøgvad determined the unknown mineral to be new to science and named it in honour of the provider of the material (Bøgvad, 1933).

Jarlite was found as columnar, fan-shaped aggregates in cavities filled by thomsenolite. It is colourless or white, but it can be found with a brown discolouration due to a thin rust-coating. The lustre of jarlite is vitreous and its hardness is slightly higher than four (Bøgvad, 1933). It has no preferred directions of cleavage, making the fractures uneven. It shows no sign of pleochroism and is colourless in transmitted light. The maximum birefringence is low, with a $\delta = 0.007$ (30μm), which result in the mineral having an interference colour of first order grey/white. This is a common feature of most of the aluminofluorides.

Jarlite crystallizes in the monoclinic crystal system, and its crystal structure has the symmetry of the space group C2/m. The crystal structure of jarlite was first properly described and solved by modern standards in 1984 by F. C. Hawthorne (1983). He refined the crystal structure with a residual R index of 5.3% for 1027 reflections. The dimensions of the unit cell were determined to be, $a = 15.942$, $b = 10.821$, $c = 7.241$ Å, with $\beta = 101.86°$. The crystal structure of jarlite is based on Al, Na and Mg sheets. These sheets are formed by corner-sharing of Al- trimers ($[Al_3F_{16}]^{7-}$) and chains of $[MgNaF_8O_2]$ (Hawthorne, 1983). Adjacent layers of these 6-coordinated cations are connected through intersecting sheets of trimers of 10- and 9-coordinated Sr-atoms, positioned at the corners and centred at c-face of the unit cell (Hawthorne, 1983). The crystal structure of jarlite can be seen in Fig. 4.1. Figure 4.1a shows the layers of $[Al_3F_{16}]^{7-} + [MgNaF_8O_2]$, while Fig. 4.1b shows the entire unit cell as projected along the c-axis.

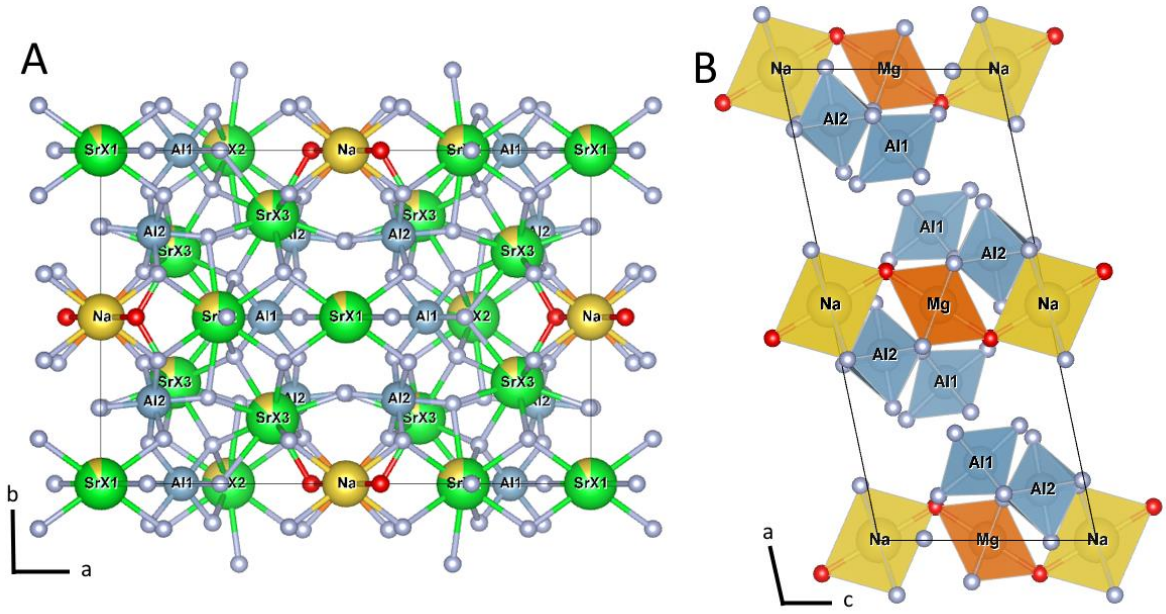

Figure 4.1: The crystal structure of jarlite. Figure A) shows the entire unite cell projected along the c-axis. Notice how the *Sr2*- site is partially hidden behind the F-atom connected to the *Al1*-site. The unnamed grey atoms are fluorine. Figure B) shows the layers of $[Al_3F_{16}]^{7-}$ + $[MgNaF_8O_2]$, projected along the b-axis. The *Sr1*-site from figure A) is located perpendicular to the plane, directly above the Mg-position and connected to the Al-octahedrons.

Jarlite occur as flat, fan-shaped crystal aggregates which can be found in cavities, but also as massive, columnar aggregates in relation with baryte. Pauly (1993) argues that the occurrence of jarlite in the cryolite deposit is due to two different crystallization events. The first event occurred at a time when Sr-Ba rich fluids became trapped within the main body of the fluorite-bearing masses. In the fluorite-cryolite and fluorite zones, jarlite crystallized as cm-sized inclusions from this entrapped fluid. It has been estimated that around 2000 tons of jarlite crystallized during this event (Pauly, 1993).

The second event was caused by the mixing between Sr-Ba rich fluids and fractured material of topaz-cryolite in five distinct fissures. The fissures were caused by the explosive events during the second stage of the deposits formation and was located within a solid body of cryolite. The length of the fissures were several metres, with the longest being 15 metres. The Sr-Ba rich fluid is believed to have been a part of the same fluid as in the first event. Jarlite was formed together with bøgvadite and baryte, due to dissolution of cryolite caused by the

intruding fluid. This replacement process caused the jarlite to crystallize as radiating and columnar aggregates together with baryte, due to the "gel-like" state of the fluid (Pauly 1993).

4.3 Jørgensenite

Jørgensenite is a rare strontium aluminofluoride, with the chemical formula $Na_2(Sr, Ba)_{14}Na_2Al_{12}F_{64}(OH, F)_4$. It was first described in 1997 by Pauly et al. (1997), and its discovery was related to previous work conducted on core-and mantle-features of some jarlites by Pauly and Nielsen (1992). They found that certain crystals of jarlite contained a Mg-rich mantle and a Mg-poor, but Ba-rich core. The core-feature thus proved to be a new mineral to science, and it was named after the founder of the cryolite company Vilhelm Jørgensen (Pauly et al., 1997).

Jørgensenite is colourless or white, with a vitreous lustre. The hardness of the mineral is between three and four, and it fractures unevenly with no preferred cleavage directions. It shows no sign of pleochroism, and it is colourless in transmitted light (Pauly et al., 1997). Its maximum birefringence is $\delta = 0.006$, with a maximum interference colour of first order grey. Its optical properties therefore make it indistinguishable from jarlite, but an optical boundary can be distinguished with crossed polars when the two minerals are adjacent to each other (Pauly et. al. 1997).

The crystal structure of jørgensenite was solved by F.C. Hawthorne and Peter C. Burns (1997), with a residual R index of 7.4% for 1632 reflections. The dimensions of the unit cell were determined to $a = 16.059$, $b = 10.974$, $c = 7.277$ Å, with $\beta = 101.70^{\circ}$. Jørgensenite crystallizes in the monoclinic crystal system and its crystal structure has the symmetry of C2/m. The crystal structure of jørgensenite is isostructural with that of jarlite, with the notable difference that jørgensenite contains a *Na*2-site fully occupied by Na, in contrast to the identical *Mg*-site in jarlite, which is partially vacant, and partially filled by Mg (Pauly et al, 1997). However, there do seem to be some inconsistencies in what truly defines a jørgensenite and Hawthorne and Burns (1997) also seem to propose that the Ba-content should exceed the Sr-content at the *Sr2*-site. This means that the difference between jarlite and jørgensenite could be governed by two criteria, (1) the Na-content needs to exceed the Mg-content at the *Na2*-site, and (2) the Ba-content needs to exceed the Sr-content at the *Sr2*-site.

The crystal structure of jørgensenite can be seen in Fig. 4.2. Figure 4.2a shows how the Al and Na octahedrons form the same type of layer as in the jarlite structure. Figure 4.2b shows the entire unit cell projected along the c-axis.

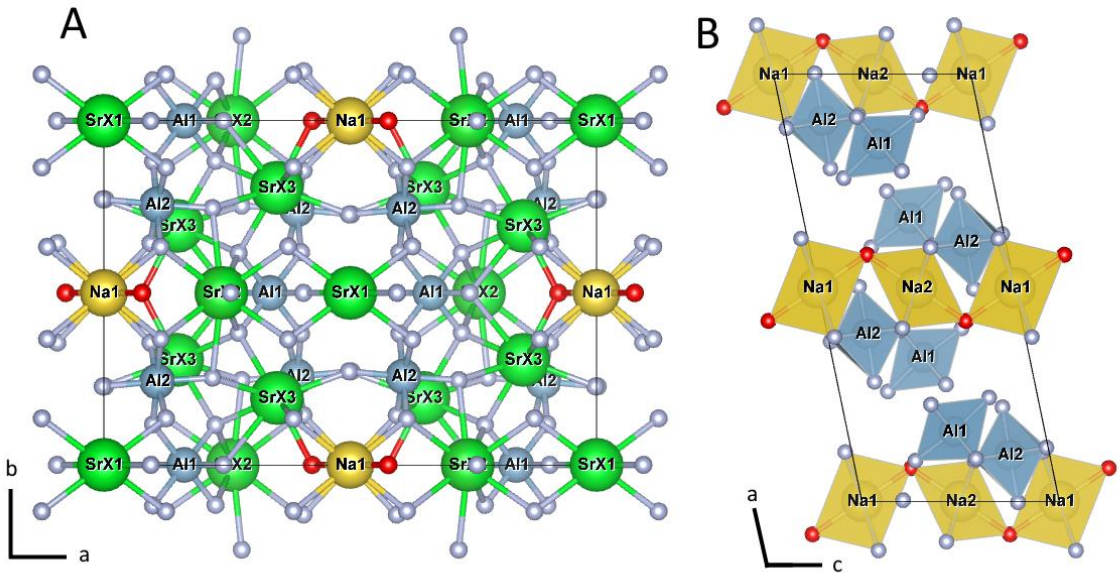

Figure 4.2: Jørgensenite is isostructural with jarlite, as is evident if comparing figure 4.2A with figure 4.1A. The main difference between the two structures can be seen in figure B, as the *Mg*-site has been substituted with a *Na2*-site.

Jørgensenite occurs as fan-shaped crystal aggregates in the same type of fissure fillings as jarlite. In these fissure fillings, jørgensenite is often overgrown by jarlite resulting in the core- and mantle-features as reported by Pauly and Nielsen (1992). The isostructural relationship, the chemical similarity and the occurrence, indicate that there may be some form of solid solution between jørgensenite and jarlite (Pauly et al. 1997). During the initial analysis of the core- and mantle-features, Pauly and Nielsen (1992), found that the core and mantle showed an optical continuity which indicate uninterrupted growth. They explained it as a feature of a temperature or pressure induced transition from a disordered to an ordered state (Pauly and Nielsen, 1992). Since the core-feature is now identified as its own mineral, it is possible that the optical continuity is caused by a chemical transition from jørgensenite to jarlite. This is indicated by the Mg-content of the type-jørgensenite (0.46 apfu) which is a significant amount compared to the idealized formula (Pauly et al., 1997).

4.4 Stenonite

Stenonite is a rare carbonate aluminofluoride mineral, with the mineral formula $Sr_2Al(CO_3)F_5$. It was first described by Hans Pauly (1962), who identified the new species from samples collected at the cryolite plant in Copenhagen. Pauly named the new mineral after the Danish scientist Nicolaus Steno, not because of the latter's involvement with Ivigtut, but solely as a tribute to his scientific achievements within the field of crystallography and mineralogy (Pauly 1962).

Stenonite is white or colourless and has a vitreous lustre. Its hardness is between 3 and 4, and it has three good cleavage directions that causes parallelepipedic fractures (Pauly 1962). The maximum birefringence is $\delta = 0.086$ (30μm), meaning that its interference colours is in the higher orders. This characteristic makes it easier to identify stenonite in thin sections, compared to the other aluminofluorides.

Stenonite crystallizes in the monoclinic crystal system and its crystal structure has the symmetry of the space group $P2_1/n$ (Hawthorne 1984). It is seldom found as euhedral crystal and more commonly found as anhedral grains (Pauly 1962).

The crystal structure of stenonite was solved by F. C. Hawthorne (1984). He found the unit cell parameters to be *a* = 5.450Å, *b* = 8.704Å, *c* = 13.150Å, with β = 98.72°. The crystal structure was refined with a residual R index of 6% for a total of 1219 reflections (Hawthorne 1984). The crystal structure of stenonite is based upon isolated clusters of $[AlCO_3F_5]^{4-}$, where the Al-F/O octahedron is connected to the carbonate group through corner-sharing of one oxygen-atom. These isolated clusters are connected in a three-dimensional network, by two different Sr-positions, one 8- and the other 9-coordinated (Hawthorne, 1984). Figure 4.3 shows the crystal structure of stenonite, viewed along the a-axis.

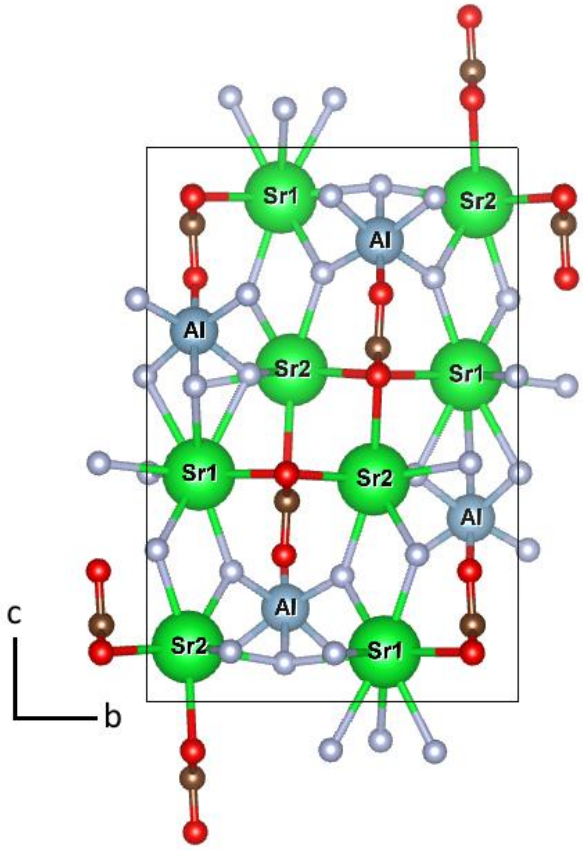

Figure 4.3: The crystal structure of stenonite, view along the a-axis.

Stenonite commonly occur together with jarlite, weberite and pyrite, but also the secondary aluminofluorides, thomsenolite, pachnolite, prosopite and hydrokenoralstonite. Euhedral crystals of pyrite seem to be a diagnostic feature of the paragenesis, and Pauly (1962) states that it almost always occurs together with jarlite.

The occurrence of stenonite in Ivigtut is proposed to have been formed during the latest stage of the formation/alteration of the deposit. At this stage, Sr, Mg, Ca and S were introduced into the system, which subsequently caused the alteration of cryolite into jarlite and siderite into stenonite, pyrite and hematite. The alteration of siderite into stenonite is marked by brecciation. This alteration is proposed to have taken place in the border-zone between the cryolite-siderite part and the siderite-fluorite part of the deposit (Pauly, 1962).

4.5 Bøgvadite

Bøgvadite is a rare barium aluminium fluoride, with the chemical formula $Na_2SrBa_2Al_4F_{20}$. It was first described in 1988 by Pauly and Pettersen (1988), but it was found in 1933 by Richard Bøgvad during his investigations of jarlite, whom the mineral is named after.

Pauly and Pettersen (1988) found bøgvadite as rectangular crystals with corroded surfaces, in the central parts of larger radiating aggregates of jarlite. It is white or colourless and have a vitreous lustre. It is transparent in transmitted light. Its streak is white, and it has a hardness between three and four. The crystals showed no signs of any preferred cleavage directions, and their fractures were irregular.

Pauly and Pettersen believed that bøgvadite crystallizes in the orthorhombic crystal system and they proposed that its crystal structure had the symmetry of space group *Pnmn* or *Pn2n*. However, the crystal structure of bøgvadite was recently solved and refined by Balić-Žunić (2014), who found that bøgvadite crystallizes in the monoclinic crystal system and its crystal structure has the symmetry of space group $P2_1/n$. The unit cell was determined to be a = 7.134 (1), b = 19.996 (3) and c = 5.3440 (8) Å, with β = 90.021 (1)°. The crystal structure of bøgvadite is based upon infinite, zig-zag chains of AlF_6-polyhedrons which are interconnected with infinite chains of Na-F. These two chains form a double layered structure, with 10-coordinated Sr-positions located within it. Individual double layers are interconnected by 12-coordinated Ba-positions (Balić-Žunić 2014).

Bøgvadite was found to occur together with baryte, jarlite, hydrokenoralstonie, thomsenolite, fluorite, topaz and an unidentified K-mica, with the latter occurring as bands transecting the investigated sample. Baryte was found within, what was interpreted by Pauly and Pettersen (1988) to be the outline of former bøgvadite crystals. Within this outline, baryte was found both as “patches” and as smaller aggregates of elongated crystals. They suggested that baryte had formed as pseudomorphs after bøgvadite, and that this relationship was due to a replacement reaction caused by the introduction of sulphate by an intruding fluid.

Pauly and Pettersen (1988) erroneously assigned bøgvadite to the orthorhombic crystal system. The reason behind this error, seems to have been that bøgvadite often appear with a twin parallel to the (001) mirror plane. Balić-Žunić (2014), argues that the frequent presence of this twin, could indicate that bøgvadite may have originally formed as a high-temperature orthorhombic polymorph which underwent a transition into the monoclinic structure upon cooling. This

would mean that the precursor to bøgvadite may have crystallized during a high temperature stage of the formation of the deposit.

5 Method

5.1 Sample Collection

None of the samples included in this research have been collected by the author of this thesis. Due to the related expenses and uncertainty regarding the COVID-19 situation, a fieldtrip to Ivituut was not possible in the timeframe, in which this research concurred. This was of course unfortunate, but due to the nature of this research project and the state of the locality (as described in section 2), it was deemed acceptable.

Samples PAD-IG001, PAD-IG002, PAD-IG003, PAD-IG006, PAD-IG009, PADIG012, were original collected by the late Steen Ahrenkiel at the cryolite plant in Copenhagen. These samples were donated to Professor Henrik Friis, at the Natural History Museum in Oslo, who passed these on to this project. The rest of the samples were all provided by Friis, who had collected them during his travels to Ivituut. These samples originate from mine tailings left by the company after the mine was abandoned in 1987.

Some work had already been conducted on some of the samples. A thin section of sample PAD-IG012 had already been made on the request of S. Ahrenkiel, and the thin section was incorporated into this project. Due to his strong interest regarding this locality, H. Friis had already collected jarlite/jørgensenite single-crystals from samples PAD-IG022, -23, -24, -25 and he had obtained crystal structure data from these. These datasets were passed on to this project, but they were re-analysed by the author.

Table 5.1: The different analyses performed on the samples

Sample Nr.	Optical	Thin section	SEM	EPMA	S-XRD	Provenance
PAD-IG001	X	X	X	X		S. Ahrenkiel
PAD-IG002	X	X	X	X		S. Ahrenkiel
PAD-IG003	X	X	X			S. Ahrenkiel
PAD-IG004	X	X	X			H. Friis
PAD-IG005	X	X	X	X	X	H. Friis
PAD-IG006	X	X	X	X	X	S. Ahrenkiel
PAD-IG007	X	X	X	X	X	H. Friis
PAD-IG008	X	X	X			H. Friis
PAD-IG009	X	X	X			H. Friis
PAD-IG010	X	X	X	X		S. Ahrenkiel
PAD-IG011	X	X	X	X		H. Friis
PAD-IG012	X	X	X			S. Ahrenkiel
PAD-IG013	X				X	H. Friis
PAD-IG014	X					H. Friis
PAD-IG015	X				X	H. Friis
PAD-IG016	X					H. Friis
PAD-IG017	X					H. Friis
PAD-IG018	X					H. Friis
PAD-IG019	X					H. Friis
PAD-IG020	X					H. Friis
PAD-IG021	X					H. Friis
PAD-IG022	X				X	H. Friis
PAD-IG023	X				X	T. W.
PAD-IG024	X				X	H. Friis
PAD-IG025	X				X	H. Friis
Pad-IG026					X	H. Friis

5.2 Thin Sections

Samples PAD- IG001 through PAD-IG011, were chosen as suitable candidates for closer examination, and it was subsequently decided to make thin sections from these. The reasoning behind this decision was based on the observation that these 11 samples contained different textures and mineral paragenesis. Suitable cross-sections were chosen based on a visual determination of the textural direction in the samples. Cross-sections were cut by a diamond-saw, as to create smaller blocks of the rock-samples, which the thin-sections were to be made from. The surface of interest on the small blocks were digitally recorded with the use of Nikon

Super Coolscan 4000 scanner. An image of sample PAD-IG006 is presented as figure 5.1, to show the type of texture that was of interest when selecting candidates for thin sections.

Figure 5.1: Sample PAD-IG006 after it had been sawed. The distinctive textural feature immediately sparked interest.

The blocks sawn from sample PAD-IG001 through PAD-IG011 were sent to Vancouver Petrographics in Canada, who made thin sections from these. Most of the thin sections were polished down to the standard thickness of 30 μm, but some of them show signs of being significantly thicker. The thin sections were not treated by any chemicals, and they were investigated with a Nikon Labophot2-polar, petrographic microscope at NHM, Økern, Oslo. All of the images were captured with a Leica MC170HD camera fitted on a Leica DMPL petrographic microscope.

5.3 Scanning Electron Microscope (SEM)

The samples were analysed with a Hitachi S-3000N Scanning Electron microscope (SEM), equipped with a backscattered electron detector and a Bruker XFlash 5020 energy dispersive X-ray detector (EDS). The instrument is located at the Natural History Museum, Oslo. Variable pressure mode at 10 Pa was used, since the thin-sections were not carbon-coated during this stage of the research. An acceleration voltage of 15.0 kV and a beam current of roughly 50 μA was used during the research.

Semi-quantitative chemical data was obtained by the use of the EDS-detector and approximately 40 EDS-points were collected for each sample. For each point the EDS-spectra were quantified and saved as atomic percentages, together with an image of the area in which the point is located. This technique was mainly applied to identify the mineral paragenesis of the samples. All minerals were identified by comparing the reported ratio of chemical elements with that of the literature. The SEM also proved to be a viable tool to investigate textures, such as chemical zonation. Because of the variable pressure mode, these textures were often diffuse, and the full extent of the density contrast between the chemically distinct zones were not recorded until the thin sections were studied with the electron microprobe.

5.4 Electron Probe Micro-Analyzer (EPMA)

To gain a more accurate insight into the chemistry of the Sr-minerals, it was decided that samples PAD-IG001, PAD-IG002a/b, PAD-IG005, PAD-IG006, PAD-IG007, PAD-IG010 and PAD-IG011, should be investigated with an Electron Probe Micro-Analyzer (EPMA). The EPMA collects high-quality quantitative chemical data, with a greater accuracy than the SEM. Like the SEM, the EMPA is a non-destructive technique.

The thin sections were coated in carbon, as to inhibit electron charging by application of a conductive layer. The electron microprobe analysis was performed on a Cameca SX100 electron microprobe with five wavelength dispersive spectrometers (WDS), at the Department of Geosciences, University of Oslo.

The following standards were used for the calibration of the elements of interest; Al_2O_3 (Al), $NaAlSi_3O_8$ (Na), $BaSO_4$ (Ba), CaF_2 (F), $SrSO_4$ (Sr), MgO (Mg), $CaSiO_3$ (Ca). The analysis was performed with all five WD-spectrometers (SP). Al, Sr and Na were analysed with TAP-crystals on SP1 (Al, Sr) and SP5 (Na). F and Mg were analysed with a LTAP-crystal on SP2. K, Ca and Ba were analysed with LPET-crystals on SP3 (K, Ca) and SP4 (Ba).

The analysis was performed with a beam-current of 10 nA and a beam-diameter of 20 μm. The count time was set to 10 seconds. The low beam-current and broad beam-diameter had to be used, as to reduce the damaged caused onto the material by the electron beam.

5.4.2 Problems

Acquiring a precise chemical analysis of light elements (atomic number 4 to 9) in minerals have been a well-known problem for decades. Even with the introduction of new types of reflective crystals and matrix corrections, the problem still persists in certain material (Raudsepp, 1995). It became evident during the preliminary EPMA-analysis of jarlite/jørgensenite, that this was the case. Fluorine is the heaviest of the light elements, but still a problematic element to analyse.

The main problem is caused by the x-ray peak of fluorine, and both its position and shape can vary for different minerals (Solberg, 1982). This variation is caused by the Kα emissions dependency on the valence electrons in light elements. This means that the crystal structure of the mineral and the bonding environment of fluorine, must be taken into consideration when choosing a standard (Raudsepp, 1995). Figure 5.2 shows both the WDS-spectra of jarlite/jørgensenite and fluorite. Notice how the shapes show strong differences and that the jarlite/jørgensenite has a peak about 100 cps higher than that of fluorite.

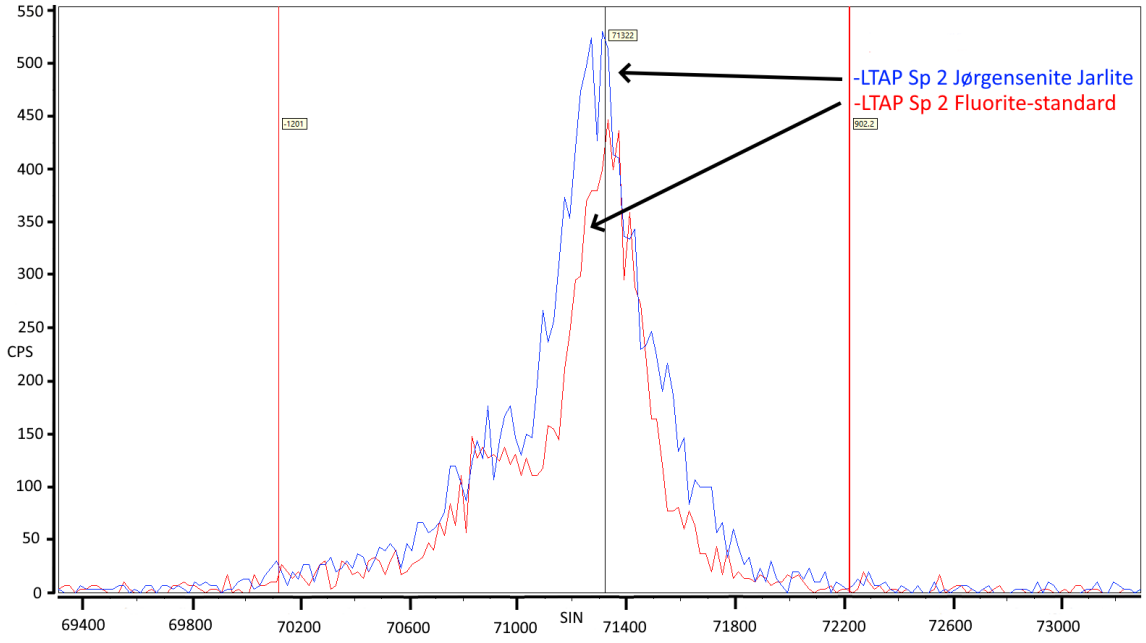

Figure 5.2. Shows the WDS-spectra of jarlite/jørgensenite (blue) compared with that of the fluorite standard (red) used in the analysis.

Fluorine in fluorite is 4-coordinated and each Ca-F bond have a strong ionic character due to the difference in electronegativity. Fluorine in jørgensenite/jarlite is either 2-coordinated, 3-coordinated or 4-coordinated and the bond type varies from strongly ionic, F-Sr and F-Na bonds, to partially covalent F-Al bonds. This means that fluorine in jarlite/jørgensenite has a

different bonding environment than that of fluorine in fluorite. Fluorite is therefore not a suitable mineral to use as a standard when analysing more complex fluorides. Unfortunately, no suitable mineral to use as a F-standard was available during the EPMA-analysis, and fluorite had to be used. The resulting consequence was that measured weight-percentage of fluorine in the analysed minerals, was lower than the theoretical amount reported in the literature. Furthermore, the erroneously low weight-percentage of fluorine effected the total recorded weight-percentage of each analysis. As a result of this, it became difficult to assess whether the minerals were analysed for their entire chemical diversity of minor elements.

5.5 Multi-Collector Inductively Coupled Plasma Mass Spectrometer

It was decided that some of the samples should be analysed by mass spectrometry, as to gain further insight into the $^{87}Sr/^{86}Sr$-signature of jørgensenite and stenonite. The motivation behind this was to see if such data could bring an additional insight into the crystallization environment of these minerals.

It was decided that the analysis should be of two different samples of stenonite and two different samples of jarlite/jørgensenite. Sample PAD-IG002 and PAD-IG019 were chosen as suitable representatives of jarlite/jørgensenite, based on the uncontaminated nature of the material. Crystals of jarlite/jørgensenite were extracted from sample PAD-IG019, while jarlite/jørgensenite of a more massive morphology was extracted from sample PAD-IG002. Great care was taken to not include other minerals than the ones in question. This applied specially to sample PAD-IG002, since the massive jarlite/jørgensenite is in close relation to cryptocrystalline aluminosilicates, topaz and an unidentified mica. The smallest traces of mica in the sample could compromise the results, since it would add a “foreign” source of radiogenic ^{87}Sr through its content of Rb. Because of the cryptocrystalline nature of the aluminosilicates, it was unproblematic to separate them from the jarlite/jørgensenite under the optical microscope, due to their difference in transparency. The aluminosilicates appeared opaque, in contrast to the completely transparent nature of the jarlite/jørgensenite fragments.

Suitable fragments of stenonite were taken from sample PAD-IG010 and PAD-IG022. These samples are representatives of a common stenonite paragenesis with weberite and pyrite. The

samples were chosen based on the purity of the stenonite. Regardless of the purity, the material was still crushed, and the fragments were sorted under a Leica MZ 16a stereomicroscope. Since weberite and stenonite share similar optical properties, only the fragments that showed the distinctive cleavage of stenonite were collected. It was unproblematic to separate the stenonite from the imbedded crystals of pyrite. Table 5.2 gives an overview of the samples with the collected weight and identity of the minerals. After collection, the fragments were grinded down to a fine powder with the use of an agate mortar and pestle.

Table 5.2: Overview of the collected material

Sample Number	Mineral	Weight before grinding	Weight after grinding
PAD-IG002	Jarlite/jørgensenite	0.0090 g	0.0075 g
PAD-IG010	Stenonite	0.0121 g	0.0067 g
PAD-IG019	Jarlite/jørgensenite	0.0085 g	0.0074 g
PAD-IG022	Stenonite	0.0156 g	0.0117 g

Because of restrictions regarding the timeframe of this research and the lack of a suitable mass spectrometers at UiO, it was only possible to have a small number of samples analysed at an external institute. The powders were therefore packed and sent to Cardiff University, Wales, for analysis at the Cardiff Earth Laboratory for Trace element and Isotope Chemistry (CELTIC). These powders were sent in the beginning of January 2023, but due to unforeseen events, they were not analysed until July 2023.

A Nu Plasma II multi-collector inductively coupled plasma mass spectrometer (MC-ICP-MS) was used to measure the $^{87}Sr/^{86}Sr$ ratios. A pristine fossil coral originating from Hendersson Island, South Pacific, was analysed as unknown for quality control (EC-5 internal coral standard). The long-term reproducibility of the standard was tested against 145 measurements, which yielded an $^{87}Sr/^{86}Sr$ ratio of 0.709162 ± 0.000006. The $^{87}Sr/^{86}Sr$ ratio was measured twice for each sample to give a minimum indication on the reproducibility of the measured ratios of each sample.

5.6 Single-Crystal X-Ray Diffractometer

Preliminary investigation of the samples was carried out with a Leica MZ 16a stereomicroscope at NHM, Økern. During this part of the research, the primary goal was to visually identify jarlite and jørgensenite crystals. Crystal aggregates of jarlite/jørgensenite were simultaneously collected, to be used in the collection of crystal-structure data from a Single Crystal X-ray Diffractometer (SXRD). For those reasons, only samples with notable cavities were studied. The samples studied were PAD-IG006, PAD-IG007, PAD-IG013 through PAD-IG026.

Suitable aggregates were collected from samples PAD-IG006, PAD-IG007 and PAD-IG013. Crystal aggregates of jarlite and jørgensenite were extracted by needle and scalpel. The aggregates were placed in small droplets of oil on a glass-slide and separated under a Streiss Stemi 508 stereomicroscope. Transmitted light was used to observe the different directions of extinction. This proved to be a useful tool to identify the different crystallographic domains within an aggregate of jarlite/jørgensenite crystals. The nature of these aggregates of fan-shaped crystals caused problems regarding the extraction of single individuals. The fan shaped aggregates have grown along [100], which is the tabular surface in jarlite/jørgensenite crystals. This means that in order to separate two individuals, the crystals must be placed on their narrowest surface and cut along the broadest. This proved to be problematic, but extraction of suitable single crystals was achieved.

Sample PAD-IG026 was included into this study in August 2023, and found by H. Friis during his summer travels to Ivittuut. This sample does not contain cavities and jørgensenite was inferred to occur as massive intergrowths of fan-shaped aggregates.

5.5.2 Analysis

The single-crystals were analysed by the use of a Rigaku Dual Beam Synenergy-S single-crystal X-ray diffractometer, equipped with a HyPix-6000 HE detector, at the Natural History Museum in Oslo. Molybdenum (Kα) was used as the X-ray source. An acceleration voltage of 50 kV with an electric current of 1 mA was used. The diffractometer is controlled through the Rigaku provided software CrysalisPro.

A pre-experiment was performed to test potentially suitable single crystals. This was done to make sure that the crystal did not contain more than one crystallographic domain, before the start of the analysis. The pre-experiments try to determine a unit cell, based on a short series of

collected reflections, and reports the percentage of reflections that correlated with the proposed cell. Because of the difficulties regarding the extraction of true single crystals, a correlation of approximately 95 % between measured reflections and the proposed unit cell, was deemed acceptable. This means that all of the analysed crystals, contain traces of different crystallographic domains, which will contribute to a slight increase in uncertainty in the results.

5.5.3 Data Integration

After analysis, it became necessary to process the raw data through peak integration and absorption correction. This was performed in the "red" version of CrysalisPro, as opposed to the online version used during the analysis. The SXRD analysis records transmitted reflections from the crystal structure as a series of frames containing points in reciprocal space. These points are inversely proportional correlated with the reflection planes of the crystal structure and acts as the basis of the orientation matrix. The orientation matrix is a 3x3 matrix and connects the reciprocal coordinate system with the orthonormal coordinate system of the diffractometer (real space) (Massa, 2000). It therefore acts as a basis when first determining the unit cell parameters, and the matrix is used to assign the reflections coordinates in the recorded reciprocal space (Blake, 2009a). With a correct orientation matrix and precise reciprocal coordinates, the intensities of the reflections can be found through integration. The orientation matrix is found automatically by the software, but it can be tweaked and redefined if one suspect that the crystal contains more than one crystallographic domain (for example due to twinning). This was not necessary, but the orientation matrix was recalculated based on the full set of frames of recorded reflections.

The integration of the reflections is based upon the numerical evaluation of the volume of each refraction peak as seen as points in the recorded reciprocal space. CrysalisPro integrates each peak by placing each identified signal within a box. The box is constructed based on a suitable background estimation, and the box will therefore confine an isolated signal (Blake, 2009b). Great care must be taken when assigning a suitable background, so that weaker signals is not lost. This is often corrected for through double integration. A standard integration procedure was conducted through the use of CrysalisPro "red".

After peak integration it becomes necessary to correct the collected data for X-ray absorption. This correction takes into account the chemical nature of the analysed crystal and its morphology. Heavier elements will typically absorb a greater amount of the incident x-rays

than the lighter elements. The morphology of the single crystal in use will also have to be taken into account, due to the absorption differences in anisotropic materials (Massa, 2000). Both aspects were corrected for during the data processing. Most of the procedure is done automatically by CrysalisPro, as long as a correct chemical formula is provided. The potential of anisotropic absorption must be corrected for through manual mapping of the surface of the single crystal.

5.5.4 Structure Refinement

The crystal structures were solved and refined using the WinGx software (Farrugia, 2012), with incorporated ShelX-programs (Sheldrick, 2008). These software-packages were chosen based on their demand of user interaction and script-manipulation.

Direct methods with ShelXS, were used for creating structure solutions, which in turn were refined with ShelXL (Sheldrick, 2015). The atoms in the structure were positioned manually by correlating the reported bond lengths to that of the literature and the initial refinement was conducted with isotropic displacement parameters. The numbering of the positions was correlated with the numbering of that of Hawthorne (1983, 1997), to make it easier to compare the results. After occupying each atomic site, the structures were refined with anisotropic displacement factors, which assigned an atomic displacement parameter (Ueq) to each atom. These atomic displacement parameters were used in combination with the chemical results from the SEM- and EPMA-analysis to test for partial- and dual-occupancy. The occupancy of the atomic positions of interest were opened by assigning each position a different free variable number (occupancy parameter). These free variable numbers react upon refinement according to the calculated relationship between the number of electrons recorded at a given atomic site, and the atom assigned to that position. A free variable number close to 1, suggest that the atomic site is fully occupied by the assigned atom, while a number significantly different from 1 suggests that the position is either partially occupied or contains mixed occupancy. A number less than 1 either suggests mixed occupancy with an atom lighter than the one assigned or a partial occupancy. A number higher than one suggests mixed occupancy with an atom heavier than the one assigned.

After partial- and dual-occupancy had been tested, the weighting scheme was refined until it converged with the suggested weighting scheme of the ShelXL-program, which completed the

refinement. Lastly the cif-files were opened in VESTA (Momma and Izumi, 2011), which was used to create the structural figures presented in this thesis.

6 Results

6.1 Petrography

6.1.1 Optical

Table 6.1 presents the chemical formula of the locality-specific minerals mentioned in the text. Since most of the minerals of interest shares similar optical properties, mineral identification with an optical microscope proved inconclusive. Most of the minerals in question share a low interreference colour of first order grey, they are white in transmitted light and have a somewhat similar relief. The exception is for fluorite, baryte and stenonite, which proved easier to identify based on the isotropic nature of fluorite, and the distinctive interference colour of baryte and stenonite. Because of this, the most accurate information which the optical analysis of the thin sections gave, was that of their texture. Textural analysis also provided means to identify jarlite/jørgensenite paragenesis based on the distinctive, fan-shaped crystal clusters, as is typical for these minerals (Pauly et al., 1997). The following section will give a description of the optical results.

Table 6.1: Chemical formulas of uncommon minerals mentioned in the text

Mineral	**Formula**
Bøgvadite	$Na_2SrBa_2Al_4F_{20}$
Jarlite	$Na_2(Sr, Na, \square)_{14}Al_{12}(Mg, \square)_2F_{64}(OH, H_2O)_4)$,
Jørgensenite	$Na_2(Sr, Ba)_{14}Na_2Al_{12}F_{64}(OH, F)_4$
Pachnolite/Thomsenolite*	$NaCaAlF_6 \cdot H_2O$
Stenonite	$Sr_2Al(CO_3)F_5$
Weberite	Na_2MgAlF_7

*Pachnolite and Thomsenolite are polymorphs (Hawthorne and Ferguson, 1983).

6.1.1.1 Jarlite and Jørgensenite

Jarlite and jørgensenite were found in all the samples, as presented in Appendix 9.1. Jarlite/jørgensenite are mainly found as fan-shaped crystal aggregates. The individual member of the fan-shaped aggregate are elongated prisms, wider near the termination than at the base of the crystal. The termination can be both bladed, but also capped. When removed from the aggregate, the single crystals are transparent, and turn into a white powder when crushed. The

aggregates in their entirety are whiter, and less translucent than the individual crystals. Free-standing jørgensenite crystals seem to be somewhat broader than jarlite crystals.

Free-standing crystal aggregates are only encountered in cavities, and in most of the material, individual aggregates have grown together to form a continuous matrix. The size of the crystal aggregates varies from 1,5-1,0 mm at the largest, to 0,05 mm and smaller. This is most noticeable under XPL, as can be seen in Fig. 6.1. The only mineral present in this figure is jørgensenite. Jørgensenite has a white to weak grey colour in PPL and it commonly has an interference colour of first order grey in XPL, but first order orange has also been observed. This can be seen in Fig. 6.1, where the termination of the crystals of the fan-shaped aggregates has an interference colour of first-order orange, while the stem of the crystals has an interference colour of first-order grey. It has a moderate to high relief, which is easier to observe in figure 6.2, and it show no signs of pleochroism.

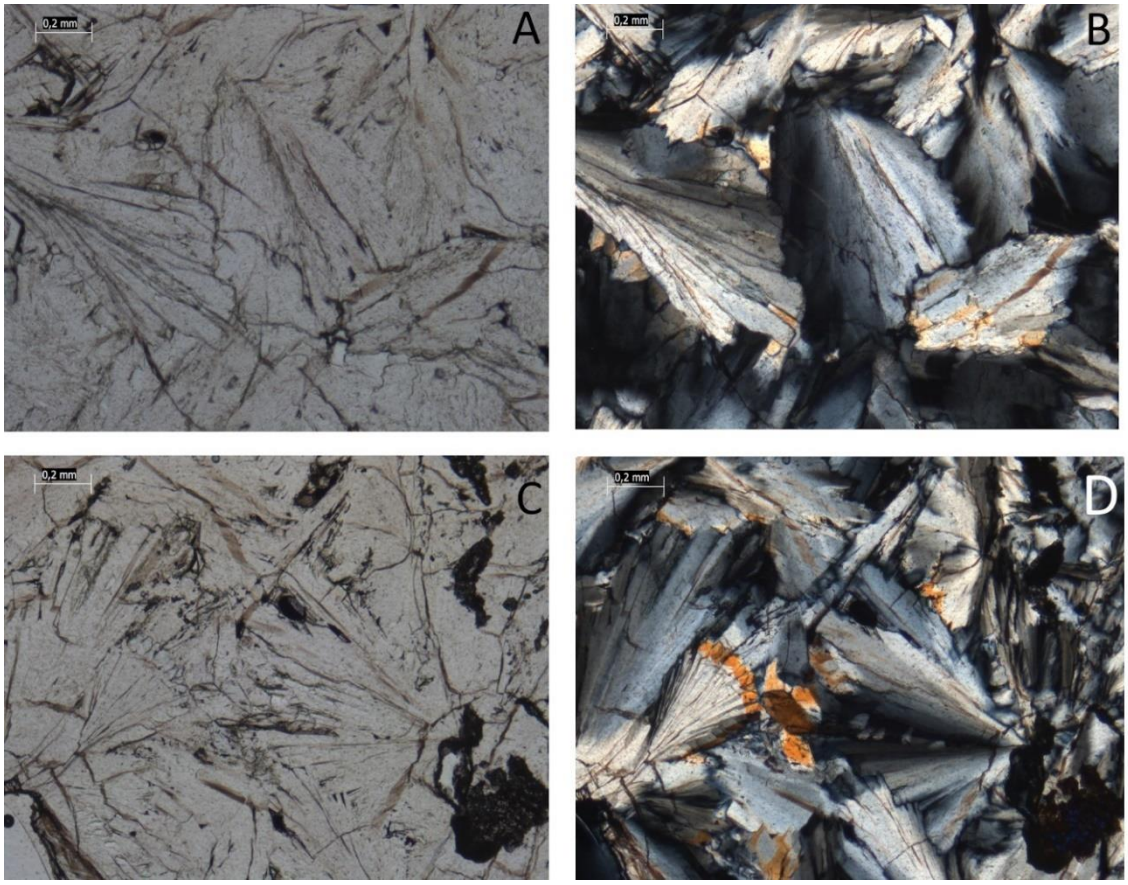

Figure 6.1: Representative fan-shaped crystal aggregates of jørgensenite. Figure A and C are captured under PPL, while B and C under XPL. The individual crystals are elongated and, in this case, have a capped termination. Notice the optical difference between the stem of the crystal and the termination, especially evident in figure D.

Even though jørgensenite and jarlite share optical similarities, a distinction between them can be made with the use of XPL, as is presented in Fig. 6.2, from sample PAD-IG002a. In this sample, jarlite occur as a mantle surrounding a jørgensenite core and a weak difference in interference colour can be observed. Jarlite has a low first-order grey, almost white interference colour, and possible a lower relief than jørgensenite. Both the core and the mantle seem to be optical homogenous. Baryte is found as small grains with an orange interference colour and a high relief, dispersed within a matrix of bøgvadite. The bøgvadite is quite difficult to distinguish from jørgensenite, but its interference colour has a somewhat lighter shade of grey. The difference in relief between bøgvadite and jarlite and jørgensenite is not apparent, but it seems to be somewhat higher. A euhedral crystal of pyrite can also be seen in the figures lower side.

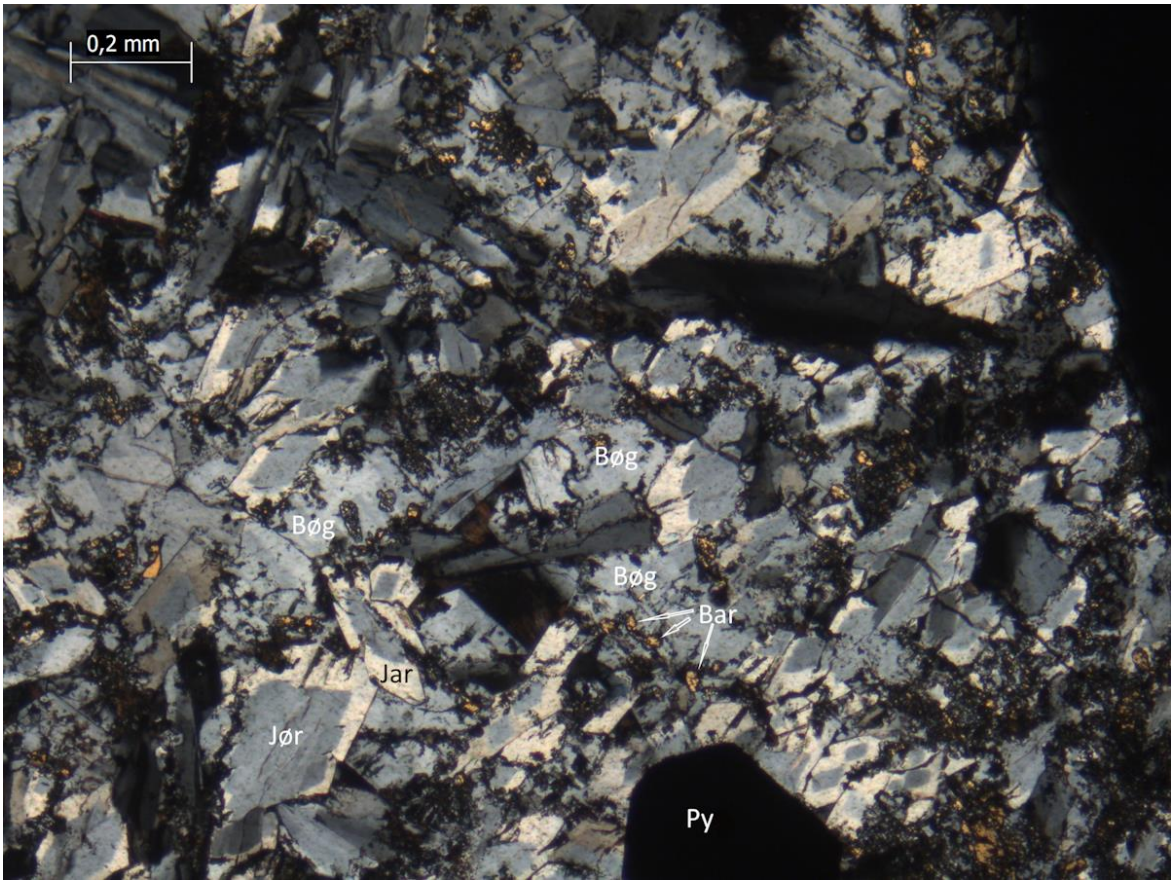

Figure 6.2: An XPL-image from sample PAD-IG002a, which represent a Sr-Ba- rich paragenesis, containing baryte (Bar), bøgvadite (Bøg), jørgensenite (Jør) and jarlite (Jar). An optical difference between jarlite and jørgensenite can be identified, based on a small difference in interference colour. Bøgvadite is more difficult to identify based on its similar interference colour to jørgensenite, but it seems to have a lower relief and is only found as anhedral areas between the jørgensenite/jarlites crystals. Baryte is found as small grains with an orange interference colour.

This relationship is also found in Fig. 6.3, in which also bøgvadite and baryte are present. Their presence is however more difficult to view than in Fig. 6.2. However, a clear optical difference is seen between jarlite and jørgensenite. Jarlite is found as a mantle with an interference colour higher than the jørgensenite core (figure 6.3A). A dark band of an unknown Al-silicates is also present, and it incapsulates the area containing baryte and bøgvadite from the mostly jørgensenite-bearing matrix. These types of silicate-bands were found throughout the sample. In this sample, baryte is not identifiable with the optical microscope but the backscatter image (Fig. 6.7) shows the complete paragenesis.

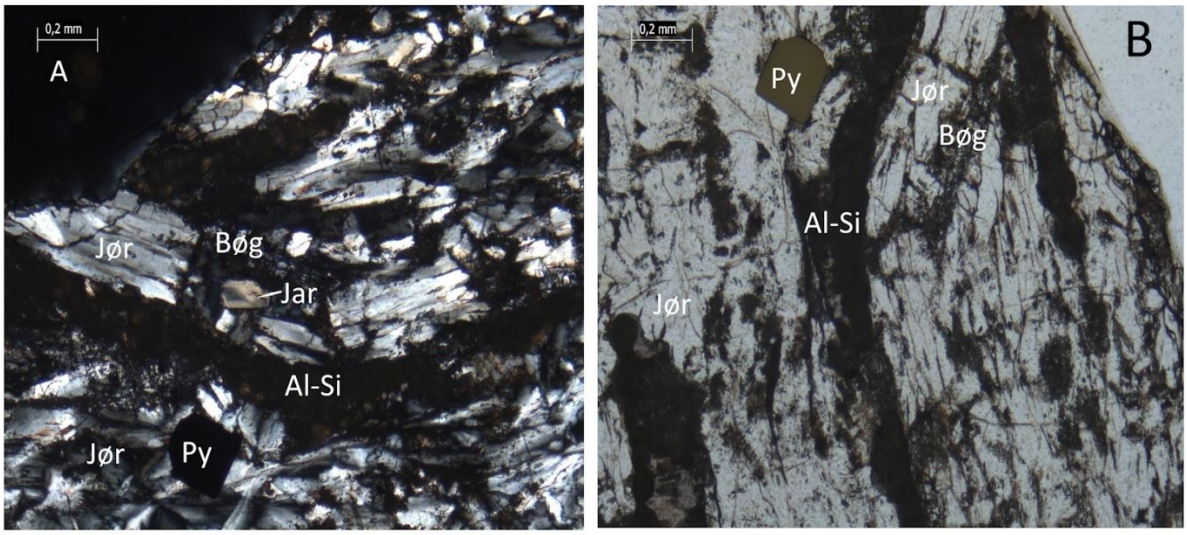

Figure 6.3: The same paragenesis as presented in Fig. 6.2. Bøgvadite (Bøg) and baryte is however less apparent, and their presence is not evident without the use of a SEM. The same optical difference between jørgensenite (Jør) and jarlite (Jar) can be viewed in figure A, under XPL. The dark band which goes across the field of view is an unidentified Al-silicates, most likely a phyllosilicate. Pyrite (Py) is found as a 0.2mm wide, euhedral crystal.

In sample PAD-IG006, jørgensenite was found as fan-shaped aggregates within the outline of a crystal, marked by a rim of fluorite and topaz (Fig 6.4A and B). Bøgvadite and baryte were found together with jørgensenite within the fluorite- and topaz-rim. The bøgvadite/baryte grains show an optical continuity and they show simultaneous extinction during rotation with XPL. The baryte grains are too small to be properly observed with an optical microscope (see Fig. 6.7 and 6.9). This textural feature was also observed in PAD-IG005 and PAD-IG011, and an image from the former sample can be found presented as Fig. 6.4. In this figure, jørgensenite is found within the outline of several crystals, which show an elongated, double-terminated bladed or pyramidal habitus. This suggests a pseudomorphic replacement by jørgensenite, since the crystal morphology does not match one expected from jørgensenite. The outlines of these

crystals are preserved by rims of cryptocrystalline topaz (beige) which evolve into thin, acicular crystals (black). Jørgensenite is also found outside of the of the topaz rims, acting as the major matrix-mineral of the sample. Some fluorite-crystals can be found confined within both the topaz and the jørgensenite.

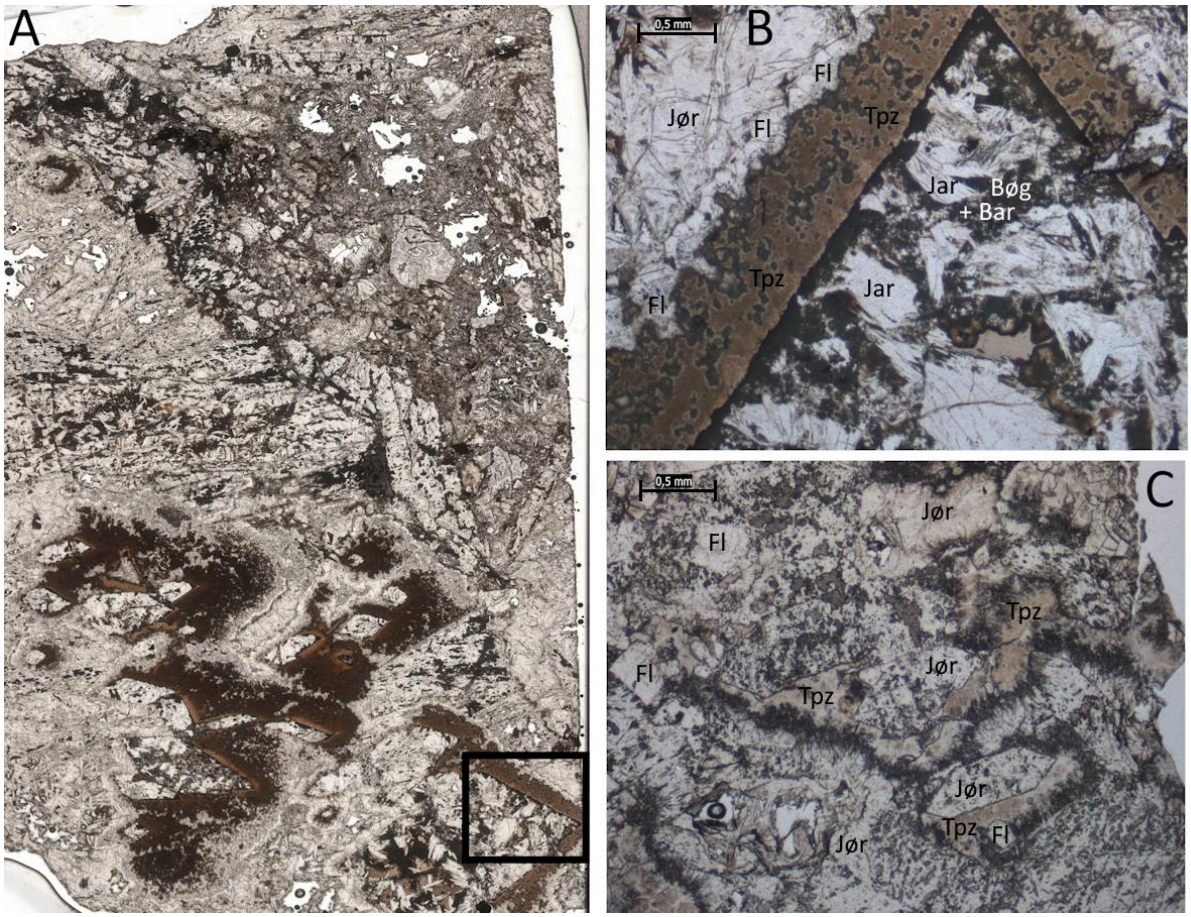

Figure 6.4: Two of the samples in which jørgensenite (Jør) and jarlite (Jar) were found as pseudomorphs after an unknown mineral. Figure A shows a scan of the thin-section PAD-IG006a in which the black square marks the area shown in figure B. Figure C presents a similar paragenesis found in sample PAD-IG005. Fluorite (Fl), topaz (Tpz), baryte (Bar) and bøgvadite (Bøg) are also a part of this paragenesis.

6.1.1.2 Stenonite

The habitus of all the stenonite found, was anhedral and no euhedral crystals occurred in the samples. Stenonite occurs together with jarlite/jørgensenite, pyrite, weberite, fluorite and quartz.

The presence of stenonite was hard to establish with a petrographic microscope, but the identification was made easier by using cross-polarized light. In thin-sections, stenonite has a clear, white colour, quite distinguishable from the greyness of jørgensenite, as shown in Fig. 6.5. The greyness of the jørgensenite is most likely caused by inclusions of jarlite, which is more clearly seen in figure 6.5B, where the grains of jørgensenite show optical heterogeneity. Compared to jørgensenite, stenonite has a low relief, which can be witnessed in the same figure, along with its higher order interference colour. Stenonite is quite homogenous and the irregular and anhedral grains seem to display an optical continuity throughout the field-of-view of Fig. 6.5B.

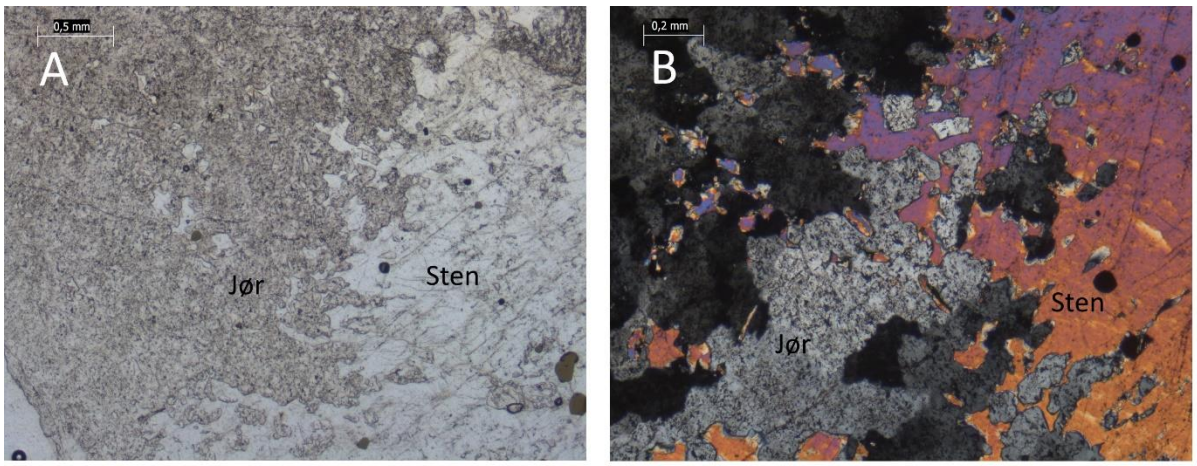

Figure 6.5: An PPL (A) and XPL (B) of a contact between stenonite (Sten) and jørgensenite (Jør), from sample PAD-IG007. The stenonite have a distinctive interference colour of a higher order than jørgensenite, and a lower relief.

The maximum birefringence of stenonite is however higher than what is shown in Fig. 6.5B and Fig. 6.6B gives a more representative level of it. In this image, stenonite can be seen to occur as a rim around a euhedral crystal of pyrite. The rim is quite homogenous, but it contains several unfilled cracks. The grey mineral is jørgensenite, while the second white mineral is fluorite.

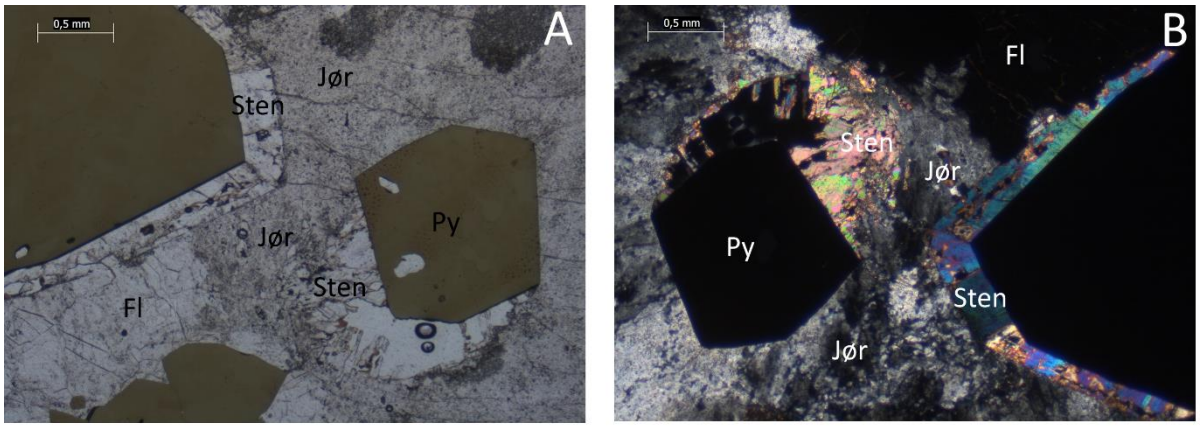

Figure 6.6: An PPL- and XPL-image from sample PAD-IG007, showing a more complete paragenesis. Stenonite (Sten) is found as a rim surrounding a euhedral crystal of pyrite (Py), while jørgensenite (Jør) acts as the matrix-mineral together with fluorite (Fl). From figure B, it is evident that the jørgensenite matrix is not optical homogenous, and it contains several intergrown crystal-aggregates. The stenonite show its highest interference colour, in contrast to the stenonite presented in Fig. 6.5.

6.1.2 SEM-EDS

6.1.2.1 Jørgensenite, Jarlite and Bøgvadite

Figure 6.7, shows an electron backscatter image (BSE-image) of the jarlite-jørgensenite-bøgvadite-baryte paragenesis, found in sample PAD-IG002. Jørgensenite is found as a core overgrown by jarlite, residing in what seems to be a matrix of bøgvadite and baryte. The bøgvadite matrix seems to be continuous, while the baryte grains are anhedral and slightly rounded. The overall appearance of baryte, is one of corrosion. The jarlite/jørgensenite crystals are elongated prismatic, with bladed termination with some of the crystal being double terminated. Others seem to have grown from a continuous matrix of jørgensenite. The jarlite overgrowth seem to be somewhat less euhedral than the jørgensenite core. The contrast difference of the minerals in this image is quite apparent, with an increasing BSE-brightness from jarlite to jørgensenite to bøgvadite to baryte, representing an increase in electron density. This makes it less challenging to differentiate between these minerals than with the optical microscope. The less electron dense, BSE-dark mineral is an unidentified, cryptocrystalline Al-silicate, most likely topaz.

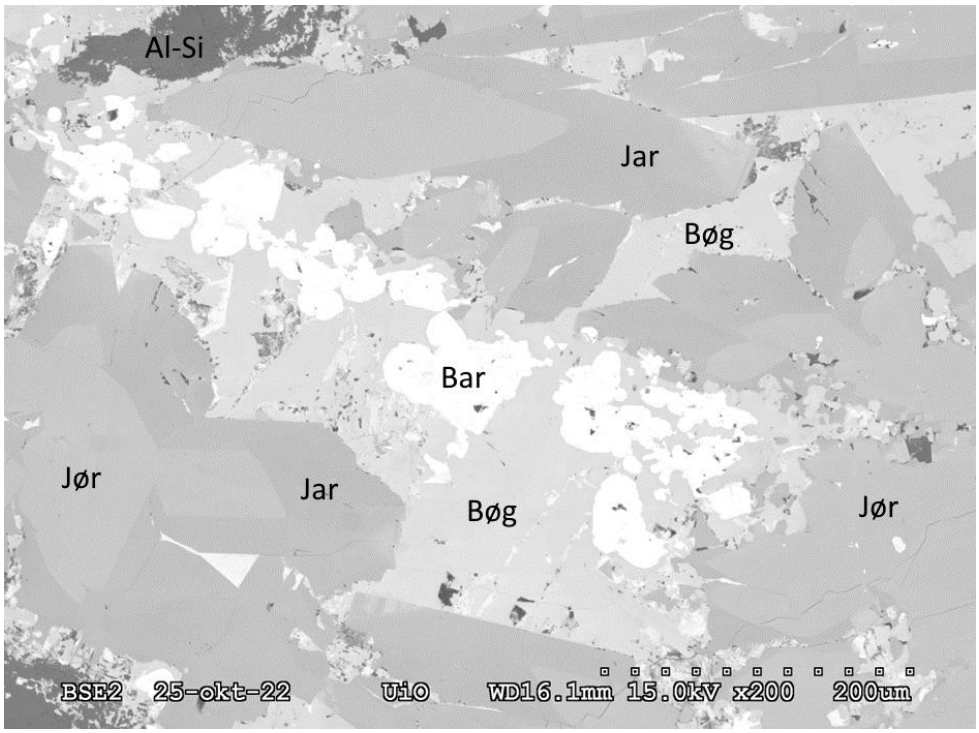

Figure 6.7: An electron backscatter image presenting the same area as presented in Fig. 6.3. The presence of baryte (Bar) and bøgvadite (Bøg) is, contrary to the PPL- and XPL-image, apparent. The density difference between jørgensenite (Jør) and jarlite (Jar), make the core- and mantle-feature readily observable.

Figure 6.8A and B, shows the EDS- spectra of jørgensenite and jarlite. As can be seen from the two figures, there is quite a noticeable difference between these two minerals in terms of their respective EDS-spectra following their difference in chemistry. Both minerals show strong peaks for Na, Sr, Al and F. The Sr-peak seem to be somewhat weaker in jarlite than it is in jørgensenite. Jarlite has additional peaks for Mg, K and Ca, which are absent in jørgensenite. However, jørgensenite has small, but noticeable peak identified as Ba due to the characteristic appearance of the Lα-peak closely followed by Lβ-peaks. The Ba peak is quite weak in jarlite, but present. The presence or absence of Mg has therefore been used as the most viable indicator as to identify and distinguish between jarlite and jørgensenite when working on these samples. This method is supported by the chemical data presented in the literature (Hawthorne, 1983; Pauly and Nielsen, 1992; Hawthorne, 1997; Pauly et al., 1997).

There are no significant elemental overlaps within the spectra, which means that quantification of the EDS-spectra yields trustworthy values in agreement with the element ratio of the theoretical formulas. There is however a small overlap between the F Kα-peak and the Ba Kα-peak.

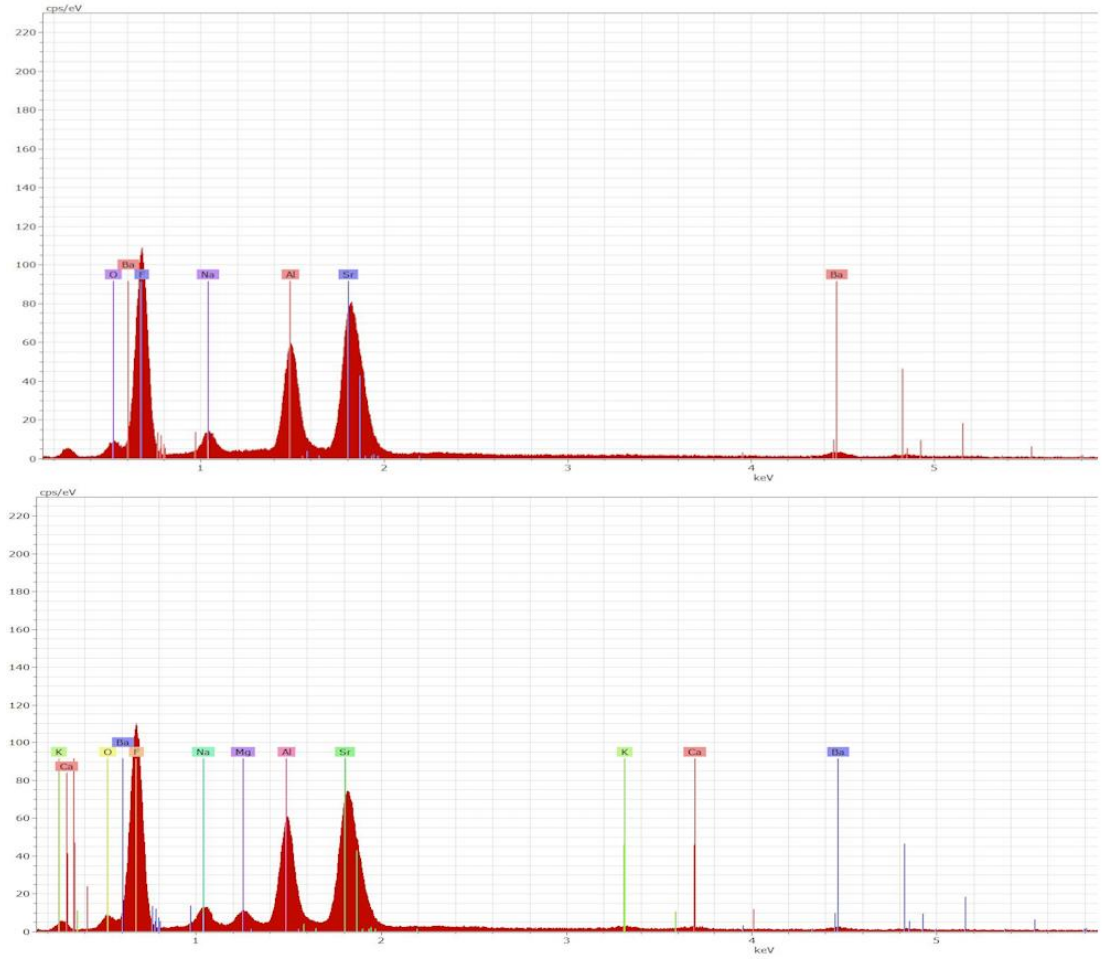

Figure 6.8: The EDS-spectra of jørgensenite (A) and jarlite (B). The EDS-spectra indicate the presence of F, O, Na, Al, Sr and Ba, with an additional presence of Ca, K and Mg in jarlite (B). The Ba-peak is stronger in jørgensenite than in jarlite, while the opposite is true for Sr.

Figure 6.9 presents a BSE-image of the same area on sample PAD-IG006a as shown in Fig. 6.4B. With the SEM, it is easier to distinguish between bøgvadite and baryte within the matrix confined by the cryptocrystalline topaz and fluorite. Baryte is found as the mostly miniscule grains of the BSE-brightest colour intermixed with bøgvadite, which is slightly less BSE-bright. However, a larger grain of baryte is found at the topside middle of the figure. Jarlite is present as fan-shaped aggregates, with euhedral termination. This is somewhat difficult to observe due to how intergrown the individual jarlite crystal are, but it can be readily observed within the baryte of the topmost side. Outside of the topaz-fluorite rim, jørgensenite is found as euhedral fan-shaped crystal aggregates, together with pachnolite/thomsenolite.

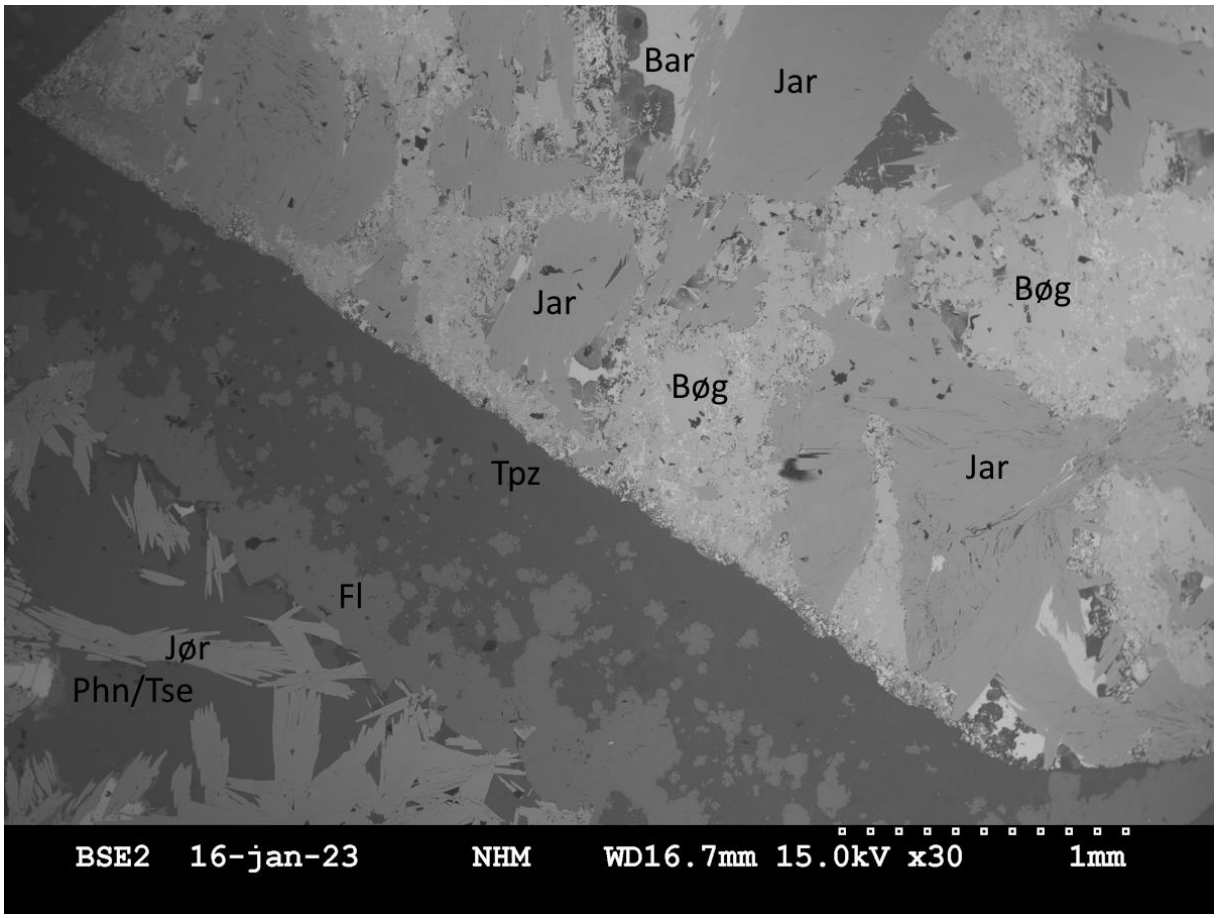

Figure 6.9: An electron backscatter image of the area shown in Fig. 6.4B. A mixture of fluorite (Fl) and topaz (Tpz) can be found marking the outline of the crystal shape, in which jarlite (Jar), bøgvadite (Bøg) and baryte (Bar) were found. The bottom left corner show fan-shaped aggregates of jørgensenite (Jør) together with pachnolite/thomsenolite (Phn/Tse).

6.1.2.2 Stenonite

Figure 6.10 presents a BSE-image of the same area of sample PAD-IG007 as presented in Fig. 6.6. The contrast has been increased in order to enhance the visibility of the density contrast between jarlite and jørgensenite. Jarlite can be found as the less BSE-bright grains within the jørgensenite matrix together with galena. The stenonite has a more homogenous appearance and show no sign of any major chemical variations or inclusions. Additionally, the stenonite is quite fractured and the distinctive cleavage pattern of stenonite is especially apparent in the fractured area at the topside, right corner of the figure. As was seen in Fig. 6.6, stenonite occur as a rim surrounding a euhedral pyrite-crystal, and the boundary between the stenonite and the jørgensenite matrix is distinctively sharp. The boundary between the topside stenonite and the

jørgensenite matrix is less distinctive and more irregular, and some stenonite grains are found completely embedded within the jørgensenite matrix.

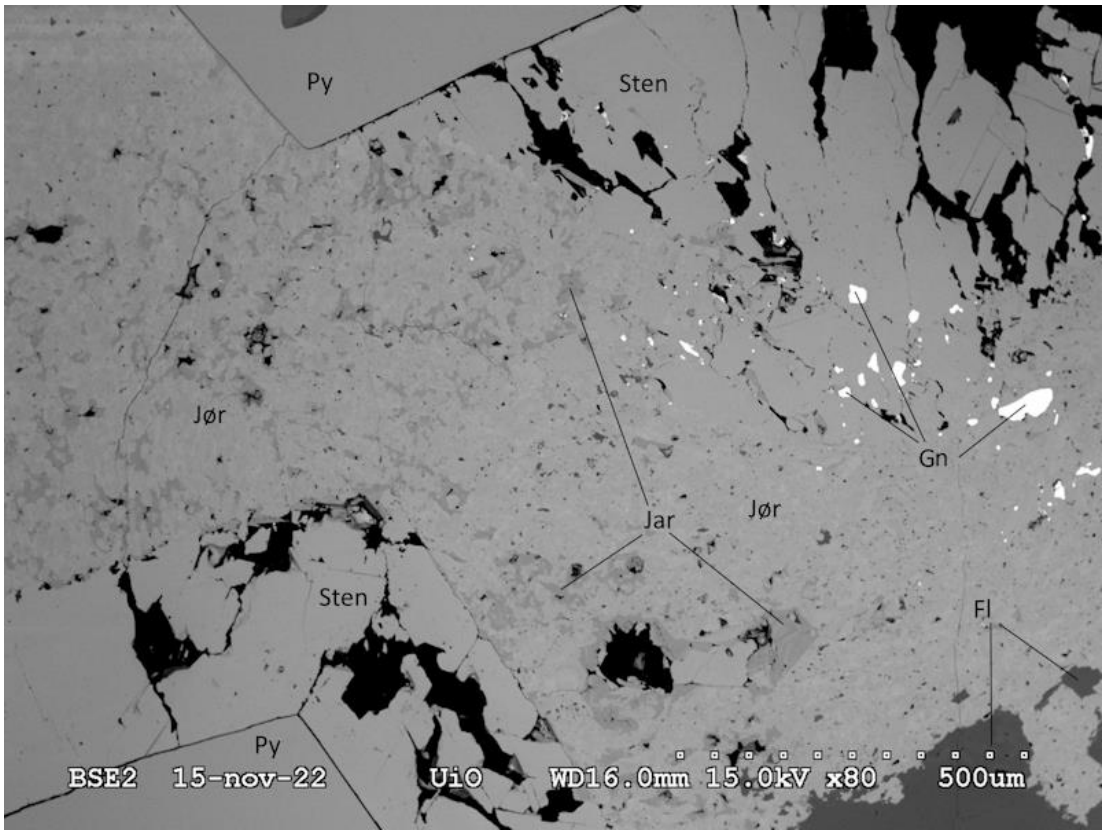

Figure 6.10: An electron backscatter image of the same area as presented in Fig. 6.6. The contrast has been increased in order to present the chemical heterogeneity of the jørgensenite (Jør) matrix. The heterogeneity is mainly caused by small zones of jarlite (Jar). The figure also shows the presence of galena (Gn), which can be seen as the grains of the brightest colour.

6.1.3 Accessory Minerals

The following section will give a brief description of the accessory minerals found throughout the samples, with special focus on the ones which have already (in this section) been encountered.

6.1.3.1 Pyrite

Pyrite has been found throughout the samples, and they are especially common to find together with stenonite. Pyrite is found as euhedral crystals, either as pentagon dodecahedrons, cubes or with an intermediate habitus.

6.1.3.2 Flourite

Fluorite has been common throughout the samples, and it has been found both as euhedral crystals, massive and as smaller inclusions within jørgensenite. Most of the fluorite appear colourless, but a weak tint of purple has been observed. Fluorite found as inclusions within jørgensenite have been anhedral and irregular in shape. They are often miniscule and in the size range of a few μm. In sample PAD-IG012, these types of fluorites are found to give the jørgensenite an appearance of a pale-green colour. The euhedral crystals along with cleavage fragments of fluorite can often be found as larger individuals up to a 1 mm in size. These can be found dispersed in a groundmass of jørgensenite. The massive and more anhedral zones of fluorite are often intermixed with topaz but have also been found dispersed in jørgensenite and in weberite.

6.1.3.3 Baryte/ Celestine

Baryte and /or celestine were found throughout the samples and were found to occur in three distinctive ways. In sample PAD-IG001, Sr-rich baryte or Ba-rich celestine were found as euhedral crystals measuring up to several mm in length (Fig.6.11). The crystals are broad but elongated and have a bladed termination.

The second type of occurrence is the one described previously in this section, in which they form a paragenesis with bøgvadite, jørgensenite and jarlite.

The third type of occurrence is one were baryte is found to have grown as tiny, elongated crystals (1μm in width) grown both in a radiating manner and a mesh-like manner. They have usually been found in a matrix of pachnolite/thomsenolite, but this has not been completely validated.

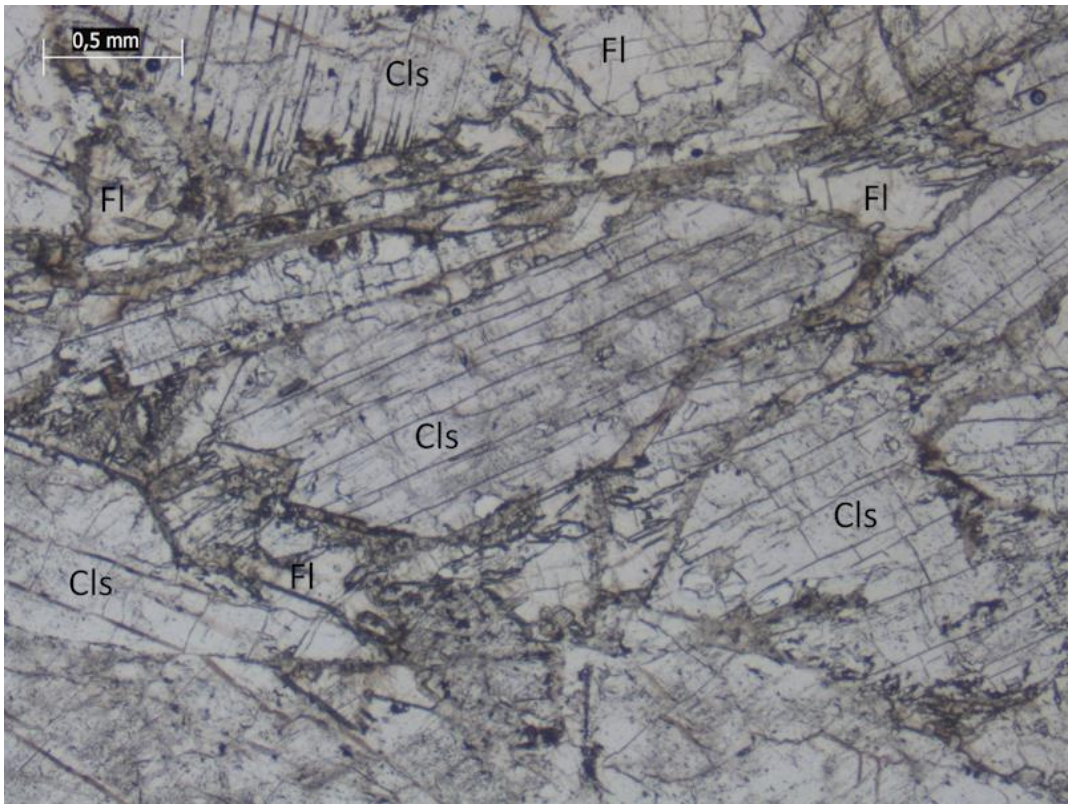

Figure 6.11: A PPL-image of euhedral celestine crystals from sample PAD-IG001. The celestine (Cls) grains are separated by fluorite (Fl).

6.1.3.4 Topaz

Topaz has mainly been found as anhedral, cryptocrystalline masses. The cryptocrystalline topaz occurs either as elongated bands or rims marking the pseudomorphs of jørgensenite after an unknown mineral. Topaz is also found as miniscule, euhedral crystals with a width below 0.1µm (presented in Fig. 7.11). These crystals seem to have grown from the cryptocrystalline masses and are often found to be intruding from such a cryptocrystalline mass, into the jørgensenite matrix.

6.1.3.5 Pachnolite/Thomsenolite

Pachnolite and Thomsenolite are to polymorphs with the chemical formula $NaCaAlF_6 \cdot H_2O$ (Hawthorne and Ferguson, 1983). It is possible to distinguish between them if they are found as euhedral crystals, but in the case where they occur as anhedral fillings, XRD must be used. Throughout the samples, pachnolite/thomsenolite were found as anhedral cavity-and vein-fillings, and they were often present in cavities lined by jarlite and/or jørgensenite crystals.

They are white and translucent, and they have a low an interference colour of first-order grey, which makes it hard to distinguish them from the other aluminofluorides.

6.1.3.6 Weberite

Weberite have mostly been found as anhedral masses, in paragenesis with stenonite, pyrite and jørgensenite.

6.2 EPMA-results

Tables 6.2, 6.4, 6.6 and 6.8 present the electron microprobe data collected from six thin sections, based on a total of 220 analysed points. The presented data is the mean weight percentage (wt%) of each analysed element over a given number of points (*n*), for each sample. The corresponding uncertainties are the combined uncertainties, calculated from the reproducibility of each set of related points at 1SE. The tables alco include the calculated formula in *apfu*, based on 12, 12, 4 and 1 Al-atoms for jarlite, jørgensenite, bøgvadite and stenonite respectively.

High vacuum was used when performing the EPMA-analysis. As a consequence, the resolution of the backscatter images was significantly higher than for the SEM-imaging. As a result, a widespread, but weak chemical variation within the jørgensenites and jarlites was observed for the first time, as shown in Fig. 6.13. The figure shows an aggregate of jarlite crystals which has grown into a cavity later filled by pachnolite/thomsenolite. Jørgensenite is also present on the right side and in the left upper corner. To image the difference between jarlite and jørgensenite the contrast had to be increased. Consequently, pachnolite/thomsenolite appears almost black.

The analysis of these minerals required a beam size of 20 μm in order to avoid burning of the material. This made it difficult to find suitable, chemical homogenous areas to analyse. Several of the points collected during the analysis therefore suffer from minor chemical heterogeneity related to the recording of different chemical domains within the jarlites and jørgensenites. This will be noticeable in Tables 6.2 and 6.6, as elevated uncertainties caused by the lower reproducibility of the analysis, especially related to the minor elements.

The main difference between jørgensenite and jarlite, is their concentration of Ba, Na and Mg. Jørgensenite should contain Ba, but be free of Mg, while jarlite should have a Mg-concentration greater than the Na-concentration found at the *Mg*-site (Pauly and Nielsen, 1992; Pauly et al. 1997; Hawthorne and Burns, 1997). As was presented in the petrography-section of the results (Section 6.1), this seems to be correct based on the quantification of the measured EDS-points of jørgensenite and jarlite. This difference was also used in order to separate the data measured with the EPMA, into jarlites and jørgensenites. The difference in the Ba- and Mg-concentration can be seen in Fig. 6.12, where jørgensenite is presented as the blue triangles and jarlite as the orange dots.

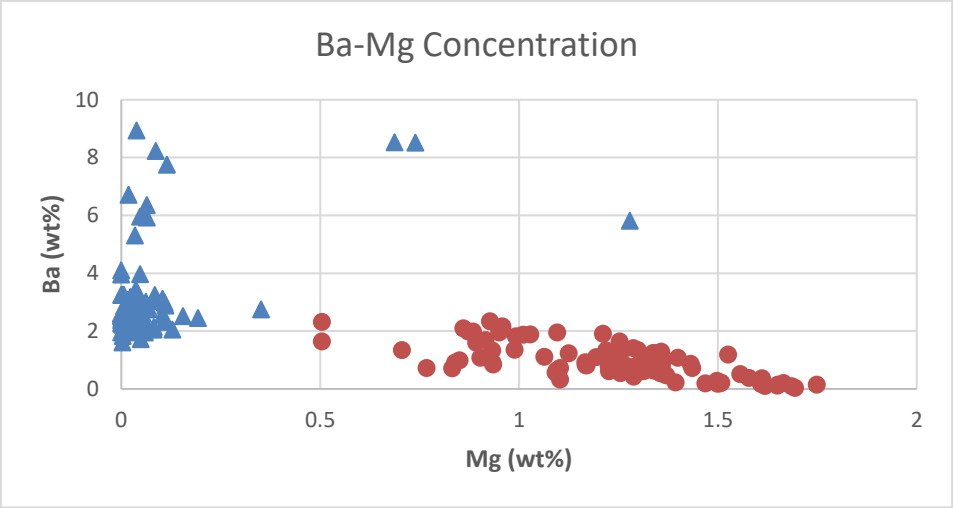

Figure 6.12: Ba-concentration (in wt%) plotted against the Mg-concentration (wt%), in order to show the difference between jarlite (red dots) and jørgensenite (blue triangles), and to present in which way the chemical data was used to distinguish between the two minerals.

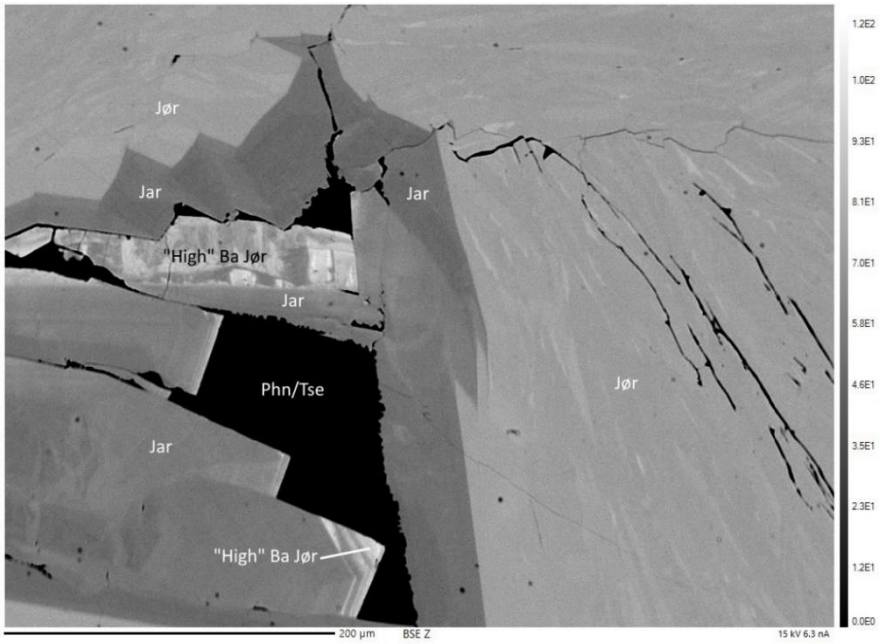

Figure 6.13: A backscatter image from the EPMA showing parts of an aggregate of jarlite (Jar) crystals located within a cavity filled by pachnolite/thomsenolite (Phn/Tse). Jørgensenite (Jør) is found as the brighter shades of grey. Notice the weak chemical difference within both the jarlite crystals and within the zone of jørgensenite.

6.2.1 Jørgensenite

Table 6.2 presents the chemical data recorded from jørgensenites in five different thin-sections. The data collected from sample PAD-IG002a, -IG002b, -IG005 and -IG006a, show similarities for all the elements, except for a variation in Ba. However, there seems to be a high uncertainty in the Ba-concentration for these four samples, and the uncertainty increases with an increasing content. PAD-IG002b has the lowest recorded wt% of Ba, with a concentration of 2.1(4) wt% (0.513 *apfu*). PAD-IG005 has the highest of the four, with a Ba content of 4(2) wt% (0.832 *apfu*), but it also has the highest uncertainty.

The concentration of Mg, K and Ca in samples PAD-IG002a, -IG002b, -IG005 and -IG006a, are overall quite low. Potassium and Ca are present in minor amounts, with the content of K being around 0.1 *apfu* and the content of Ca being around 0.05 *apfu*. Magnesium was not detected (< 0.001 wt%). The uncertainties should be noted, and both the recorded content of K and Ca have high uncertainties, caused by the chemical heterogeneity of jørgensenite. The K content of sample PAD-IG006a is especially suspect, with an uncertainty matching the recorded concentration (0.1(1) wt%), which leaves the value meaningless.

The chemical data recorded from sample PAD-IG007 show noticeable differences from the other four, with elevated Ba concentration (8(1) wt%). The content of K and Ca is also higher in this sample. However, the most noticeable difference is the content of Mg, which is 0.9(3) wt% (1.16 *apfu*) and in stark contrast with the Mg concentration of the four other samples (< 0.001 wt%).

Of the five samples, PAD-IG007 is the one that most closely resemble the chemical composition of jørgensenite, as presented by Pauly et al (1997), Table 7.7, Section 7.5.1.

All of the samples show a deficiency in F, which was to be expected (see section 5.4.2). This have as a consequence, that the total wt% of the samples are too low. However, the deficiency in the measured wt% of F seems to be systematic, with a deficiency of 10% when compared to the literature (Pauly and Nielsen, 1992). Additional F has therefore been included in Table 6.2, together with the literature value of H_2O, in separate rows from the measured data. These additions were used to calculate a new total wt% for jørgensenite.

Table 6.2: Chemical data (EPMA) and calculated formula of jørgensenite

	PAD-IG002a	PAD-IG002b	PAD-IG005	PAD-IG006a	PAD-IG007
n	22	18	26	22	3
Weight percent (wt%)					
F	39 (1)	39.1(5)	39(1)	39(1)	38.6(4)
Na	2.7(2)	2.7(2)	2.7(2)	2.6(3)	2.34(9)
Mg	0	0	0	0	0.9(3)
Sr	40 (1)	39.9(8)	38(2)	40(2)	34.1(9)
Al	10.7(3)	10.7(3)	10.6(3)	10.7(4)	10.4(1)
K	0.11(8)	0.11(8)	0.19(8)	0.1(1)	0.54(3)
Ca	0.06(4)	0.05(3)	0	0.08(7)	0.22(4)
Ba	3(1)	2.3(4)	4(2)	3(1)	8(1)
Total	95(2)	95(1)	93(2)	95(2)	94.8(2)
H_2O[1]	1.22	1.22	1.22	1.22	1.22
F[2]	3.9	3.91	3.9	3.9	3.8
Total[3]	100.12	100.13	98.12	100.12	99.82
Atoms per formula unit (*apfu*)					
F	61.796	62.372	61.836	61.817	63.641
Na	3.51	3.58	3.59	3.39	3.18
Mg	0	0	0	0	1.160
Sr	13.72	13.78	13.07	13.62	12.18
Al	12.00	12.00	12.00	12.00	12.00
K	0.086	0.082	0.145	0.110	0.435
Ca	0.048	0.040	0.057	0.058	0.169
Ba	0.569	0.513	0.832	0.598	1.735

1: The value of H_2O is taken from Pauly et al. (1997)
2: Additional F calculated from the measured F-concentration, based on a 10% deficiency
3: A new total based on the additional wt% from H_2O and F

Table 6.3 presents the empirical formula of jørgensenite as calculated from the *apfu*-values presented in Table 6.2. The site-assignment follow that of Pauly et al. (1997). The five empirical formulas seem to overall follow the same pattern. The three *Sr*-sites have an abundance of element ranging from 14.11 *apfu* in sample PAD-IG005 to the highest of 14.53 *apfu* in sample PAD-IG007. The *Na*2-position have a deficiency of atoms, ranging from 0.41 *apfu* in sample PAD-IG005 to the highest of 0.61 *apfu* in sample PAD-IG007. It may be possible that this is due to analytical errors regarding the measurement of Na. The *F*-site have a deficiency of atoms, ranging from 0.36 *apfu* at the smallest to 3.20 *apfu* at the greatest. The content of H_2O/

OH^- have not been included, due to uncertainty in relatability between the samples from Pauly et al. (1997) and this study. However, it seems unlikely that the absent content of H_2O/OH^- would explain the deficiency of atoms at the *F*-site.

Table 6.3: Empirical formula of jørgensenite

Samples	Empirical Formula
PAD-IG002a	$Na_{2.0}(Sr_{13.72}Ba_{0.57}K_{0.09}Ca_{0.05})_{\Sigma\ 14.43}Na_{1.51}Al_{12.00}F_{61.80}$
PAD-IG002b	$Na_{2.0}(Sr_{13.78}Ba_{0.51}K_{0.08}Ca_{0.04})_{\Sigma\ 14.41}Na_{1.58}Al_{12.00}F_{62.37}$
PAD-IG005	$Na_{2.0}(Sr_{13.071}Ba_{0.83}K_{0.15}Ca_{0.06})_{\Sigma\ 14.11}Na_{1.59}Al_{12.00}F_{61.84}$
PAD-IG006a	$Na_{2.0}(Sr_{13.62}Ba_{0.60}K_{0.11}Ca_{0.06})_{\Sigma\ 14.39}Na_{1.39}Al_{12.00}F_{61.81}$
PAD-IG007	$Na_{2.0}(Sr_{12.18}Ba_{1.74}K_{0.44}\ Na_{0.34}Ca_{0.17})_{\Sigma\ 14.87}\ (Mg_{1.16}\ Na_{0.84})_{\Sigma 2.0}\ Al_{12.00}F_{63.64}$

6.2.2 "High-Ba" Jørgensenite

The microprobe data recorded from the analysis of "High"-Ba jørgensenite is presented in Table 6.4, together with the calculated atoms per formula unit. This chemical composition was only measured from small zones located near the termination of certain jørgensenite crystals. Due to the small size of these zones, it was not possible to analyse the required number of points (>3) in order to calculate the reproducibility. As a consequence of this, no uncertainties are reported for chemistry of the three points presented in Table 6.4.

The most prominent difference between these analyses and those of the more common jørgensenite presented earlier, is the amount of Ba measured. The most Ba-rich of the jørgensenite presented in Table 6.2, are the ones from sample PAD-IG007, which have an average Ba-content of 1.7 *apfu*. The lowest Ba-content of the Ba-rich jørgensenite, contain almost twice that amount (3.2 *apfu*). Another difference is the amount of recorded Mg. Most of the jørgensenite presented earlier contained a Mg-concentration below the detection limit (<0.001), while the Mg-content of these jørgensenite is between 0.56 and 0.58 *apfu*. Additionally, the content of Ca and K are also higher for these Ba-rich jørgensenites, ranging from 0.41 to 0.49 *apfu* for K and 0.60 to 0.77 *apfu* for Ca.

Table 6.4: Chemical data (EPMA) and calculated formula of Ba-rich jørgensenite

	PAD-IG002b	PAD-IG002b	PAD-IG011
Weight percent (wt%)			
F	37.13	37.72	36.99
Na	2.28	2.29	2.34
Mg	0.56	0.57	0.58
Sr	26.84	26.46	27.91
Al	10.19	10.36	10.34
K	0.50	0.54	0.61
Ca	0.60	0.62	0.77
Ba	15.46	16.31	14.02
Total	93.59	94.89	93.55
Additional F	3.71	3.77	3.70
OH	1.22	1.22	1.22
New Total	98.52	99.88	98.47
Atoms per formula unit (*apfu*)			
F	62.10	63.04	60.98
Na	3.15	3.11	3.19
Mg	0.74	0.74	0.75
Sr	9.73	9.44	9.98
Al	12.00	12.00	12.00
K	0.41	0.44	0.49
Ca	0.48	0.49	0.60
Ba	3.58	3.71	3.20

The empirical formulas of these Ba-rich jørgensenite are presented in Table 6.5. The *Sr*-site are closer to their ideal value of 14 atoms, than they are in the ordinary jørgensenites (Table 6.3), but a small abundance of atoms is present. The amount of Na and Mg are slightly too low to fill both the *Na1*- and *Na2*-site. The *F*-sites show a deficiency of F-atoms, similar to that of jørgensenite and jarlite.

Table 6.5: Empirical formula of Ba-rich jørgensenite

Samples	Empirical Formula
PAD-IG002b	$Na_2(Sr_{9.73}Ba_{3.58}Ca_{0.48}K_{0.41})_{\Sigma 14.2}(Na_{1.15}Mg_{0.74})_{\Sigma 1.89}Al_{12}F_{60.98}$
PAD-IG002b	$Na_2(Sr_{9.44}Ba_{3.71}Ca_{0.49}K_{0.44})_{\Sigma 14.08}(Na_{1.11}Mg_{0.74})_{\Sigma 1.85}Al_{12}F_{63.04}$
PAD-IG011	$Na_2(Sr_{9.98}Ba_{3.20}Ca_{0.60}K_{0.49})_{\Sigma 14.27}(Na_{1.19}Mg_{0.75})_{\Sigma 1.94}Al_{12}F_{60.98}$

6.2.3 Jarlite

The microprobe data recorded from the analysis of jarlite is presented in Table 6.6, together with the calculated atoms per formula unit.

The Mg-content varies from the lowest of 0.8(3) wt% (1.10 *apfu*) to the highest of 1.5 wt% (1.78 *apfu*). The content of K varies from 0.7 to 1.1 wt% (0.55 to 0.8 *apfu*), which is consistently higher than what was found in jørgensenite. The same pattern is seen for the content of Ca, varying from 0.2 to 0.8 wt% (0.11 to 0.6 *apfu*), which is significantly higher than what was found in jørgensenite.

Of the samples presented in Table 6.6, the data from PAD-IG006a show a somewhat different chemical nature than the other four. Especially evident is the increased Ba content of 1.7(4) wt% (0.38 *apfu*), which is 1.2 wt% higher than the lowest value recorded in sample PAD-IG002b. Similar to the Ba, K and Ca data from jørgensenite in Table 6.2, the Ba measurements in the jarlites have a high relative uncertainty, which especially evident in sample PAD-IG006a. A mean Ba-content of 1 wt% with an uncertainty of 1 wt%, presents a measurement from which the heterogeneity of jarlite is evident.

The Sr content in the jarlites is systematically lower than that of the jørgensenites and varies between 36.5 wt% and 38.1 wt%, as opposed to the variation between 38 and 40 wt% found in the jørgensenites.

Table 6.6: Chemical data (EPMA) and calculated formula of jarlite

	PAD-IG002a	PAD-IG002b	PAD-IG005	PAD-IG006a	PAD-IG011
n	16	15	11	26	22
Weight percent (wt%)					
F	40.1(8)	40.3(7)	39.0(6)	39(1)	40(1)
Na	2.3(3)	2.3(3)	2.45(9)	2.4(4)	2.2(1)
Mg	1.4(3)	1.5(2)	0.8(3)	1.1(6)	1.3(2)
Sr	36.5(9)	36.5(8)	38(1)	38.1(9)	38(1)
Al	11.1(3)	11.2(2)	10.9(1)	11.0(3)	11.0(4)
K	1.1(5)	1.0(5)	0.7(1)	0.7(6)	1.2(2)
Ca	0.8(4)	0.8(2)	0.08(3)	0.2(2)	0.5(1)
Ba	0.8(7)	0.5(4)	1.7(4)	1(1)	0.9(6)
Total	94(2)	94(1)	94(1)	94(2)	94(3)
H_2O[1]	2.9	2.9	2.9	2.9	2.9
F[2]	4.01	4.03	3.9	3.9	4.0
Total[3]	100.92	100.93	100.8	100.8	100.9
Atoms per formula unit (*apfu*)					
F	61.56	61.54	61.200	61.36	61.45
Na	2.97	2.95	3.18	3.11	2.79
Mg	1.69	1.78	1.10	1.34	1.53
Sr	12.17	12.08	12.91	12.79	12.64
Al	12.00	12.00	12.00	12.00	12.00
K	0.80	0.76	0.55	0.55	0.91
Ca	0.60	0.60	0.06	0.11	0.34
Ba	0.17	0.11	0.38	0.20	0.20

1: The value of H_2O is taken from Hawthorne (1983)
2: Additional F calculated from the measured F-concentration, based on a 10% deficiency
3: A new total based on the additional wt% from H_2O and F

Table 6.7 presents the empirical formula of jarlite for each of the five samples. The formula is calculated based on the *apfu*-values presented in Table 6.6. The elements have been assigned their respective positions based on the study of Hawthorne (1983) and Pauly and Nielsen (1992).

The *Na*-, the *Na*/*Mg*- and the *Al*-sites sum up to the ideal values, while the *Sr*-sites show a consistent abundance of the assigned elements (Sr, Na, K, Ca and Ba). Due to the high uncertainties related to K, Ca and Ba, it is difficult to assess whether the abundance of 0.4 *apfu* at the *Sr*-site for sample PAD-IG011 and PAD-IG002b is due to an issue regarding the site-

assignment, or just a consequence of the unprecise measurement of the concentration of these elements.

Table 6.7: Empirical formula of jarlite

Samples	Empirical Formula
PAD-IG002a	$Na_{2.0}(Sr_{12.17}Na_{0.66}K_{0.80}Ca_{0.6}Ba_{0.17})_{\Sigma\ 14.4}(Mg_{1.69}Na_{0.31})_{\Sigma 2.0}Al_{12.00}\ F_{61.56}$
PAD-IG002b	$Na_{2.0}(Sr_{12.08}Na_{0.73}K_{0.76}Ca_{0.60}Ba_{0.11})_{\Sigma\ 14.28}(Mg_{1.78}Na_{0.22})_{\Sigma\ 2.0}Al_{12.00}\ F_{61.54}$
PAD-IG005	$Na_{2.0}(Sr_{12.91}Na_{0.28}K_{0.55}Ca_{0.06}Ba_{0.38})_{\Sigma\ 14.18}(Mg_{1.10}Na_{0.90})_{\Sigma\ 2.0}Al_{12.00}\ F_{61.20}$
PAD-IG006a	$Na_{2.0}(Sr_{12.79}Na_{0.45}K_{0.55}Ca_{0.11}Ba_{0.20})_{\Sigma\ 14.1}(Mg_{1.34}Na_{0.66})_{\Sigma\ 2.0}Al_{12.00}\ F_{61.36}$
PAD-IG011	$Na_{2.0}(Sr_{12.64}Na_{0.32}K_{0.91}Ca_{0.34}Ba_{0.20})_{\Sigma\ 14.41}(Mg_{1.53}Na_{0.47})_{\Sigma\ 2.0}Al_{12.00}\ F_{61.45}$

6.2.4 Bøgvadite and Stenonite

Table 6.8 presents the chemical composition of bøgvadite from two samples and stenonite from one. Due to the relative rareness and size of these minerals, the number of points that was possible to analyse is far less than with the jarlite and the jørgensenite presented in the preceding section, with the exception of sample PAD-IG006a, in which it was possible to analyse 17 points on bøgvadite.

6.2.4.1 Bøgvadite

The concentration of the major elements Na, Al, F, Sr and Ba in the two bøgvadite samples are similar, with the only difference being a small variation in the Sr-content of 0.07 *apfu*. As with the jarlites and the jørgensenites, the bøgvadite analysis suffer from a systematic deficiency in the measured F-content. However, the deficiency of F in bøgvadite is greater than the one affecting jarlite and jørgensenite, and the measured F-concentration in bøgvadite is 20% less than the literature value (Pauly and Pettersen, 1988). As with Tables 6.2 and 6.6, additional F has been calculated and provided for the two samples of bøgvadite.

As can be seen from the raw data provided in Appendix III-1, K, Ca and Mg were measured, but they were removed due to their high uncertainties up to six times as high as the actual value

of the mean content, leaving the value below the detection limit. In addition, the values of Mg and K were in the second decimal (wt%), meaning that the potential contribution would have been minimal.

Table 6.8: Chemical data (EPMA) and calculated formula of bøgvadite and stenonite

Mineral	Bøgvadite	Bøgvadite	Stenonite
Sample Number	PAD-IG002a	PAD-IG006a	PAD-IG007
n	6	17	7
Weight percent (wt%)			
F	32.8(4)	33(1)	22.8(3)
Na	4.4(1)	4.4(2)	0.01(1)
Mg	0	0	0
Sr	4.1(6)	3(1)	48.4(9)
Al	11.3(2)	11.3(3)	7.1(1)
K	0	0	0.008(8)
Ca	0	0	0.6(1)
Ba	38(1)	38(2)	0
Total	91.0(8)	90(2)	79(1)
F[1]	6.56	6.6	2.28
CO_3 [2]	-	-	16.0
Total[3]	97.56	96.6	97.28
Atoms per formula unit (*apfu*)			
F	16.46	16.46	4.56
Na	1.83	1.84	0.002
Mg	-	-	-
Sr	0.44	0.37	2.099
Al	4.00	4.00	1.0
K	-	-	0.001
Ca	-	-	0.057
Ba	2.66	2.68	-
CO_3	-	-	1.013

1: Additional F, calculated based on a 20% deficiency in bøgvadite and 10% deficiency in stenonite
2: Concentration of CO_3 in stenonite as published in Pauly (1962)
3: The new total, based on additional F for bøgvadite and F and CO_3 in stenonite

6.2.4.2 Stenonite

The stenonite sample show a high content of Sr with a concentration of 48.4(9) wt%. Na, K and Ca are present in minor amounts, with the Ca-concentration being the highest of the three (0.6 wt%). As with jørgensenite and jarlite, the measured F-content of stenonite (22.8 (3) wt%) show a systematic deficiency of around 10 %, which have been added in a sperate row of Table 6.8.

The CO_3-group was not measured during the EPMA-analysis and the concentration of CO_3 in stenonite is based on the concentration of Pauly (1962).

Table 6.9 presents the empirical formula of bøgvadite and stenonite. The *Na*-site in bøgvadite show for both samples a deficiency of around 0.16 *apfu* from the ideal number of 2. A deficiency of elements is also found at the *Sr*-site, but with an *apfu* of respectively 0.44 and 0.37 for the two samples, meaning that the value is quite far from the ideal *apfu* of 1. In contrast, the *Ba*-site show an abundance of 0.66 and 0.68 *apfu* for the respective samples. The *F*-site in the formula show a deficiency for both samples, which was to be expected, given the EPMA-data.

The empirical formula of stenonite show an abundance of elements in the *Sr*-site of 0.159 *apfu*, but the Sr content in itself is quite close to the ideal value of 2. The CO_3-group is close to its ideal of 1.0, while the *F*-site has the same deficiency of elements as jarlite, jørgensenite and bøgvadite.

Table 6.9: Empirical formula of bøgvadite and stenonite

Mineral	Sample Number	Empirical Formula
Bøgvadite	PAD-IG002a	$Na_{1.83}Sr_{0.44}Ba_{2.66}Al_{4.00}F_{16.46}$
Bøgvadite	PAD-IG006a	$Na_{1.84}Sr_{0.37}Ba_{2.68}Al_{4.00}F_{16.46}$
Stenonite	PAD-IG007	$(Sr_{2.099}Na_{0.002}K_{0.001}Ca_{0.057})_{\Sigma 2.159}Al(CO_3)_{1.013}F_{4.56}$

6.2.5 Chemistry of Accessory Minerals

In connection with the investigation of the Sr-minerals contained within the samples, several observations were made of accessory minerals and their related textures. Since jørgensenite, jarlite, bøgvadite and stenonite were of main interest during this study, none of these accessory minerals were thoroughly analysed with the EPMA. Some EPMA-tests were performed on pachnolite/thomsenolite, hydrokenoralstonite and weberite during the preliminary analyses with the EPMA. This analysis showed that these minerals reacted similar to jørgensenite, jarlite and bøgvadite when analysed, with a systematic deficiency in F. Therefore, these data are not presented here.

6.3 MS-ICP-MS results

Table 6.10 presents the $^{87}Sr/^{86}Sr$-ratios measured from MC-ICP-MS, at the University of Cardiff. The presented values are the mean value of two measurements and the uncertainties are the reproducibility calculated from the 2σ-values of each independent measurement. Both stenonite and jørgensenite have been analysed and these are abbreviated sten and jør, respectively. The measured $^{87}Sr/^{86}Sr$-ratios are consistent for both jørgensenite and stenonite but display a small variation between the two mineral species. Jørgensenite have a somewhat lower $^{87}Sr/^{86}Sr$- signature of 0.78933 and 0.708918, when compared to the signature of stenonite, 0.709738 and 0.709698.

Table 6.10 also presents selected $^{87}Sr/^{86}Sr$-measurements from the literature. The initial $^{87}Sr/^{86}Sr$-ratios for these measurements have been recalculated based on an approximate age of 1270 Ma for the Ivigtut intrusion (Köhler et al. 2007) and a decay constant of $1.3972*10^{-11}$ (Faure and Mensing, 2005). The $^{87}Sr/^{86}Sr$-signature of stenonite and jørgensenite are similar to those measured for cryolite and fluorite (Blaxland, 1974), but generally dissimilar to the measurements from whole rock analysis.

Table 6.10: $^{87}Sr/^{86}Sr$-isotopes measurements for jørgensenite, stenonite, and from literature

Sample	**Mineral**	**$^{87}Sr/^{86}Sr$**	**2se**
PAD-IG002	Jør.	0.708933	0.000015
PAD-IG010	Sten.	0.709738	0.000016
PAD-IG019	Jør.	0.708918	0.000014
PAD-IG022	Sten	0.709698	0.000013
$^{87}Sr/^{86}Sr$-ratios from the literature			
Sample	**$^{87}Sr/^{86}Sr$**	**$^{87}Rb/^{86}Sr$**	**$^{87}Sr/^{86}Sr$ (initial)**
Cryolite A[1]	0.71062	0.0472	0.70977
Cryolite B[1]	0.70894	0.0095	0.70877
Fluorite[1]	0.71611	0.3740	0.70941
Granite[1]	0.86343	8.656	0.70846
Granite[1]	1.06727	20.603	0.69842
Dark Granite[2]	0.98408	17.021	0.67936
Dark Granite[2]	1.00062	16.905	0.69797
Granophyre[2]	1.22608	31.59	0.66053
Granophyre[2]	0.96883	15.381	0.69347
Granophyre[2]	1.13567	27.398	0.64517

1: Blaxland (1974)
2: Goodenough (1997)

6.4 SXRD-results

The following pages will present the results from the structural analysis of jørgensenite, jarlite and stenonite. As mentioned in the introduction to the method section of this thesis, some of the datasets were inherited from H. Friis. These datasets were treated as raw-data and all of the processing and refinement were conducted by the author of this thesis. The main problem of gathering good single-crystals from jørgensenite and jarlite was caused by their morphological occurrence as stacked, fan-shaped aggregates (see Fig. 6.1). Nevertheless, the work resulted in the analysis of nine jørgensenite and one jarlite. Two of the jørgensenite were discarded during the refinement, due to the low quality of the collected data. During this section jørgensenite will be abbreviated jør and jarlite will be abbreviated jar.

Table 6.11: Structural parameters and refinement data of jørgensenite and jarlite

Mineral	Jør[1]	Jør[1]	Jør[1]	Jør[1]	Jør[1]	Jør[1]	Jør [1]	Jar[2]	Jør[3]	Jar[4]
Sample Number	PAD-IG014	PAD-IG015	PAD-IG023	PAD-IG023	PAD-IG006	PAD-IG006	PAD-IG026	PAD-IG025		
Exp. Number	557	711	729	730	686	702	804	699		
Crystal System	Monoclinic	Monoclinic	Monoclinic	Monoclinic	Monoclinic	Monoclinic	Monoclinic	Monoclinic	Monoclinic	Monoclinic
Space Group	*C2/m*	*C2/m*	*C2/m*	*C2/m*	*C2/m*	*C2/m*	*C2/m*	*C2/m*	*C2/m*	*C2/m*
a (Å)	16.0734(2)	16.0625(3)	16.0262(4)	16.0341(3)	16.0497(4)	16.0630(4)	16.1034(2)	15.9859(5)	16.059(7)	15.942(4)
b (Å)	10.9580(1)	10.9528(2)	10.9314(2)	10.9253(2)	10.9252(2)	10.9555(2)	11.0392(1)	10.8406(4)	10.974(4)	10.821(5)
c (Å)	7.2805(1)	7.2776(1)	7.2857(2)	7.2769(1)	7.2730(2)	7.2751(2)	7.3093(1)	7.2780(2)	7.277(3)	7.241(2)
B(°)	101.656(2)	101.678(2)	101.742(2)	101.676(2)	101.686(3)	101.659(2)	101.682(1)	101.884(3)	101.70(3)	101.86(2)
V (Å^3)	1255.89(4)	1253.85	1249.67	1248.43	1248.86(7)	1253.84(6)	1272.44	1234.21(8)	1256.0(9)	1222.5(?)
Z	1	1	1	1	1	1	1	1	1	1
F(000)	1374	1374	1400	1400	1348	1374	1436	1346		
ρ (g/cm^3)	3.97	3.94	4.07	4.07	3.9	3.97	4.14	3.94		
No. of collected reflections	29836	22585	28404	31145	17169	36864	32655	6414	4001	1495
No. of unique reflections	3478	2860	3463	3489	2847	3497	3554	2146	1940	
No. of parameters refined	130	130	129	130	130	128	130	129		
R (int)	0.0279	0.0311	0.0309	0.0494	0.0461	0.0678	0.0224	0.0197		
Final R1	0.0252	0.0269	0.0255	0.0275	0.0363	0.0351	0.0202	0.0262	0.074	0.053
wR2	0.044	0.0390	0.0627	0.0560	0.0591	0.065	0.0357	0.042	0.092	0.066
GooF	1.340	1.215	1.090	1.178	1.085	1.080	1.094	1.107		

1: $Na_2Sr_{14}Na_2Al_{12}F_{64}OH_4$
2: $Na_2Sr_{14}Mg_2Al_{12}F_{64}OH_4$
3: Hawthorne and Burns (1997)
4: Hawthorne (1997)

6.4.1 Structural Parameters of Jørgensenite and Jarlite

6.4.1.1 Jørgensenite

Included in Table 6.11 are unit cell parameters, collection data and refinement data. Of the seven experiments performed on jørgensenite, two originate from the same sample (exp. 729 and 730). A high number of reflections were collected for each sample, with 17,169 reflections yielding 2847 unique reflections at the lowest (exp. 686) and 36,864 reflections yielding 3497 unique reflections at the highest (exp. 702).

The refinement data presented are used to estimate the quality of the initial structure data and the proceeding refinement. These parameters and their meaning will be discussed more thoroughly in the discussion-section of this thesis. However, it is worth pointing out that the Goodness-of-fit parameter, varies quite considerably between the jørgensenites, from what is deemed an acceptable value of around 1.1, to an unsatisfactory value of 1.340 at the highest. All seven experiments were refined to a Final R1 between 2- and 4% with a wR2 between 4- and 6%.

From the unit cell parameters, it can be seen that the unit cell volume of the seven analysed jørgensenites have a difference of 24.01 $Å^3$ from the smallest of 1248.43 $Å^3$ (exp. 730) to the largest of 1272.44 $Å^3$ (exp. 804). The increase in unit cell volume seems to be primarily correlated with an increase in the length of the *a*-axis, with a smaller contribution of an increased length in both the *b*- and the *c*-axis. The *a*-axis varies from 16.0262 Å at the shortest to 16.1034 Å at the longest. The β-angle is quite consistent between the six experiments, but with a noticeable difference in exp. 729, in which the angle is 101.742°, as opposed to around 101.67° for the five others.

When comparing the presented unit cell parameters of jørgensenite with those already published by Hawthorne and Burns (1997) (Table 6.11), a small difference is noticeable. The *b*-axis of the jørgensenites presented in Table 6.11, seem to be consistently shorter than that of Hawthorne and Burns. Similarly, the *c*-axis seems to be consistently longer, while the *a*-axis show a variety of lengths. The average unit cell volume of the six experiments is smaller than the one presented by Hawthorne and Burns, with the most similar being experiment 557.

6.4.1.2 Jarlite

Table 6.11 also presents the structural parameters and refinement data for one experiment performed on a jarlite crystal as well as the literature data. It became evident during the sample collection and the SXRD pre-experiments, that jarlite was somewhat rarer to find than jørgensenite.

6414 reflections were collected, and 2146 unique reflections were found. The jarlite structure was refined to a final R1 of 2.62% with a GooF of 1.097. The *a*-, *b*- and *c*-axis of the unit cell were found to be 15.9859 Å, 10.8406 Å and 7.2780 Å respectively, with a β-angle of 101.686°. As with the jørgensenites, the unit cell parameters of the jarlite experiment are also slightly different from that of the already published data (Table 6.11). All three axis are slightly longer than in the published data and consequently, the unit cell volume is 11.71 $Å^3$ larger than that published by Hawthorne (1983).

When comparing the structural parameters of the jørgensenites and jarlite, the most noticeable difference is between the respective unit cell volumes. The average unit cell volume of jørgensenite is 1251.29 $Å^3$, which is an increase of 1.31% (16.44$Å^3$) from that of the analysed jarlite. Similar to that of jørgensenite, this difference in unit cell volume seems to be primarily caused by an increase in the length of the *a*-axis, from a jarlite length of 15.9885 Å to an average jørgensenite length of 16.049 Å.

6.4.2 Bond distances and polyhedron volume

Table 6.12 presents the bond distances of the *Sr*- and *Na*-sites for jørgensenite and jarlite. Additional bonds to the *Sr2*-site have been included in order to see how the bond length between the *Sr2*-site and *F8-site* varies throughout the samples. This distance is not recognized as a true bond in the literature (Hawthorne, 1983; Hawthorne and Burns, 1997). Two different coordinations for the *Sr2*-site have therefore been provided, both in Table 6.12 and in Table 6.13. These additional bonds will be further discussed in Section 8.3.

Table 6.12: Bond distances for the *Sr*- and *Na*-sites

Mineral	Jør	Jør	Jør	Jør	Jør	Jør	Jør	Jar
Exp. Number	557	711	729	730	686	702	804	699
Bond Distance								
Sr1-F3 (x2)	2.490(2)	2.487(2)	2.478(2)	2.477(2)	2.482(3)	2.494(3)	2.496(1)	2.473(2)
Sr1-F7 (x4)	2.929(2)	2.930(2)	2.921(2)	2.913(2)	2.918(2)	2.930(2)	2.974(1)	2.885(1)
Sr1-F10 (x4)	2.535(1)	2.535(1)	2.523(1)	2.532(1)	2.533(2)	2.539(2)	2.516(1)	2.526(1)
Average	2.684	2.684	2.673	2.674	2.677	2.654	2.662	2.659
Sr2-F2	2.668(2)	2.665(2)	2.673(2)	2.649(2)	2.649(2)	2.663(3)	2.726(1)	2.628(2)
Sr2-F4 (x2)	2.645(1)	2.640(1)	2.656(1)	2.628(1)	2.627(2)	2.647(2)	2.703(1)	2.634(1)
Sr2-F5 (x2)	2.834(1)	2.833(1)	2.839(2)	2.839(2)	2.838(2)	2.834(2)	2.836(1)	2.856(1)
Sr2-F6 (x2)	2.739(1)	2.735(1)	2.721(2)	2.720(2)	2.723(2)	2.737(2)	2.787(1)	2.664(1)
Sr2-F10 (x2)	2.635(1)	2.634(1)	2.631(1)	2.612(1)	2.615(2)	2.629(2)	2.695(1)	2.582(1)
Sr2-F8 (x2)*	3.096(2)	3.095(2)	3.112(2)	3.102(2)	3.100(2)	3.099(2)	3.094(1)	3.135(2)
Average (CN 9)	2.708	2.706	2.708	2.694	2.695	2.702	2.749	2.678
Average (CN 11)	2.770	2.767	2.772	2.759	2.759	2.768	2.807	2.750
Sr3-F1	2.416(1)	2.416(1)	2.449(1)	2.414(1)	2.416(1)	2.416(1)	2.422(1)	2.476(1)
Sr3-F2	2.852(1)	2.852(1)	2.830(1)	2.845(1)	2.849(2)	2.852(2)	2.842(1)	2.822(1)
Sr3-F4	2.508(1)	2.508(1)	2.498(1)	2.502(1)	2.507(2)	2.507(2)	2.514(1)	2.491(1)
Sr3-F5a	2.544(1)	2.542(1)	2.530(1)	2.537(2)	2.540(2)	2.538(2)	2.549(1)	2.510(1)
Sr3-F5b	2.552(1)	2.551(1)	2.537(2)	2.543(2)	2.544(2)	2.551(2)	2.564(1)	2.517(1)
Sr3-F6	2.505(1)	2.502(1)	2.503(1)	2.502(1)	2.501(2)	2.502(2)	2.513(1)	2.501(1)
Sr3-F7	2.455(1)	2.452(1)	2.440(1)	2.449(1)	2.453(2)	2.416(1)	2.444(1)	2.433(1)
Sr3-F8	2.608(2)	2.609(1)	2.665(2)	2.627(2)	2.609(2)	2.611(2)	2.619(1)	2.707(1)
Sr3-F10	2.898(1)	2.894(2)	2.897(2)	2.901(1)	2.895(2)	2.891(2)	2.924(1)	2.878(1)
Average	2.593	2.592	2.594	2.592	2.590	2.587	2.598	2.593
Na1-F1 (x2)	2.179(2)	2.179(2)	2.193(2)	2.179(2)	2.173(2)	2.185(3)	2.194(1)	2.195(2)
Na1-F4 (x4)	2.418(1)	2.416(1)	2.394(1)	2.411(1)	2.416(2)	2.412(2)	2.413(1)	2.377(1)
Average	2.338	2.337	2.327	2.334	2.335	2.299	2.304	2.316
Na2-F1 (x2)	2.194(2)	2.193(2)	2.114(2)	2.158(2)	2.188(2)	2.187(3)	2.198(1)	2.049(2)
Na2-F8 (x4)	2.250(2)	2.244(2)	2.182(2)	2.213(2)	2.239(2)	2.239(2)	2.266(1)	2.110(2)
Average	2.232	2.227	2.159	2.195	2.222	2.213	2.232	2.090

*Not reported as «true bonds by the literature (Hawthorne, 1983; Hawthorne and Bursn, 1997)

6.4.2.1 Jørgensentie

The seven jørgensenite experiments, all display somewhat similar bond lengths for the five cation sites. The *Sr2*-site show the largest variation, between 2.694 Å (exp. 730) to 2.749 Å (exp. 804) if the site is assumed 9-coordinated, and between 2.759 Å (exp. 730) to 2.807 (exp. 804) if the site is assumed 11-coordinated. The average bond length of the *Sr1*- and *Sr2*-sites are nearly identical between the seven experiments, with the bond lengths of the *Sr2*-site being on average the longest. The shortest average bond lengths are found at the *Sr3*-site. The *Na*-

sites show some variation in bond lengths, with exp. 702 and exp. 804 having the shortest average bond length of 2.299 Å and 2.304 Å, of the *Na2*-site.

Table 6.13 presents the polyhedron volume of the same cationic sites as Table 6.12. Since the polyhedron volume is calculated from the bond distance, the same pattern of variation as with the bond distances themselves is noticeable, between the individual experiments. From the bond lengths in Table 6.12, one would expect the polyhedron volume to increase in size from *Sr3*-site < *Sr1*-site < *Sr2*-site. The polyhedron volume show that the *Sr2*-site is in fact the smallest, closely followed by the *Sr3*-site. The *Sr1*-site has the greatest polyhedron volume, but also the greatest variation, from 36.200 $Å^3$ (exp. 729) to 37.206 $Å^3$ (exp. 804).

There is also a variation between the *Sr2*- and *Na2*-sites between the individual jørgensenites. Experiment 804 have overall the largest polyhedron volumes of the seven experiments, and the polyhedron volume of the *Sr2*-site in exp. 804 is considerably larger than in the six other jørgensenite. The same trend is seen in both 9- and 11-coordination.

The variation in polyhedron volume seems to be the greatest at the *Na*2-site, and Fig. 6.13 shows a plot of the polyhedron volume of the *Na*2-site against the length of the *a*-axis. From the plot it can be seen that there exists a positive trend of increasing length of the *a*-axis with an increase in the polyhedron volume of the *Na2*-site.

Table 6.13: Polyhedron volume ($Å^3$) and coordination number for the *Sr*- and *Na*-sites

	Mineral	Jør	Jør	Jør	Jør	Jør	Jør	Jør	Jør
	Exp.	557	711	729	730	686	702	804	699
Sr1	CN:10	36.692	36.684	36.220	36.238	36.436	36.757	37.206	35.644
Sr2	CN: 9	31.880	31.796	31.858	31.374	31.442	31.888	33.471	30.803
Sr2	CN: 11	45.842	45.733	45.954	45.297	45.297	45.884	47.719	44.759
Sr3	CN:9	33.296	33.150	33.371	33.221	33.168	33.227	33.610	33.235
Na1	CN: 6	15.754	15.728	15.715	15.670	15.649	15.746	15.998	15.524
Na1	CN: 6	14.318	14.225	13.073	13.683	14.155	14.127	14.535	11.936

6.4.2.2 Jarlite

The bond lengths of the *Na*- and *Sr*-sites in jarlite are presented in the last column of Table 6.12. The majority of the bond lengths are similar to the lengths found in jørgensenite, and only a small difference can be observed between the bond lengths of the *Sr1*-, *Sr3*- and *Na1*-sites, which are shorter in jarlite. Additionally, both the *Sr2*-site and the *Na2*-sites have shorter bond lengths in jarlite than they do in jørgensenite. These differences are more readily observable in Table 6.13, where it can be seen that all of the cation sites have a smaller polyhedron volume in jarlite than they do in jørgensenite, and the largest difference is found at the *Sr2*- and *Na2*-sites.

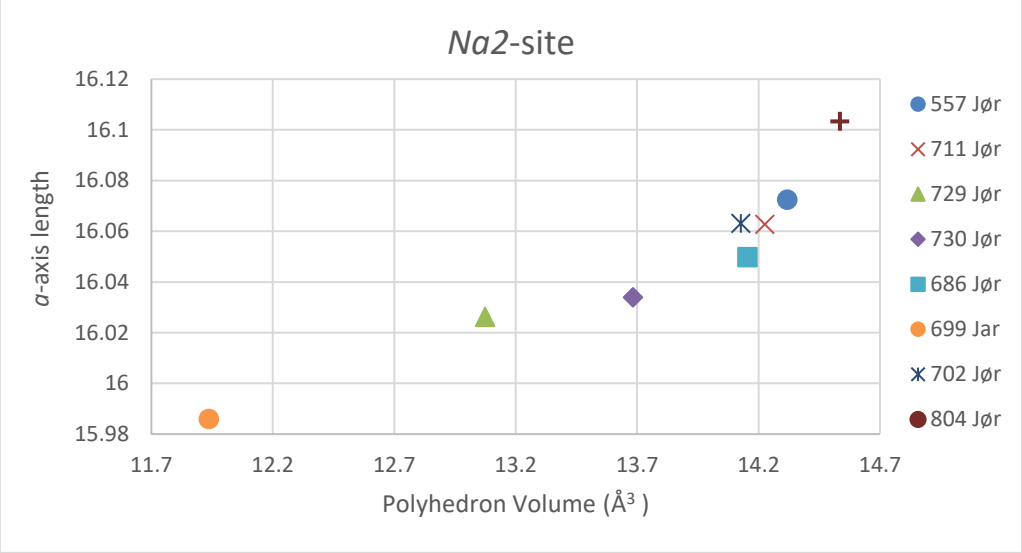

Figure 6.13: The polyhedron volume of the *Na2*-site plotted against the *a*-axis length of the unit cell. There is an overall positive correlation.

6.4.3 RSS-factors

Table 6.14 presents the refined site-scattering (RSS) factors for all of the cation-sites. The RSS should ideally yield a number close to the number of electrons found in the site-assigned element. For the three *Sr*-sites, the *Sr2*-sites have RSS-factors which is consistently higher than the ideal number (38*e* for Sr), while for the *Sr3*-sites they are consistently lower. The RSS-factors of the *Sr1*-sites shows no particular trend, but they are all close to their ideal value. The

Na1-sites have RSS-factors consistently lower, while the *Na2*-positions have consistently higher than the ideal value of 11*e*, except for exp. 730 and exp. 804 in which they are both less than ideal. Both the *Al*-sites have RSS-factors lower than their ideal values of 13*e*. This holds true for all the experiments, but at varying degrees. Notice that for the jarlite experiment (699), the RSS factor based on Mg occupancy of the *Na2*-site is presented.

Table 6.14: Refined site-scattering (RSS) factors for the cation sites in *e*

Mineral	**Exp.**	*Sr1*	*Sr2*	*Sr3*	*Na1*	*Na2*	*Al1*	*Al2*
Jør	557	39.801	44.235	37.402	10.720	11.116	12.782	12.783
Jør	711	39.938	44.277	37.259	10.545	11.195	12.744	12.643
Jør	729	37.766	41.721	36.037	10.460	11.240	12.628	12.587
Jør	730	38.048	39.819	36.907	10.490	10.718	12.799	12.631
Jør	686	38.620	41.789	37.256	10.769	11.036	12.710	12.581
Jør	702	40.727	44.142	37.188	10.416	11.035	12.851	12.625
Jør	804	39.286	53.334	36.841	10.885	10.853	12.736	12.700
Jar	699	37.919	35.842	36.141	10.532	11.449*	12.692	12.578

*Calculated based on Mg

6.4.4 Bond Valence Sums

Tables 6.15, 6.16 and 6.17 present the calculated bond valence sums for three of the experiments conducted. Table 6.15 and 6.16 present the bond valence sums of two jørgensenites, exp. 729 and exp. 804. The reason behind why these two were chosen, was that they represent two different types of jørgensenite, with different unit cell lengths and occupancy of Ba. Table 6.17 presents the bond valence sums of jarlite (exp. 699). The bond valence sums were calculated using the formula,

$$BVS = e^{\frac{R_0 - R_i}{b}} \qquad (6.1)$$

where R_i is the observed bond lengths, R_0 and b are calculated parameters, where the latter has a constant value of 0.37 (Brown, 2009). R_0 are also constants but varies depending on the elements. A series of revised R_0-values were calculated by Gagné and Hawthorne (2015), but these are solely based on O as the anion. This means that the possibly outdated R_0-values of Brese and O'Keeffe (1991) had to be used.

6.4.4.1 Jørgensenite

There are some similarities between the bond-valence sums presented in the two Tables 6.15 and 6.16 for jørgensenite. Both the *Sr1*-position, and the two *Al*-positions are similar, and their sums of charges are quite close to the ideal charges of 2 and 3, respectively.

The bond valence sums of the *Sr2*- and *Sr3*-site for exp. 729 are less than their ideal sum of 2. Experiment 729 have a bond valence sum of 1.67 for the *Sr2*-site and 1.58 for the *Sr3*-site. Experiment 804 is closer to the ideal charge of 2 for both the *Sr2*-site and the *Sr3*-site, with bond valence sum of 1.94 and 2.05, respectively.

The two additional bonds which was introduced in Table 6.12, have also been assigned the *Sr2*-position of exp. 804 and exp. 729 in Tables 6.15 and 6.16.

Table 6.15: Bond-valence sums for exp. 729, jørgensenite

Site	*Sr1*	*Sr2*	*Sr3*	*Na1*	*Na2*	*Al1*	*Al2*	**Sum**
F1			0.24	$0.20^{2x}\downarrow$	$0.28^{2x}\downarrow$			0.96
F2		0.19	0.09			0.49		0.85
F3	$0.29^{2x}\downarrow$					0.52		0.81
F4		$0.20^{2x}\downarrow$	0.21	$0.12^{4x}\downarrow$			0.48	1.00
F5a		$0.12^{2x}\downarrow$	0.19			$0.47^{2x}\downarrow$		0.97
F5b			0.19					
F6		$0.16^{2x}\downarrow$	0.21				0.53	0.90
F7	$0.09^{4x}\downarrow$		0.25				0.53	0.87
F8		$0.06^{2x}\downarrow$	0.13		$0.23^{4x}\downarrow$		0.48	0.91
F9						$0.46^{2x}\downarrow$	0.43	0.89
F10	$0.26^{4x}\downarrow$	$0.21^{2x}\downarrow$	0.07				0.47	1.00
Sum	1.95	1.67	1.58	0.86	1.50	2.87	2.92	

The *Na1*-site show a small deficiency in its bond valence sum (0.86), for exp. 729, while it is near ideal for exp. 804. The main difference in bond valence sums is found at the *Na2*-site. Experiment 804 have a bond valence sum for the *Na2*-site of 1.30, which is somewhat above the ideal value of 1, while exp. 729 have significantly larger bond valence sum of 1.5.

The *F*-sites show a variety of bond valence sums, but the majority fall within a 10% interval of the ideal sum of 1.

Table 6.15: Bond-valence sums for exp. 804, jørgensenite

Site	*Sr1*	*Sr2*	*Sr3*	*Na1*	*Na2*	*Al1*	*Al2*	**Sum**
F1			0.29	$0.24^{2x\downarrow}$	$0.24^{2x\downarrow}$			0.97
F2		0.22	0.11			0.50		0.91
F3	$0.28^{2x\downarrow}$					0.52		0.75
F4		$0.23^{2x\downarrow}$	0.28	$0.13^{4x\downarrow}$			0.47	1.07
F5a		$0.16^{2x\downarrow}$	0.27			$0.46^{2x\downarrow}$		1.07
F5b			0.26					
F6		$0.19^{2x\downarrow}$	0.27				0.54	0.95
F7	$0.08^{4x\downarrow}$		0.33				0.53	0.87
F8		$0.08^{2x\downarrow}$	0.16		$0.20^{4x\downarrow}$		0.50	0.91
F9						$0.46^{2x\downarrow}$	0.43	0.90
F10	$0.26^{4x\downarrow}$	$0.24^{2x\downarrow}$	0.10				0.46	1.00
Sum	1.90	1.94	2.05	0.99	1.30	2.86	2.93	

6.4.4.2 Jarlite

The bond valence sums of the jarlite experiment (699), presented in Table 6.17, show similarities with the *Sr1*-site and the two *Al*-sites of jørgensenite. The *Sr1*-site sum up to an ideal bond valence sum of 1.99, while the two *Al*-sites have a somewhat lower than ideal bond valence sums of 2.90 and 2.92. The bond valence sum of the *Na1*-site (0.90) and Mg2-site (1.83) are also quite close to their ideal values of 1 and 2.

The *Sr2*-site and *Sr3*-site both have deficient bond valence sums, with the *Sr2*-site having the lowest sum of 1.67, which is quite far from the ideal value of 2. The bond valence sum of the *Sr3*-site (1.60) is similar to the on for exp.729 (1.57). The *F*-sites show a variety of bond valence sums, with most of them being within a 10% interval of the ideal value of 1, similar to exp. 729 and exp. 804.

Table 6.16: Bond-valence sums for exp. 699, jarlite

Site	*Sr1*	*Sr2*	*Sr3*	*Na1*	*Mg*	*Al1*	*Al2*	**Sum**
F1			0.23	$0.20^{2x\downarrow}$	$0.34^{2x\downarrow}$			0.99
F2		0.19	0.09			0.49		0.86
F3	$0.29^{2x\downarrow}$					0.53		0.82
F4		$0.19^{2x\downarrow}$	0.28	$0.12^{4x\downarrow}$			0.48	1.01
F5a		$0.10^{2x\downarrow}$	0.21			$0.48^{2x\downarrow}$		1.00
F5b			0.20					
F6		$0.18^{2x\downarrow}$	0.21				0.54	0.92
F7	$0.10^{4x\downarrow}$		0.25				0.54	0.89
F8		$0.05^{2x\downarrow}$	0.12		$0.29^{4x\downarrow}$		0.46	0.87
F9						$0.46^{2x\downarrow}$	0.43	0.89
F10	$0.25^{4x\downarrow}$	$0.22^{2x\downarrow}$	0.08				0.47	1.02
Sum	1.99	1.67	1.60	0.90	1.83	2.90	2.92	

7 Discussion

7.1 Refinement Results

In order to discuss the site-population of jarlite and jørgensenite, some discussion concerning the refinement of the crystal structures are in order. When performing a crystal structure refinement, the GooF and the Residual-factors (R-factors) are used as indicators of how well the structure has been refined. The R-factors should converge towards a minimum during the refinement, and the smaller they are at the end of a completed refinement, the better. The reason behind this, can be easily demonstrated by using the formula of the simplest of the R-factors, the R1 (formula 1).

$$R1 = \frac{\sum||F_O|-|F_c||}{\sum|F_O|} \qquad (7.1)$$

It can be seen from formula 1, that the R1-factor is simply the sum of the absolute value of the observed structure factor minus the absolute value of the calculated structure factor, divided by the sum of the absolute value of the observed structure factor. This means that a refinement will be successful if the calculated structure factor of the refined crystal structure converges towards the observed structure factor (Massa, 2000; Müller, 2006).

The GooF on the other hand, acts as an indicator of how well the refined structure matches that of the initial observed structure, which means that acceptable values are in the range 1±0.1.

$$GooF\ (S) = \left[\frac{\sum w(F_o^2-F_c^2)^2}{(N_R-N_P)}\right]^{1/2} \qquad (7.2)$$

As with the R1-factor, F_o is the observed structure factor, while F_c is the calculated structure factor. The w is a weighting factor, which marks the trustworthiness of each single reflection and is derived from a set of standard uncertainties related to the measured reflections. N_R is the number of independent reflections, while N_P is the number of refined parameters (Müller, 2006).

As can be seen in Table 7.1, experiment 729, 686, 702, 804 and 699 are within this range, while experiment 730 are just outside of it, and experiment 557 and 711 are far off. The problem with

experiment 557 and 711, began when the *Sr*-positions were opened and assigned dual occupancy with Ba. This had an immediate impact on the GooF and increased it from ~1.1 to ~1.3, at the same time as it lowered the Final R1-parameter.

Table 7.1: Refinements-parameters from table x.

Min.	**Jør**	**Jør**	**Jør**	**Jør**	**Jør**	**Jør**	**Jør**	**Jar**
Exp.	**557**	**711**	**729**	**730**	**686**	**702**	**804**	**699**
R(int)	0.0279	0.0311	0.0309	0.0494	0.0461	0.0678	0.0224	0.0197
Final R1	0.0252	0.0269	0.0255	0.0275	0.0363	0.0351	0.0202	0.0262
wR2	0.0440	0.0390	0.0627	0.0560	0.0591	0.0650	0.0357	0.0420
GooF	1.340	1.215	1.090	1.178	1.085	1.080	1.094	1.107

A high GooF can often indicate that there is some sort of problem with the absorption correction that was performed during the data integration. Experiment 711 was therefore reopened in CrysalisPro and assigned a new and more precise face index absorption correction. A new chemical formula was used for absorption correction with 1.5 apfu of Ba. The new dataset was then refined anew, but the problem with the high GooF persisted. It was then decided that the entire experiment should be rechecked. During the revaluation of the dataset, no serious violations were found among the collected reflections, but some reflections that may originate from a potential twin was found in the Ewald Explore software. The twin was identified by CrysalisPro to be related to the main crystallographic domain by a 180° rotation around a (-1 0 0.5)-axis. Even though this seemed to be an erroneous twin domain, an attempt was made to solve it as a twinned structure. It became evident during the integration that this assumption was correct, when CrysalisPro proposed a F-centred unit cell and gave an R(int)-value of 0.4 when forced to the correct monoclinic C-centred unit cell. This would most likely suggest that the additional crystallographic domain found, was not a true twin, but more likely a tiny fragment attached through surface cohesion. This attempt was therefore discarded and the problem with the high GooF still persisted.

It was later decided that exp. 557 and 711 should be tested with different background corrections, a Standard Background correction and a Smart Background correction, in order to see if this could influence the GooF. This was first conducted on exp. 804, where the GooF

changed from 1.191 (Standard Background) to 1.094 when using a Smart Background. Since the choice of background had an immediate effect on the Goof, it was decided to try a Smart Background correction on exp. 557 and 711. For exp. 557 the change of background from standard to smart, had a small, but not truly significant impact on the GooF from 1.400 to 1.340. For exp. 711, the opposite occurred, and the Smart Background correction raised the GooF from 1.215 (standard) to 1.260 (smart).

The choice of background can therefore have an impact on the integration of the dataset, and that the choice between Smart- and Standard Background corrections needs to be evaluated independently. Regarding exp. 557 and 711, the problem with the GooF can most likely be attributed to the additional crystallographic domains found with the Ewald Explorer Software.

7.2 Chemical Results

The results from the EPMA-analysis display a varying degree of precision. The nature of the imprecise results is caused by the high degree of chemical heterogeneity found within the samples. It is evident from Fig. 6.1 that the massive jørgensenite found throughout several of the samples, in fact are multiple fan-shaped aggregates with different orientations that has grown together to form a continuous matrix. This type of growth seems to have left several interstitial voids, which have been filled by jarlite, similar to the growth sequence of the core and mantle features displayed in Fig. 6.7. Some of these void fillings also display a higher degree of BSE-brightness, which indicates a slightly elevated concentration of Ba, as compared to the jørgensenite matrix.

The described morphology is believed to be the main cause of the imprecisions displayed in the chemical data. The intergrowth of fan-shaped aggregates is difficult to distinguish, even when performing BSE-imaging in high vacuum. This can be seen in Fig. 7.2, where the contrast had to be elevated in order for these features to appear. However, some problems could be attested to analytical errors. Especially the measured concentration of Na seems to be lower than would be expected, especially if compared to the EPMA- data of Pauly and Nielsen (1992).

However, these levels of imprecisions recorded act as an interesting result in itself and attest to the fact that most jørgensenite and jarlite are highly heterogeneous in their content of minor elements, and that varying degrees of substitution is common. Additionally, the imprecise

concentrations of the minor elements, could be used as an indication of what range of concentration would be expected, when evaluating the site-population. This gives a higher degree of freedom when conducting the site-assignment, at the same time as it restricts the degree of certainty of any conclusions.

7.3 Site-assignment

To gain further insight into the crystal structure but also the nature of jørgensenite and jarlite, it is important that a deeper understanding of the crystal chemistry is obtained. The site-assignment of Hawthorne (1984) and Hawthorne and Burns (1997) gives a good indication as to the crystal chemistry of jarlite and jørgensenite, but their conclusions lack the necessary detail to be considered satisfactory. The following sections will therefore discuss the nature of the different sites within the crystal structure of jarlite and jørgensenite.

7.3.1 *Al*-sites

The *Al*-sites are six-coordinated and form isolated Al-trimers with the sequence *Al2-Al1-Al2*. The average Al-F bond length is between 1.81 and 1.82 for the two sites, which is close to the ideal bond length between six-coordinated Al and four-coordinated F of 1.85 (Shannon, 1976).

Both the Bond-Valence Sums (BVS) and the Refined Site Scattering (RSS)-factors of the *Al*-sites are slightly below their ideal values (Tables 6.14, 6.15, 6.16 and 6.17). The BVS are however close enough to indicate that the *Al*-sites are fully occupied by trivalent cations and that the sites are six-coordinated. The slightly deficient RSS-factor could indicate that a lighter atom is present, however, there does not exist any lighter trivalent cation, which would also satisfy the bond length. The RSS-factor could also be attributed to partial vacancy, which in such a case would amount to a partial vacancy of 1-3%, but it could also be considered close enough to the ideal value, so that the discrepancy could be attributed to analytical errors. It is therefore likely that the *Al*-sites are fully occupied by aluminium.

7.3.2 *Na1*-site

The *Na*1-site is 6-coordinated to F and have average bond lengths of 2.3 Å. The *Na*1-site show an interesting behaviour in the structure. The RSS factors for this site are consistently less than the ideal value of 11*e*, and the bond-valence sums are consistently less than the ideal value of

1, except for exp. 804 (see Table 7.2). The deficient RSS-factors indicate that the site is shared between Na and an atom with less electrons or vacancies. The combination of a deficient electron count and low BVS indicates that the *Na1*-site is partially vacant.

However, it seems unlikely that this is the case. From the chemical data of jarlite and jørgensenite (Tables 6.3 and 6.7), it is evident that the average Na-content is too high to justify the idea that a distinct *Na*-site would favour partial vacancy.

There is another possibility as to why the RSS-factor of the *Na1*-site show systematic deficiency in the number of electrons. In the original publication on jarlite, 0.04 - 0.08 wt% (400-800 ppm) of Li was measured (Bøgvad, 1933). Later research has omitted Li, due to the inability of detecting it with the EPMA (Pauly and Nielsen, 1992), but the occurrence of cryolithionite do suggest that Li was available during the evolution of the cryolite deposit (Geller, 1971; Pauly, 1986). Additionally, the fluid-inclusions study of Köhler et al (2008), found that the first stage cryolite contained fluid inclusions with up to 3000 ppm of Li and second stage fluorite which contained 100-800 ppm of Li. Cryolithionite most likely formed from first stage cryolite (Pauly, 1986), which means that it is the fluid inclusions of the second stage fluorite that is the most relevant in the case of jarlite and jørgensenite.

A minor content of Li could explain why the *Na1*-site fails to achieve ideal RSS-factors and BVS. Due to the low atomic weight of Li, as little as 0.04 wt% would result in a Li-content of 0.17 *apfu*. The *Na1*-site of the jarlite sample (exp. 699) has an RSS-factor of 10.53, which can be achieved if the site is shared between 94% Na and 6% Li, resulting in a possible Li-content of 0.12 *apfu*. Table 7.2 presents the calculated theoretical proportion of Li in the *Na1*-site, along with the corresponding *apfu*. As can be seen from the table, none of the calculated *apfu*-values exceed the value of 0.34 *apfu* measured by Bøgvad (1933), with the highest being 0.15 *apfu* for exp. 702. This suggests that there could be validity to a minor amount of Li substituting for Na at the *Na1*-site. This is further supported by the new bond-valence sums presented in Table 7.2, calculated from the theoretical occupancy. The new bond-valence sums for the *Na1*-site of exp. 729 and 699, are closer to their ideal value, with values of 1.01 and 1.04, compared to the old ones of 0.86 and 0.90. Exp. 804 seem to be a *Na*1-site with full occupancy of Na and the BVS show little difference from the former.

Table 7.2: RSS-factor, Occupancy of Li, and BVS for the *Na1*-site

Mineral	Exp	RSS	Occ. Li (%)	*apfu*	Old BVS	New BVS[1]
Jør	557	10.72	3.4	0.07	0.94	1.02
Jør	711	10.55	5.7	0.11	0.88	1.01
Jør	729	10.46	6.8	0.14	0.86	1.01
Jør	730	10.49	6.4	0.13	0.86	1.01
Jør	686	10.77	3.0	0.06	0.97	1.04
Jør	702	10.42	7.3	0.15	0.83	0.99
Jør	804	10.89	1.5	0.03	0.99	1.03
Jar	699	10.53	5.8	0.12	0.90	1.04

1: New bond-valence sum calculated based on the occupancy reported in column 4.

This suggest that minor amounts of Li could be substituting for Na at the *Na1*-site. However, it is important to stress that without chemical data which verify the presence of Li, this discussion is purely theoretical. An additional problem with this suggestion, is that similar to the possibility of partial vacancy, an additional content of Li, would result in empirical formulas which have a further increased excess of cations, especially for jarlite. The empirical formulas for jørgensenite however, have a deficiency of up to 0.61 *apfu* at the *Na2*-site, which would mean that in the case of excess Na at the *Na1*-site, this can be hosted in the *Na2*-site without imposing any problems.

7.3.3 Na2/Mg-site

One of the major differences between the isostructural minerals jarlite and jørgensenite is their concentration of Mg. From the literature, jørgensenite is described as mostly Mg-free, while jarlite has a Mg-content of 2 to 4 *apfu*, and a distinct *Mg*- site in its crystal structure (Hawthorne, 1983; Pauly and Nielsen, 1992; Pauly et al. 1997; Hawthorne and Burns, 1997; Hawthorne and Hartwig, 2021). This difference has been used during the work on this thesis to distinguish between the two minerals while working on the SEM and EPMA.

Hawthorne (1983) defined the *Mg*-site in jarlite as a partially filled site, governed by the substitution mechanism,

$$\square + 2H_2O \leftrightarrow Mg + 2(OH) \qquad (7.3)$$

where the two *O1*-sites bonded to the *Mg*-site, changed between being occupied by H_2O or OH, according to the occupancy of Mg. After the discovery of jørgensenite, this idea partially changed as to also include substitution between Na and Mg, as it was found that the *Mg*-site in jarlite was a *Na*-site in jørgensenite, containing dual occupancy of Na and Mg (Pauly et al. 1997). However, the main theory of vacancy at the *Mg*-site still persists (Hawthorne and Hartwig, 2021).

As was presented in Table 6.6, the Mg-content of jarlite is consistently less than the ideal value of 2 *apfu*, which could indicate that the *Mg*-site is partially vacant in accordance with Hawthorne (1983). However, the Na-concentration is too high to only occupy the *Na*1-site and the *Sr*-sites, similar to what was found by Pauly and Nielsen (1992). Additionally, as will be discussed in Section 7.3.7, the *O1*-site described in Hawthorne (1983) are in fact a *F1*-site, and the F-O substitution occurs over multiple sites within the crystal structure. Consequently, if the *Mg*-site were to be vacant, there would be no H_2O-molecule at this site, which could form hydrogen-bonds to the then partially unbonded *F8*-site, as originally suggested by Hawthorne (1983).

It therefore seems unlikely that the *Mg*-site in jarlite is partially vacant. A more likely scenario is that the *Mg*-site in jarlite is fully occupied, with dual occupancy of Mg and Na. This would also explain why Pauly and Nielsen (1992) were unable to present an empirical formula in agreement with both the theoretical formula of Hawthorne (1983) and their own EPMA-data.

The *Na*2/*Mg*-site is 6-coordinated to F and have average bond lengths of 2.2 Å for jørgensenite and 2.1 Å for jarlite. The RSS-factor for the *Na2/Mg*-site first presented in Section 6.4.3, are reproduced for this section as Table 7.3. It can be seen from the RSS-factors, that most of the values for the *Na*2/*Mg*-site falls close to the ideal electron count of 11*e*. The RSS-factors for all of the jørgensenite experiments are quite near to their ideal value, and it seems unlikely that the site-population should include any significant vacancies or major contribution from another element. However, there could be a small contribution of Mg, as was found in Pauly and Nielsen (1992). This is supported by the range of different polyhedron volumes recorded for the *Na2*-site in jørgensenite (Fig. 6.13). Additionally, an undistorted Mg-F octahedron have an ideal volume of 11.15 $Å^3$, while a Na-F octahedron have an ideal volume of 16.6 $Å^3$. If these values are compared to the ones in Table 6.13, it seems likely that some Mg is present, which contributes towards a decrease in the polyhedron volume.

However, this is in contradiction to the chemical data presented in Table 6.2 of this thesis. It also brings to question whether Na have been successfully measured with the EPMA, since none of the RSS-factors gives any strong indications towards partial vacancy or shared occupancy, as the empirical formulas of Tables 6.3, suggests.

The jarlite crystal structure shows a different behaviour, and the RSS-factor of the *Mg*-site is lower than what is to be expected from full Mg-occupancy (12*e*), with a value of 11.449*e*. This value corresponds to a site-population of 40% Mg and 60% Na, or 95% Mg and a 5% vacancy. When the latter value was used to calculate the BVS of the *Mg*-site, the result was a BVS of 1.2, while the dual occupancy of Mg and Na gave 1.83 (Table 6.16). Consequently, it seems more likely that the *Mg*-site in jarlite experiences dual occupancy with Na, rather than partial vacancy as suggested by Hawthorne (1983). However, it seems likely that the RSS-factor underreports the contribution of Mg, since the polyhedron volume of Table 6.13 indicate that Mg should dominate the site.

Table 7.3: RSS-factors for the *Na2*/*Mg*-sites

Mineral	Jør	Jør	Jør	Jør	Jør	Jør	Jør	Jar
Exp.	557	711	729	730	686	702	804	699
Na1-site	11.116	11.195	11.240	10.718	11.036	11.035	10.853	11.449

7.3.4 *Sr1*-site

The *Sr*1-site is 10-coordinated to F and have average bond lengths between 2.65 and 2.7 Å. The *Sr1*-site display a somewhat consistent behaviour through all of the examined structures. Both the RSS-factors and the BVS presented in Tables 6.14, 6.15 and 6.16 are in agreement with full occupancy of Sr, and the average bond-lengths (Table 6.12) are also in agreement with the ideal bond length for 10-coordinated Sr bonded with 4-coordinated F (2.67 Å) (Shannon, 1976). It is therefore unlikely that other atoms are involved in the site-population of the *Sr1*-site.

However, the RSS-factors of exp. 557, 711, 702 and 804 indicates that these have a small surplus of electrons at the site (Table 6.14), which could be attributed to a small addition of Ba to the *site*-population. However, 10-coordinated Ba have an ideal bond length to F of 2.82 Å, which means that the observed bond lengths for the *Sr1*-site are slightly shorter than would be expected if the Ba-contribution was significant (Shannon, 1976). There do however seem

to be a difference between the polyhedron volumes of jørgensenite and jarlite for this site. The *Sr1*-site in jarlite (exp. 699), have a somewhat smaller polyhedron volume of 35.644 Å^3, compared to a volume between 36.2 and 37.2 Å^3 for jørgensenite. If the *Sr1*-site in jarlite is acknowledged as a pure *Sr*-site, which is supported by the BVS and RSS-factor, the increase in polyhedron volume in jørgensenite could be attributed to a site-population of both Sr and small amounts of Ba.

7.3.5 *Sr2*-site

7.3.5.1 Jørgensenite

The *Sr*2-site is 9-coordinated to F and have average bond lengths around 2.7 Å. The *Sr2*-site have been treated somewhat different from the other sites in the crystal structure of jarlite and jørgensenite. It became obvious during the refinement of the crystal structure data, that this site was affected by Sr-Ba substitution, due to the RSS-factors produced when the occupancy was assigned a free-variable factor. The RSS-factors (Table 6.14), indicate that the site-population of the *Sr2*-site contain shared occupancy between Sr and a heavier atom, which in this case must be Ba. All of the jørgensenite experiments were therefore refined with shared occupancy between Sr and Ba at the *Sr2*-site (Table 7.4)

Dual occupancy between Sr and Ba is supported by the bond lengths. 9-coordinated Sr and Ba have ideal bond lengths of 2.62 Å and 2.78 Å, respectively (Shannon, 1976). The average observed bond length for this site seems to be an intermediary between the ideal lengths (6.12).

Table 7.4: The Occupancy of Ba, RSS-factor and Polyhedron Volume for the *Sr2*-site

Mineral	Exp	RSS	Occ. Ba	*Sr2-F8* (Å)	PV (Å^3) CN: 9	PV (Å^3) CN: 11
Jør	557	44.235	0.326	3.096(2)	31.880	45.842
Jør	711	44.277	0.286	3.095(2)	31.796	45.733
Jør	729	41.721	0.187	3.112(2)	31.858	45.954
Jør	730	39.819	0.095	3.102(2)	31.374	45.297
Jør	686	41.789	0.179	3.100(2)	31.442	45.297
Jør	702	44.142	0.325	3.099(2)	31.888	45.884
Jør	804	53.334	0.858	3.094(1)	33.471	47.719
Jar	699	35.842	-	3.135(2)	30.803	44.759

The additional bonds between the *Sr2*-site and the *F8*-site, which was first introduced in Table 6.12, are presented in Table 7.4, together with the occupancy of Ba. The distance between *Sr2* and *F8* has not been reported in the literature, since it was not considered to be a true bond (Hawthorne, 1983; Hawthorne and Burns, 1997). When the bond distances between the *Sr2*-site and the *F8*-site are compared to the occupancy of Ba, one sees that the bond-distance decreases with an increase of Ba. The ideal bond distance between an 11-coordinated Ba and a 4-coordinated F, is 3.06 Å (Shannon, 1976), and it can be seen from Table 7.4, that the bond lengths decrease towards 3.06 Å with an increasing content of Ba. This indicates that the bonding interaction between the *Sr2*-site and the *F8*-site increases, when the content of Ba increases. This suggest that the *Sr2*-site should be recognized as a 11-coordinated site, in contrast to the findings of Hawthorne (1983) and Hawthorne and Burns (1997). This would explain why the *Sr2*-site experiences the highest degree of Sr-Ba substitution, since neither the *Sr1*-site nor the *Sr3*-site have the necessary surroundings to be able to transform into a higher coordination.

A coordination number higher than 9 seems to be preferable for Ba, which is also the case for the related Ba-aluminofluoride usovite and possibly also bøgvadite (Litvin et al, 1980; Balić-Žunić; Weil, 2015). Balić-Žunić (2014) reports Ba in bøgvadite as 8-coordination. A calculation of the BVS of the Ba-site in bøgvadite gave a sum of 1.75, indicating that some significant bonding interactions may be lacking. Since the *Ba*-site in bøgvadite is identical to the *Sr2*-site in jørgensenite (Balić-Žunić, 2014), it is not unreasonable to assume that the true coordination number of Ba in bøgvadite should be closer to 11. Furthermore, experiment 804 has a polyhedron volume of 47.719 $Å^3$ when 11-coordinated, which is comparable to the polyhedron volume of the 11-coordinated Ba in usovite, 48.572 $Å^3$ (Litvin et al, 1980).

7.3.5.2 Jarlite

The RSS-factor of exp. 699 (jarlite) show an interesting difference from the jørgensenite experiments. Whereas the crystal structure of all the jørgensenite show a surplus of electrons for the *Sr2*-site, the crystal structure of jarlite has a deficiency. The *Sr2*-site in jarlite also has the smallest polyhedron volume of 30.803 $Å^3$ (CN 9). When comparing this volume to the polyhedron volume of exp. 730 (31.374, CN 9), the jørgensenite with the lowest occupancy of Ba, this could simply be the true volume of a Ba-free *Sr2*-site. However, the RSS-factor do not support full occupancy of Sr, and an RSS-factor of 35.84*e* indicate that the *site*-population

include additional elements. It could also indicate partial vacancy, but this seems unlikely based on the empirical formulas of Table 6.7, and those of Pauly and Nielsen (1992).

A potential candidate for the *site*-population is Ca. 11-coordinated Ca have been found to have bond lengths between 2.279 to 2.965 Å (Gagné and Hawthorne, 2016), which are within the range of the bond lengths found for the *Sr2*-site (Table 6.12). However, Gagné and Hawthorne (2016) worked primarily on cations bound to O^{2-} and since F^{-} has a greater electronegativity than O^{2-}, the mean bond distances would most likely be somewhat shorter.

Furthermore, this is supported by the correlation between the CSS-factor and the RSS-factor. A CSS-factor of 35.84*e* was calculated from a shared site containing 12% Ca and 88% Sr. A Ca-concentration of 12 % (0.48 *apfu*) are in accordance with the measured concentration (Table 6.6) and with the literature (Hawthorne, 1983; Pauly and Nielsen 1992). However, a new BVS calculated from this occupancy-ratio yielded a sum lower to the one calculated based on full occupancy of Sr (see Table 7.5). A site-population of Sr, Ba and Ca was also tested for jørgensenite, leaving an almost identical result to that calculated for a site-population of only Sr and Ba.

Table 7.5: RSS, CSS and BVS values and theoretical occupancies for the *Sr2*-site

Mineral (exp.)	RSS	CSS	Occ. Ba	Occ. Ca	Old BVS	New BVS[1]
Jør (557)	44.2	44.3	0.42	0.07	1.80	1.80
Jør (711)	44.3	44.3	0.42	0.07	1.78	1.82
Jør (729)	41.7	41.8	0.31	0.1	1.67	1.69
Jør (730)	39.8	39.8	0.17	0.07	1.66	1.67
Jør (686)	41.8	41.8	0.31	0.1	1.73	1.75
Jør (702)	44.1	44.1	0.41	0.07	1.80	1.80
Jør (804)	53.3	-	0.86	-	1.94	-
Jar (699)	35.8	35.8	0.05	0.17	1.67	1.57

1: New bond-valence sum calculated based on the occupancy reported in columns 4 and 5.

This does not necessarily rule out the addition of Ca to the site-population of the *Sr2*-site. The lack of effect on the BVS, could be attributed to the short bond distances, ideally found between Ca and F, and that the wide range of bond distances found by Gagné and Hawthorne (2016),

are not truly considered when creating ideal BVS-parameters. However, whether Ca should be considered a part of the site-population for the *Sr2*-site or not, remains inconclusive.

Based on the RSS-factors for the *Sr*-sites in jarlite, it is probable that the jarlite crystal, which was analysed, is an example of a completely Ba-free jarlite, and additional experiments are required to further investigate the distribution of Ba and Ca in jarlite. Furthermore, there does exist a Ca- dominated jarlite, Calcjarlite, $Na(Ca,Sr)_3Al_3(F, OH)_{16}$, which was first described in 1973 (Povarennykh, 1973). Unfortunately, the only publication on calcjarlite is in Russian and no cif-files seems to be available for download. If it is true that calcjarlite is isostructural with jarlite (Hawthorne and Hartwig, 2021), then there is a possibility that the similarity between jarlite and calcjarlite can be found as Ca-substitution at the *Sr2*-site. However, additional data on the crystal structure of jarlite, and a revised publication on calcjarlite, are needed before anything can be concluded on this matter.

7.3.6 *Sr3*-site

The *Sr*3-site is 9-coordinated to F and have average bond lengths around 2.6 Å. Table 7.6 presents the RSS-factors, and the BVS for the *Sr3*-site, which were first presented in Tables 6.14, 6.15, 6.16 and 6.17, for both jørgensenite and jarlite. The RSS-factor for this site seems to be consistently lower than its ideal value of 38*e*, indicating that the site is either partially vacant, or shared between Sr and one (or more) elements with fewer electrons. The chemical data presented in Tables 6.2 and 6.6, as well as the data from Pauly and Nielsen (1992) indicate that both K and excess Na should be found as a part of the site-population of one of the *Sr*-sites. No indications of shared occupancy between Sr, Na and K have been found at neither the *Sr1*- nor the *Sr2*-site, and the *Sr3*-site remains as the most likely candidate.

This is supported by the bond lengths of the *Sr3*-site, of which the majority of the bond lengths are between 2.45 and 2.60 Å, which is close to the ideal bond length of 2.55 Å for 9-coordinated Na (Shannon, 1976). Potassium, on the other hand, have an ideal bond length of 2.86 Å when 9-coordinated (Shannon, 1976), making the majority of the bond lengths too short. However, 9-coordinated K have been found to have a range of bond lengths, measuring between 2.67 to 3.1 Å (Gagné and Hawthorne, 2016). This range fits the longer bond lengths (>2.7 Å) recorded for the *Sr3*-site, but the range of standard bond lengths should most likely be shorter, when F^- as an anion is considered.

The RSS-factor was attempted reproduced by testing different occupancy-ratios of K, Na and Sr, so as to find a CSS-factor as close as possible to the RSS-factor. The occupancy of Sr was held as high as possible, so as to replicate the site as Sr-dominated. However, no restrictions were enforced on the occupancy of Na and K, except that the total occupancy of Na, K and Sr should sum to 1. Column 4 presents the occupancy of K and Na that had a CSS-factor closest to the RSS-factor and column 5 presents the corresponding content (total *apfu* of Na + K). The overall trend seems to be that in order to reproduce the RSS-factor, the occupancy of K needs to be larger than the occupancy of Na, however exp. 557, 711 and 686 show an opposite behaviour. This relationship of a higher K-content than Na-content at the *Sr3*-site is in agreement with the *apfu*-values calculated from the EPMA-data in Table 6.6, which indicates that these occupancy ratios are reasonable.

Table 7.6: RSS, CSS and BVS values and theoretical occupancies for the *Sr3*-site

Mineral (exp.)	RSS	CSS	Occ. K (%)	Occ. Na (%)	*apfu*	Old BVS	New BVS[1]
Jør (557)	37.402	37.40	1.0	1.5	0.20	1.89	2.04
Jør (711)	37.259	37.27	1.0	2.0	0.24	1.87	2.05
Jør (729)	36.037	36.05	6.0	3.0	0.72	1.57	2.01
Jør (730)	36.907	36.89	3.0	2.0	0.4	1.78	2.02
Jør (686)	37.256	37.27	1.0	2.0	0.24	1.84	2.06
Jør (702)	37.188	37.16	3.0	1.0	0.31	1.87	2.05
Jør (804)	36.841	36.89	3.0	2.0	0.40	2.05	2.02
Jar (699)	36.141	36.13	7.0	2.0	0.72	1.60	1.99

The occupancy of K, Na and Sr were used to calculate new BVS for the *Sr3*-site. The BVS presented in Tables 6.15, 6.16 and 6.17 are reproduced here as column 6, Table 7.6. The old BVS are consistently below the ideal value of 2, except for exp. 804. This indicate that a monovalent cation could contribute to the site-population in the majority of the experiments. The new bond-valence sums are closer to their ideal value of 2 now that the contribution of K and Na to the average bond lengths of the Sr3-site have been taken into consideration. This is especially evident for experiment 729, 730, and 699 in which the contribution of K and Na, increases the BVS with almost 25% for exp. 729 and 699, and 12.5% for 730.

Both the correlation between the CSS and RSS, and how the theoretical occupancy affects the BVS, indicates that it is likely that K and Na are in fact a part of the site-population of the *Sr3*-site. However, it is important to keep in mind that this results rest on a "trial-and-error" way of assigning occupancy, and that the most preferable way of testing this, would be based on precise chemical data. Due to the poor precision of the chemical measurements (Tables 6.2 and 6.6), it is difficult to confidently compare the structural data with the chemical data. The best procedure would be to use the chemical data directly as a means to calculate a CSS-factor and see how it compares to the RSS-factor. However, it is interesting to note that the K-content presented in Tables 6.2 and 6.6, do somewhat match the *apfu* found through the calculated occupancies. In addition to this, they are also comparable to the chemical data of Pauly and Nielsen (1992), in which the K-content varies between 0.09 to 0.89 *apfu* (see Table 7.7).

7.3.7 *F*-sites

When comparing the anion-sites to that of the already published data (Hawthorne, 1983; Hawthorne and Burns 1997), it became evident that the most noticeable difference is that of the O1-site. In both jørgensenite and jarlite, the *O1*-sites were 3-coordinated, bonded to the *Na1*-, *Na2/Mg*- and the *Sr3*-site. During the refinement of the crystal structure of jørgensenite and jarlite, it became evident that this site was in fact a *F*-site. The original *O1*-site was opened by assigning it a free variable factor, which subsequently resulted in an RSS-factor of 8.88*e*. This meant that the *O1*-site contained an electron count closer to F (9*e*) than to O (8*e*). Following this result, a free variable factor was in turn assigned to each *F*-site. No distinct *O1*-site was found during the refinement. The Final R1 increased when the *F*-sites were refined as fully occupied *O*-sites, meaning that a distinct *O*-site was not supported by the refinement.

The differences in the atomic displacement parameters (Ueq) were used as indicators, as to which *F*-sites to test for dual occupancy with O. The *F*-site with the most noticeable F-O substitution proved to be the *F9*-site, with some minor substitution at the *F3*- and *F8*-sites (see Fig. 7.7, for the new O location). The new "site" is also supported by the fact that the oxygen found in the jarlite and jørgensenite structures are OH^- or H_2O molecules, which have been proven by microbeam infrared spectroscopy (Pauly et al. 1997). It is doubtful that either OH^- or H_2O would have had the available space required to reside at the original *O1*-site of Hawthorne (1983). As can be seen in Fig. 7.7, the new position is located within the largest

void of the structure of jørgensenite and jarlite, which could support the necessary space for the substitution of F with OH^- and/or H_2O.

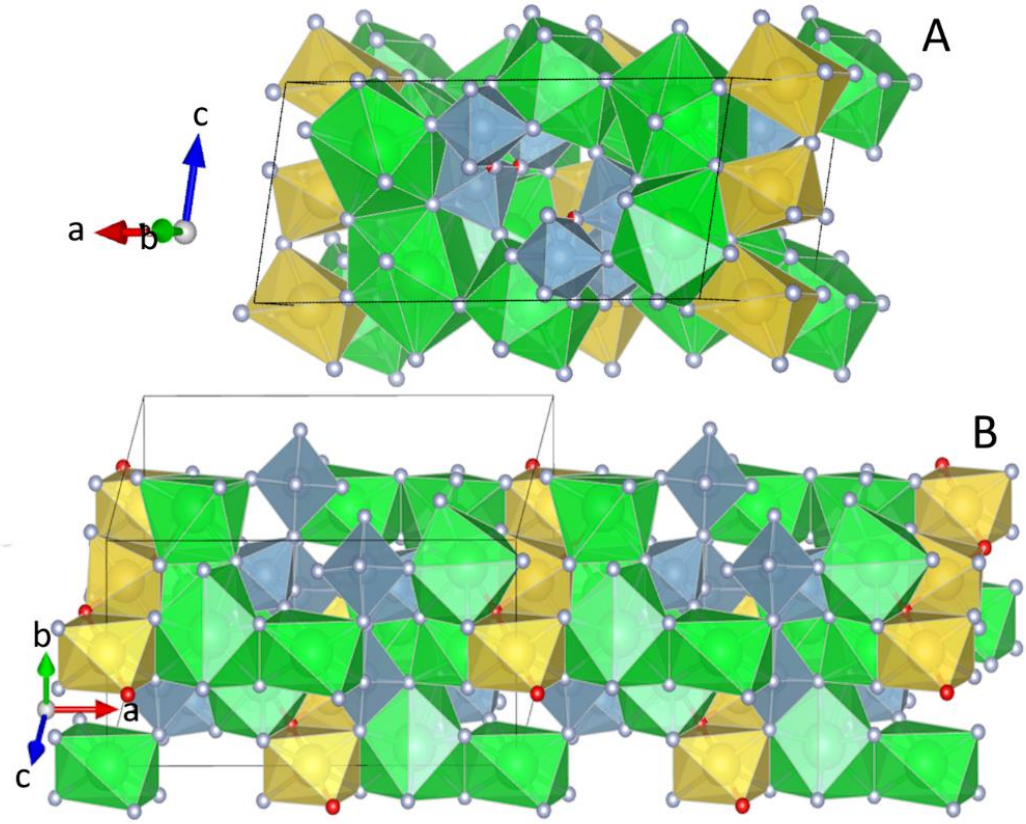

Figure 7.7: The new and the old location of O (red atom) in the crystal structure of jørgensenite and jarlite. Fig. A presents the new site where dual occupancy between O and F is found at the *F9*-site, which form bonds to the *Al1*- and *Al2*-sites. Fig. B presents the old position of Hawthorne (1984)

If OH^- and/or H_2O is substituting for F in the crystal structure of jarlite and jørgensenite, there should be a *F*-site located near the *F9*-site which could act as an acceptor for the directional hydrogen bonds created by the OH^- or H_2O-molecule (Pauling, 1960). The distance between the H-atom and the O-atom in OH^- is around 1 Å, and the hydrogen bond which would form between the H-atom and a proposed F-atom should be around 1.5 Å (Atkins et al. 2018). As can be seen in Fig. 7.8, there are only two suitable *F*-site candidates. The figure also presents two proposed placements for the H-atom, and it is important to stress that these are purely theoretical, and their placement is not related to any structural data. Potential H-atoms could be found among the x-ray residuals at the end of the crystal structure refinement, but these were not utilized due to the weakness of their signals and their subsequent erroneous behaviour

(ShelXL placed them within the O-atom). The placement of these theoretical H-atoms was conducted on the basis that the bond length between O and H should be close to 1 Å and that the hydrogen bond to the nearest *F*-site acting as acceptor, should be directional.

Figure 7.8A presents two likely candidates as receptors for hydrogen bonding. The first candidate is the *F7*-site which would be located 1.54 Å away from the theoretical *H*-site. This distance is identical to the ideal distance for a hydrogen bond between H and F and it could therefore be the most likely candidate. However, as can be seen in the more complete unit cell presented in Figure 7.8B, the H-atom would then be located along one of the edges of the *Al2*-octahedron. It is unlikely that this would be a stable placement of the H-atom, due to the repulsive forces acting upon it from the *Al2*-site.

The second candidate is the mirrored *F9*-site, at a distance of 2.3 Å from the theoretical *H*-site. This distance is quite large for a proposed H-bond, but this can explain why there is a 50% occupancy of O at the *F9*-site. The distribution of O in the *F*9-site could be governed by a glide line along the *b*-axis, which would leave every other *F9*-site occupied F and susceptible to H-bonds (Fig. 7.8C). This would still mean that the hydrogen bond between OH^-/H_2O- occupied F9-site and the F-occupied F9-site is fairly long, but a similar length of hydrogen bonds is present in the Ca-aluminofluoride, carlhintzeite (Kampf, 2010), and the Mg-aluminoflouride, leonardsenite (Weil and Werne, 2001; Mitolo et al. 2013).

The situation could also be that within each unit cell, one pair of mirrored *F9*-sites are occupied by F and the other pair by O. This model would better explain the length of the hydrogen bond, as the ideal O-H—O bond is around 1.8 Å (Atkins et al. 2018). Such a situation is found in the more complex aluminoflourides, chukhrovite (Vignola et al., 2012) and creedite (Guiseppetti and Tadini, 1983), with both of them having O-H—O bond lengths of around 2 Å. However, it is unclear if such an ordering may lead to a change in symmetry of jarlite-structures.

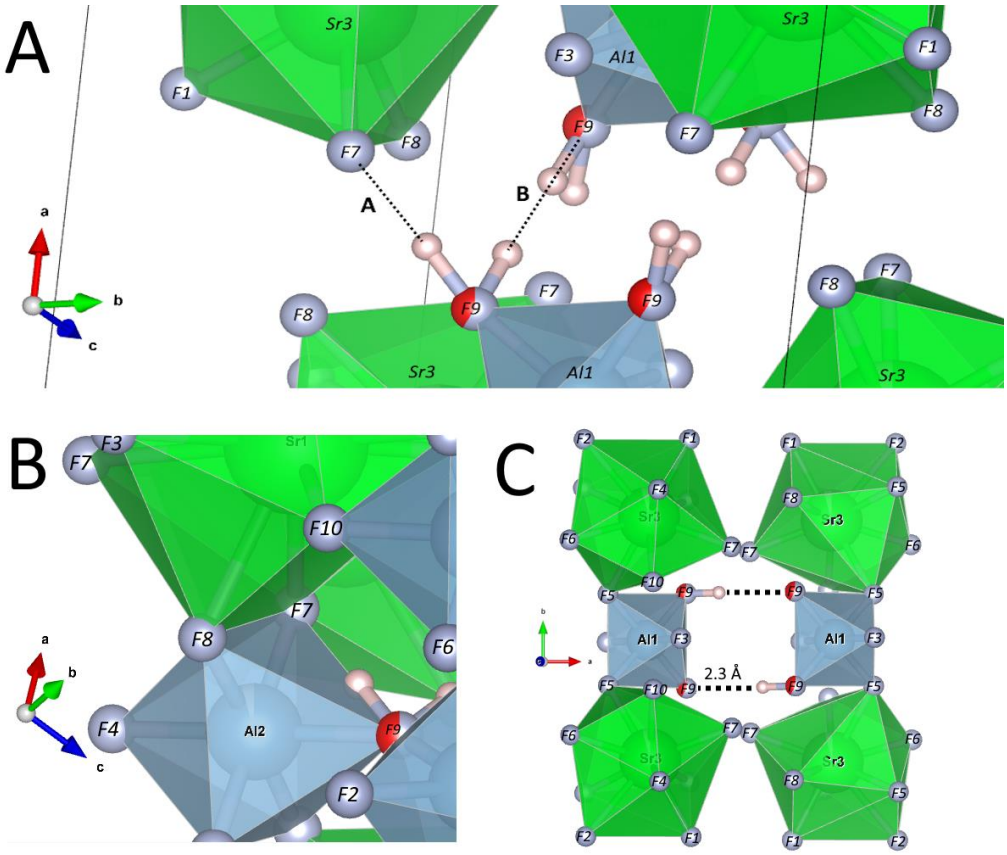

Figure 7.8: A presents the two possible H-bonds to the two nearest, opposite H-atoms. B shows that alternative A would place the H-atom along one of the edges of the Al-octahedron. C presents an overview of a proposed H-bond scheme, in which alternating *F9*-sites are occupied by O and forms H-bonds to the mirrored *F9*-site.

7.4 The Substitution Mechanism

In order for the dual occupancy of Na and Mg at the *Na2/Mg*-site to be valid, there must exist a coupled substitution mechanism which would sustain the charge neutrality of the structure. If the starting point is being treated as *Na*-site, then the structure will experience an increasing ionic charge if Mg substitutes for Na and turns the *Na*-site into a *Mg*-site. In addition, this coupled substitution mechanism must occur in relation to the *F*-sites which surrounds the *Mg*-site, so as to compensate for the increased or decreased charge at the *Mg*-site. Since the *O1*-site of Hawthorne (1983) has been disproven (Section 7.3.7), and no major substitution between F and O have been found at the *F1*-, *F4*- and *F8*-site, it seems unlikely that the charge neutrality is being sustained by anionic substitution. The most probable candidate to host this additional

substitution mechanism is the *Sr3*-site. The *Sr3*-occupant is bonded to two of the same *F*-sites as the *Na2/Mg*-atom (*F1* and *F8*), which is shown in Fig. 7.9. This proposal is supported by the BVS Tables (6.15, 6.16, 6.17) from which it can be seen that the valence of the *Sr3-F1*- and *Sr3-F8*-bonds, reacts to the occupancy of Mg at the *Na2*/*Mg*-site.

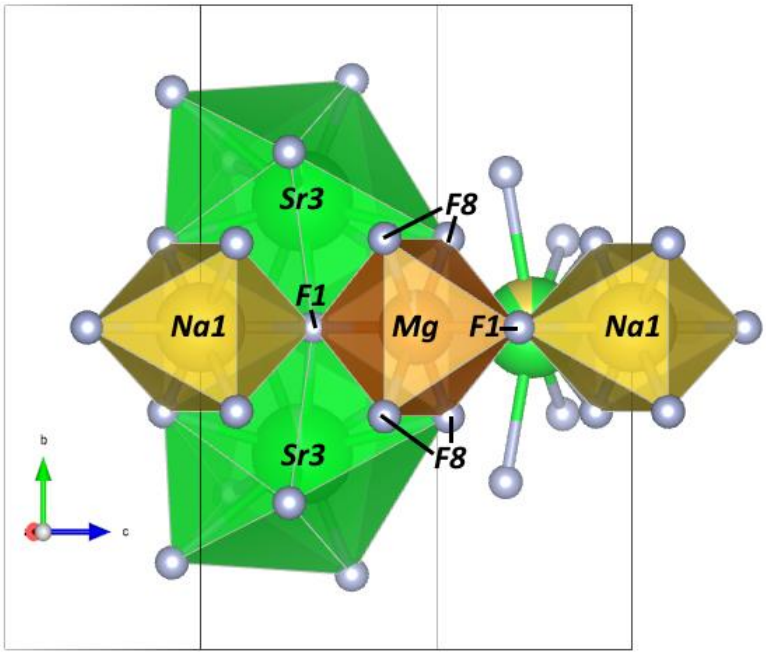

Figure 7.9: The bonding environment of the *Mg*-site in jarlite. Mg shares bonds to the *F1*-and *F8*-sites with the *Sr3*-site and the *Na*1-site. The *Sr2*-site seen in the background do not share any anions with the Mg-polyhedron.

A likely scenario is therefore that the charge neutrality of the structure is being maintained by coupled cationic substitution, occurring at both the *Mg*-site and the *Sr3*-site. In order to sustain the charge neutrality of the crystal structure, a monovalent cation must substitute for one Sr-atom, at a ratio determined by the Mg-content at the *Mg*-site. The only monovalent cations found during the EPMA-analysis were K and Na, as was presented in Section 6.2. Sodium is primarily assigned to its own site, but some excess Na have been found to occupy *Sr3*-site together with K. The proposed substitution between K, Na, Sr and Mg, would follow the formula (sites in brackets),

$$Mg^{2+}[Na2] + (K^{+} + Na^{+})_{1}\,[Sr3] \leftrightarrow\ Sr^{2+}[Sr3] + Na^{+}[Na2] \qquad (7.4)$$

This substitution mechanism would be governed by the Mg-content in the *Mg*-site, and an equal number of Na + K atoms have to be found at the *Sr3*-site for this formula to hold true. Figure

7.10 presents a plot of the excess-Na + K content (*apfu*) against the Mg-content (*apfu*) for all of the points analysed with the EPMA for jarlite. There is a clear positive correlation between the Mg-content and the K + Na – content. This trend should follow a 1:1 ratio if the proposed formula is correct. However, it seems to be somewhat deficient on the Na + K-content. There is the possibility that more monovalent cations are involved, however only K and Na were found during the analysis with the EDS and the EPMA. Another possibility is that the content of excess Na assigned to the *Sr3*-site should be higher than the estimation used. The used estimation was based on the total content of Na minus the content assigned to the *Na1* and *Mg*-site. This works for the *Mg*-site, but there could be some type of substitution at the *Na1*-site which would increase the amount of excess Na. An addition of Li to the *Na1*-site (as discussed in Section 7.3.2) would have this effect, and an increasing content of Li, would results in an increasing content of excess Na at the *Sr3*-site.

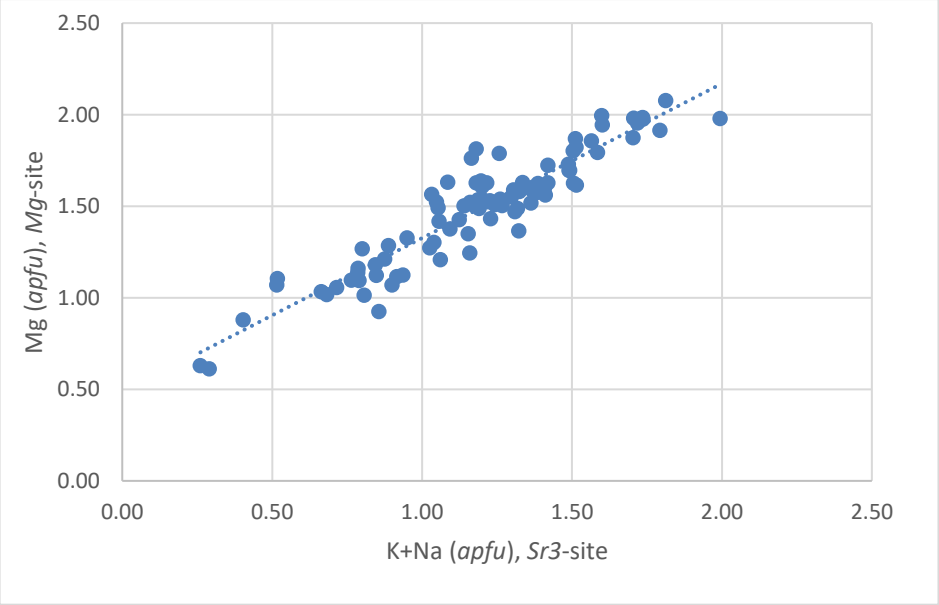

Figure 7.10. A plot of the Mg-content of the *Mg*-site in jarlite against a proposed content of excess Na + K found within the *Sr3*-site.

7.5 What is jørgensenite/jarlite?

7.5.1 Previous studies

The Ba-, Mg-, Na-content has been used throughout this thesis as a means to identify and distinguish chemically between jarlite and jørgensenite. As can be seen in Tables 6.1 and 6.5, together with Fig. 6.2, this criterion seems to work in order to achieve a chemical distinction between the two phases observed as the core-and-mantle features (Fig. 6.2 and 6.7). However, this criterion is a simplified version of the criteria presented by Hawthorne and Burns (1997) for the difference between jørgensenite and jarlite.

The complete set of criteria, as of Hawthorne and Burns (1997), are (1) that jørgensenite should contain a greater content of Na than Mg at the *Na2*-site (thus making it a *Na*-site and not a *Mg*-site) and (2) that the *Sr2*-site should be dominated by Ba. For the jørgensenite analysed by Hawthorne and Burns (1997) this seems to hold true, they found that the *Sr2*-site contained 60% Ba and that the *Na2*-site contained 75% Na. An interesting aspect of these criteria is that only one of them holds true when the structural results of Hawthorne and Burns (1997) are compared to the accompanying chemical results of Pauly et al. (1997). From the chemical data presented in Table 1 of Pauly et al. (1997) and Table 7.7 (this thesis), it is seen that the measured Ba-concentration yielded a Ba content of 1.85 *apfu*. However, they do not place the Ca, K, excess Na, Sr and Ba into their corresponding *Sr*-sites. This means that from a structural perspective, they have not verified that the second criterion of Hawthorne and Burns (1997) have been fulfilled.

There are three *Sr*-sites in the structure of jarlite and jørgensenite. The *Sr1*-site is located at the 8 corners of the unit cell and c-centred yielding a contribution of 2 Sr-atoms to the chemical formula. The *Sr*3-site have 8 positions within the unit cell, which contributes with 8 Sr to the chemical formula, and the *Sr2*-position contributes with the 4 remaining atoms. A was discussed under Section 7.3, K and excess Na are hosted within the *Sr3*-site. The *Sr1*-site is mainly occupied by Sr, but it seems likely that this site experiences some degree of dual occupancy with Ba. Finally, the *Sr2*-site is primarily occupied by Sr and Ba, with a possible minor content of Ca. A more precise empirical formula for jørgensenite, based on the chemical data of Pauly et al. (1997), would therefore be:

$Na_2(Sr_{1.8}Ba_{0.2})_2(Sr_{2.09}Ba_{1.65}Ca_{0.21})_{3.95}(Sr_{7.14}Na_{0.63}K_{0.23})_8Na_2Al_{12}F_{64}(OH,F)_4$

It is evident from the new formula, that the Ba > Sr at *Sr2*-site criterion of Hawthorne is not fulfilled, due to the dominance of Sr in the *Sr2*-site.

There are two other interesting inconsistencies between the chemical nature of jørgensenite as described by Hawthorne and Burns (1997) and the description of Pauly et al. (1997). The latter proposed an ideal end-member formula of $Na_2Sr_{14}Na_2Al_{12}F_{64}(OH,F)_4$, which is completely Ba-free. This is in stark contrast to the second criterion of Hawthorne and Burns (1997), with which the chemical formula of an ideal end-member would have been $Na_2Sr_{10}Ba_4Na_2Al_{12}(OH,F)_4$. Whether the Ba-rich end-member is still considered valid is however uncertain. A new study on the classification of aluminoflourides, Hawthorne and Hartwig (2021) seem to agree that the ideal formula should be Ba-free, in accordance with Pauly et al. (1997).

The second inconsistency originates from the introduction of Pauly et al. (1997), in which they present jørgensenite as a new mineral which had previously been described from the paper of Pauly and Nielsen (1992) as the Mg-Free core-part of the core-and-mantle feature of jarlite. However, the empirical formulas presented by Pauly and Nielsen (1992) of the analysed cores have a Ba-content in the ranges of 0.47 to 0.57 *apfu* (Table 7.7), which does not meet the second criterium of Hawthorne and Burns (1997). This also means that the chemistry of the cores does not match the chemical data presented by Pauly et al. (1997), except for one "jalite", originating from the stenonite paragenesis, which have a Ba-content of 1.87 *apfu* (Pauly and Nielsen, 1992). However, the chemical data of Pauly and Nielsen (1992) do support the idea of Pauly et al. (1997), that the ideal end-member could be $Na_2Sr_{14}Na_2Al_{12}F_{64}(OH,F)_4$. This would however mean that the second criterion of Hawthorne and Burns (1997), Ba > Sr at the *Sr2*-site, would be an unnecessary criterion in order to chemically define jørgensenite, as the new classification also seem to agree with (Hawthorne and Hartwig, 2021).

Table 7.7: Chemical data (*apfu*) from the literature

	Core[1]	Mantle[1]	Core[1]	Mantle[1]	Core[1]	Mantle[1]	Jørgensenite[2]
OH	-	-	-	-	-	-	2
F	68	68	68	68	68	68	66
Na	3.87	3.19	3.72	3.77	3.43	3.16	4.17
Mg	0.07	1.60	0.31	1.61	0.02	1.90	0.46
Sr	13.55	12.25	13.72	12.13	13.73	11.84	11.03
Al	11.83	11.74	11.59	11.73	11.91	11.75	12.00
K	0.15	0.89	0.24	0.60	0.09	0.77	0.23
Ca	0.10	0.36	0.13	0.29	0.09	0.47	0.21
Ba	0.57	0.17	0.47	0.20	0.53	0.18	1.85

1: From Pauly and Nielsen (1992)
2: From Pauly et al. (1997)

7.5.2 This Study

7.5.2.1 Low-Ba jørgensenite

The majority of jørgensenite analysed with the EPMA show a similar chemistry as the cores of Pauly and Nielsen (1992). The Ba-content is systematically below the 1.85 *apfu* of Pauly et al. (1997) and are in the ranges between 0.51 and 0.83 *apfu*. The Mg-content is below detection limit (<0.001) and the Na-content is in the range of 3.39 to 3.59 *apfu*. In relation to the criteria of Hawthorne and Burns (1997), these results fulfil the first criterion, but not the second.

The jørgensenite found in paragenesis with stenonite have a higher Ba-content of 1.73 *apfu*, which is also similar to the one described by Pauly and Nielsen (1992). However, it also has a Mg-content of 1.16 *apfu*, which would mean that the *Na2*-site is dominated by Mg. Consequently, the jørgensenite with the highest content of Ba found, fails to fulfil both criteria that define jørgensenite (Hawthorne and Burns, 1997). The elevated Mg-content of this particular jørgensenite could be related to the small internal zones of jarlite found throughout jørgensenite of sample PAD-IG007 (as shown in Fig. 6.7), and it is possible that such a domain has contributed during the analysis.

7.5.2.2 High-Ba Jørgensenite

As presented in Section 6.2.2 certain jørgensenite crystals were found to have Ba-rich terminations. Due to the size of these areas, few could be analysed with the EPMA due to the high beam size. As presented in Table 6.3, three Ba-rich jørgensenites were found during the EPMA-analysis and analysed successfully. These three samples all have a Ba-content above 3.0 *apfu*, which means that the *Sr*2-site is dominated by Ba. Simultaneously, they have a Na-content exceeding the Mg-content at the *Na2*-site. This means that they fulfil the criteria of Hawthorne and Burns (1997), and that these criteria could be correct.

This is further supported by the structural data found from analysis and refinement of experiment 804. With an RSS-factor of 53.334*e* for the *Sr2*-site, this jørgensenite truly has a *Sr2*-site dominated by Ba. The RSS-factor gives a Ba-concentration of 85% which result in a Ba-content of 3.4 *apfu*. This correlates with the EPMA-data recorded from the Ba-rich terminations, and it indicates that the crystal analysed as exp. 804 could be of similar chemistry.

The high amount of Ba found both by SXRD and EPMA would also suggest that in these instances, the *Sr2*-site should be more properly named a *Ba*-site.

7.5.2.3 New classification

The results discussed in Sections 7.5.2.1 and 7.5.2.2 provide some clarification as to what should be considered a jørgensenite. Since the majority of the EPMA-data provide strong evidence for the existence of a Ba-poor jørgensenite, it seems in order to verify the original suggestion of Pauly et al. (1997) and the later clarification of Hartwig and Hawthorne (2021). The ideal formula of jørgensenite should be recognized as $Na_2Sr_{14}Na_2Al_{12}F_{64}(OH, F)_4$, with no additional requirements for the Ba-content. The difference between jørgensenite and jarlite is therefore their respective content of Mg at the *Na2/Mg*-site, where Na > Mg defines a jørgensenite and Na < Mg defines a jarlite. The revised site-assignment of the crystal structure of jarlite and jørgensenite also makes it possible to propose a more detailed general formula for these minerals,

$$(Na, Li)_2\ (Sr, Ba)_2\ (Sr, Ba, Ca)_4\ (Sr_{8-y}\ (K_a\ Na_b)_{a+b=y})_8\ (Na_x, Mg_y)_{x+y=2}\ Al_{12}F_{64}(OH, F)_4$$

where the ordering of cation sites are as follows; *Na1*, *Sr1*, *Sr2*, *Sr3*, *Na2*, *Al1+Al2*. In this general formula, x > y defines a jørgensenite, and x < y a jarlite.

When it comes to the existence of a Ba-dominant jørgensenite, as first suggested by Hawthorne and Burns (1997), it is evident from exp. 804 that such a mineral exists, and it is therefore proposed that it should be recognized as its own mineral. Furthermore, from the EPMA-data presented in Section 6.2.2, there also seem to exist a Ba-dominated jørgensenite with a Mg-content that resemble an intermediary phase between jarlite and jørgensenite. This indicate that both jarlite and jørgensenite may have corresponding Ba-dominant endmembers.

It is therefore possible that jørgensenite and jarlite may be a part of a larger group of isostructural Sr-aluminoflourides, with theoretical endmembers defined by Ba or Sr dominance at the *Sr2*-site and Mg or Na dominance at the *Na2/Mg*-site. Additionally, since caljarlite have been presented as the Ca-analogue of jarlite, there may exist additional members, defined by a Ca-dominant *Sr2*-site and Mg or Na dominance at the *Na2/Mg*-site. The members of this theoretical group are presented in Table 7.9.

When it comes to naming the new mineral species, it is proposed that it should wait until further insight into this proposed mineral-group have been achieved. Furthermore, a detailed

description of this new mineral should be accompanied by a detailed description of its paragenesis. The paragenesis from which exp. 804 was collected from is different from the all the others, and the Ba-analogue of jørgensenite were found together with bøggildite ($Na_2Sr_2Al_2PO_4F_9$). The crystal structure should have been sufficiently described in the previous sections in order to confidently approve of its chemical and structural relationship to jørgensenite. However, this paragenesis still remains to be researched.

Table 7.9: Ideal chemically formula of the proposed group members

Jørgensenite	$Na_2Sr_{14}Na_2Al_{12}F_{64}(OH, F)_4$
Ba-analogue	$Na_2Sr_{10}Ba_4Na_2Al_{12}F_{64}(OH, F)_4$
Jarlite[1]	$Na_2Sr_{14}Mg_2Al_{12}F_{64}(OH, H_2O)_4$
Jarlite[2]	$Na_2Sr_6(Sr_6(Na,K)_2)_8Mg_2Al_{12}F_{64}(OH, H_2O)_4$
Theoretical	$Na_2Sr_{10}Ba_4Mg_2Al_{12}F_{64}(OH, H_2O)_4$
Calcjarlite?	$Na_2Sr_{10}Ca_4Mg_2Al_{12}F_{64}(OH, H_2O)$
Theoretical	$Na_2Sr_{10}Ca_4Na_2Al_{12}F_{64}(OH, H_2O)$

1: Ideal formula based on fully occupied *Sr*-sites, meaning that it is not charge balanced
2: Ideal formula based on the suggested substitution mechanism of Section 7.4

7.6 Petrology

7.6.1 Prismatic Bodies

Pauly (1993) described an occurrence of jarlite as pseudomorphs after prismatic precursors, which he found to be cleavage fragments of cryolite. As was presented in Section 6.1, similar pseudomorphs have been found during the work on this thesis, but also some that are quite different. The pseudomorphs found in sample PAD-IG006 (Fig. 6.4) show a more distinct crystal habitus than the prismatic bodies of Pauly (1993), but both are rimmed by same type of cryptocrystalline topaz. Pauly (1993) was able to use the angles between the cryptocrystalline topaz-coverings to determine the crystallographic faces of the replaced crystal. Even though the faces are among the most commonly found for minerals with a “box”-like habitus, Pauly (1993) correlated these findings with the cleavage-faces of cryolite ({001} and {110}). If the prismatic bodies were to be the remnants of cleavage fragments of cryolite, one would expect that the observed habitus not only corresponded to the cleavage faces, but also corresponded to the

crystal system of cryolite. The highly elongated shape of some of these prismatic bodies, together with the crystal faces, do not correspond well with a monoclinic symmetry. Figure 7.11 presents several of these prismatic bodies, from which two potential 2-fold rotation axes can be inferred to be present.

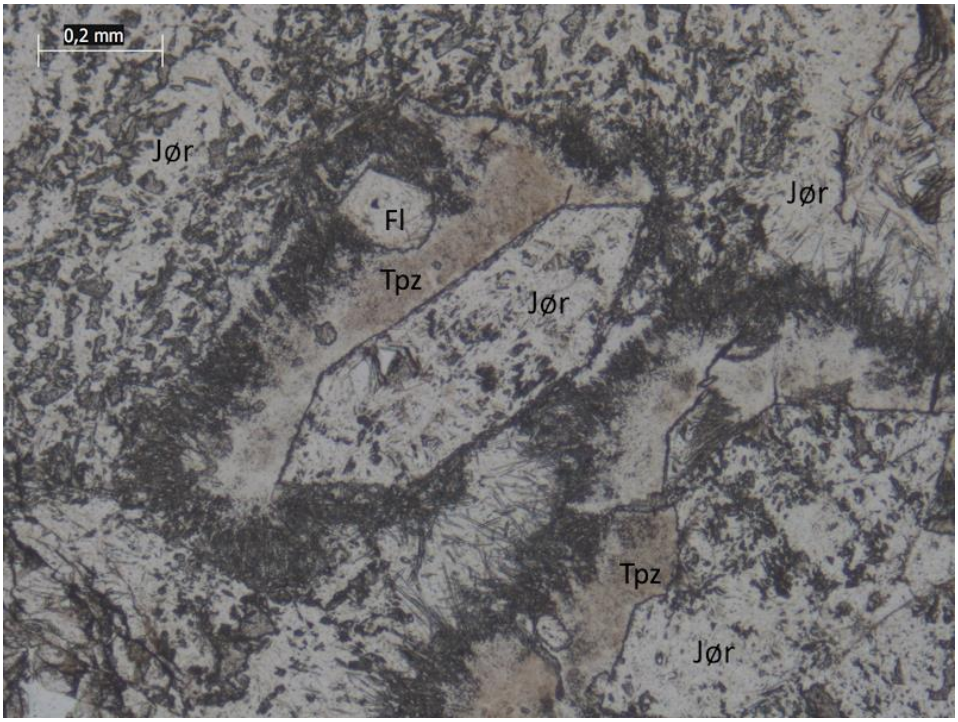

Figure 7.11. A closer view of the "prismatic body", or jørgensenite (Jør) pseudomorph after celestine or baryte, as proposed and discussed in the text, from sample PAD-IG005, first presented in Fig. 6.4. Notice the thin crystals of topaz (Tpz), which can be seen radiating from the dark band below the pseudomorph.

Figure 6.11 presented an XPL-image of euhedral crystals of celestine/baryte found in sample PAD-IG001. The habitus of these crystals seems to be identical to the outline of the pseudomorphs found in PAD-IG006, which suggests that these pseudomorphs could have formed after baryte and/or celestine. This proposal is further strengthened by the presence of the anhedral and corroded grains of baryte found within the crystal. These baryte grains seem to have a uniform extinction in XPL, indicating that they are identically orientated, which means that these originally crystallized as part of one crystal. The proposed pseudomorphic replacement after baryte also satisfy the measured crystal faces of Pauly (1993), and all of the faces identified by him can also be found in baryte crystals or cleavage fragments (Seager and Davidson, 1952; Imreh and Mârza, 1978).

The presence of bøgvadite also supports this notion. Balić-Žunić (2014) and Pauly and Petersen (1988), both argued that bøgvadite and jarlite/jørgensenite seem to have co-crystallized, meaning that the fluid from which these grew must have been enriched in Sr and Ba. The breakdown of baryte and celestine would indeed produce a Sr- and Ba-rich environment, favourable for the co-crystallization of jørgensenite, jarlite and bøgvadite.

7.6.2 Dissolution of Baryte and Celestine

The replacement of celestine and baryte into jørgensenite, jarlite and bøgvadite, could be attributed to a change in the redox conditions of the system. Baryte is usually found as a product of oxidation of sulfides, and the dissolution of baryte would therefore be attributed to the introduction of a reducing fluid (Hanor, 2000). Since jarlite and jørgensenite have a high content of Sr, it is more likely that they occur as pseudomorphs after celestine than baryte. Celestine is more soluble than baryte under reduced conditions (Hanor, 2000). This would also explain why jørgensenite and jarlite are more common than bøgvadite, and also why celestine is a somewhat uncommon mineral to find. The fact that celestine/strontian baryte was found in in sample PAD-IG001, suggests that dissolution was localized.

The proposed hypothesis is supported by the observed texture of the baryte found in paragenesis with jørgensenite, jarlite and bøgvadite. The baryte grains were observed to be highly anhedral, irregular and slightly rounded, which attest to a somewhat corroded texture. In addition, baryte was found in close vicinity to euhedral crystals of pyrite, which is in stark contrast to the occurrence of galena, of which the latter was found as miniscule, irregular and anhedral grains.

This is in contrast to the proposed crystallization sequence of Pauly and Petersen (1988), of which they argue that baryte formed as a product of corrosion of bøgvadite. However, no textural evidence has been found to attest to the breakdown of bøgvadite in favour of baryte and it seems more likely that bøgvadite formed as a product of the replacement of baryte and/or celestine.

Pauly and Bailey (1999) argued that the second stage mineralization of fluorite, topaz and Sr-aluminoflourides was accompanied by several pneumatic explosions. If pyrite were to be native to the earlier stages, it seems unlikely that the heterogeneously distributed euhedral crystals would remain undamaged during an explosive event which caused widespread fracturing throughout the deposit. It seems more likely that the pyrite crystallized from the same source

as jørgensenite, jarlite and bøgvadite, which would mean that sulphur must have been remobilized prior.

The remobilization of sulphur can therefore be attributed to the dissociation of baryte. Baryte would have become unstable due to the introduction of a reducing, H^+-rich fluid, which would have reduced S^{6+} in sulphate, to S^- in the persulfide of pyrite. The dissociated Ba^{2+} would quickly have been incorporated into the Ba-bearing phases, jørgensenite, jarlite and bøgvadite. Such a fluid would also have been acidic, with the pH necessary in order to dissociate siderite (Harper and Row, 1965), which would have been necessary in order to remobilize Fe. Siderite is commonly found throughout certain parts of the cryolite deposit but have been absent in the samples investigated during the work on this thesis. The dissociation of siderite would provide the iron, necessary for the crystallization of pyrite, a process which have been reported from Ivigtut (Pauly, 1962). The complete replacement process of baryte and siderite, can therefore be written as,

$$2\ BaSO_4\,(s) + 4H^+\,(aq) + FeCO_3\,(s)$$

$$\rightarrow 2Ba^{2+}\,(aq) + FeS_2\,(s) + 7/2\ O_2\,(l \text{ or } g) + 2\ H_2O\,(l \text{ or } g) + CO_2\,(l \text{ or } g) \qquad (7.5)$$

, where baryte is redox-sensitive and siderite is pH-sensitive. It is important to state that this hypothesis is purely a suggestion, and that further research is necessary. The high number of variables (H^+, O_2, H_2O, CO_2) also makes it difficult to evaluate this proposal with the use of phase diagrams.

The dissociation of siderite due to acidic conditions may be transferable to stenonite. Potential evidence for the breakdown of stenonite was presented in Fig 6.5, where it seems likely that jørgensenite may have formed after stenonite. However, Fig. 6.6 presents an XPL-image of stenonite, from which it can be seen that stenonite occur as a rim, partially surrounding pyrite. The sharp boundaries between jørgensenite and stenonite indicate that stenonite is unaffected by the presence of jørgensenite. Additionally, Pauly (1962) reported that stenonite had been found as products of alteration of siderite. This is in contrast to the relationship found in Fig. 6.5 and could indicate that there exist several generations of stenonite.

7.6.3 Primary Ba- phases

The evidence provided for the breakdown of baryte and celestine as a direct cause for the crystallization of jørgensenite and jarlite, is in contrast to the proposed crystallization sequence of Pauly and Petersen (1988), Pauly (1993) and Balić-Žunić (2014). Additional discussion of this crystallization sequence will be presented in Section 7.6.4.

However, it seems unlikely that baryte and celestine are the primary Sr and Ba phases of the deposit, in accordance with the reasoning of (Pauly and Petersen, 1988; Balić-Žunić, 2014; Hutchinson et al. 2019). As mentioned in the beginning of this section, both baryte and celestine form under oxidizing conditions (Hannon, 2000). Due the high amount of F^- which would have been present during the first stage of the formation of the cryolite deposit, the conditions would have been slightly reducing (Köhler et al. 2007, Hutchinson et al. 2019). This means that there is the possibility that baryte and celestine represent secondary Ba and Sr phases of the deposit and that the primary phases still remain to be discovered.

Even though the Ivigtut cryolite deposit is quite unique from a geological perspective, there do exists similar systems, as presented in Section 2.1. The Katugin rare metal deposit in East Siberia, Russia, is found in relation to an A-type granitic complex, which also host lenses and veins of cryolite (Gladkochub et al. 2017). The mineralogy of these cryolite lenses is similar to that of Ivigtut and several of the aluminofluorides first described from Ivigtut can also be found at Katugin (Pauly and Bailey, 1999; Starikovaa et al., 2017). What makes the comparison between Katugin and Ivigtut interesting, is that several different Ba-aluminofluorides have been discovered at Katugin, and that these minerals have been proposed to represent some of the earliest phases formed. These minerals include usovite $Ba_2CaMgAl_2F_{14}$ and three potentially new minerals with the chemical formula $BaAlF_6(OH)$, $BaCa_2AlF_9$ and $BaCa_4AlF_{13}$, which has not been fully described yet (Starikovaa et al., 2017). All of these minerals have been suggested to have been formed as primary Ba-phases, mainly based on the logical conclusion that Ba-aluminoflourides should have a larger stability field than Ca- and Na- aluminoflourides (Starikovaa et al., 2017).

None of these minerals have so far been reported from Ivigtut, but it is a possibility that such phases could have formed during the early stage of the formation of the cryolite deposit at Ivigtut, similar to what has been found for Katugin.

7.6.4 Formation of jørgensenite and jarlite

7.6.4.1 Crystallization Sequence

The proposal that jørgensenite and jarlite formed due to the dissolution of celestine holds implications for the inferred crystallization sequence. It is evident that the cryptocrystalline topaz and fluorite must have crystallized at a stage when celestine still existed. Pauly (1993) attested the topaz rims found around the prismatic bodies, to have been formed by an explosive event. The cryptocrystalline nature, and the flow-like, dendritic appearance of these bands, are in support of this notion (Fig 6.4). The two events, the introduction of topaz and the dissociation of celestine and baryte are probably linked, as the explosive event would undoubtedly have caused widespread fracturing (Pauly and Bailey, 1999). These fractures and veins probably acted as transport ways for H^+ bearing fluids which caused the dissociation of celestine at the same time as the explosion deposited large amounts of topaz and fluorite. The second generation of topaz found as tiny radiating needles began crystallizing shortly after celestine dissociated, and further growth was probably inhibited by a quick change in conditions, favouring the crystallization of jørgensenite followed by jarlite.

The crystallization of bøgvadite followed soon after and was probably caused by the dissociation sequence of (1) celestine, (2) baryte, meaning that the Ba-content of the fluid increased during the final stages of dissociation. This is supported by the EPMA-data of bøgvadite, Tables 6.8 and 6.9. The amount of Ba detected in bøgvadite exceed that which could solely be placed in the *Ba*-site in its crystal structure, and it seems likely that surplus Ba substitutes for Sr at the *Sr*-site. This result attest to the overall Ba-enriched state of the fluid from which bøgvadite formed and support that jørgensenite and jarlite had already crystallized when the fluid started to corrode baryte. The anhedral character of bøgvadite is also in support of this proposal, and euhedral growth was inhibited by the already crystallized jørgensenite and jarlite.

This proposal slightly alters the proposed crystallization sequence of Pauly and Petersen (1988) and Balić-Žunić (2014), who reported bøgvadite as having co-crystallized with jarlite and/or jørgensenite. However, Pauly and Petersen (1988) and Balić-Žunić (2014) reported finding euhedral crystals of bøgvadite, which has not been found during the work on this thesis.

Lastly, residual fluids rich in Ca and Mg accumulated within pockets of jørgensenite and jarlite, from which pachnolite/thomsenolite and/or hydrokenoralstonite crystallized. This is in

agreement with the hypothesis of Pauly and Bailey (1999) and supported by the petrological evidence presented in Appendix I. Almost all of the cavities in which jørgensenite and jarlite crystallized is filled by pachnolite/thomsenolite and/or hydrokenoralstonite, and these minerals are also found to occur in veins which transects intergrowths of fan-shaped aggregates of jarlite.

7.6.4.2 Solid solution between jarlite and jørgensenite?

Pauly and Nielsen (1992) first suggested that there may be a solid solution series between the core-and-mantle features which they observed during their studies. This hypothesis was further elaborated upon by Pauly et al. (1997) and they suggested that there should at least be a partial solid solutions series between the two minerals, based on the amount of Mg found in the *Na2*-site of the type jørgensenite (0.46 *apfu*).

As can be seen from the Mg-concentration measured from jørgensenite (Table 6.2) and the complete set of measurements (Appendix III), the majority of jørgensenites are almost completely Mg-free. This is in contrast to the hypothesis of Pauly et al. (1997), and suggests that jørgensenite is on average, free of Mg.

However, there is the possibility that these results more closely reflect the chemical environment from which jørgensenite formed, than they provide evidence towards or against a solid solution series. In section 7.4, it was presented that the Na- and Mg-content in the *Mg*-site of jarlite, is governed by the complex cationic substitution presented in Formula 7.4. Such a substitution mechanism would be controlled by the overall concentration of Sr in the fluid from which these minerals crystallized.

Accordingly, a solid solution series between jarlite and jørgensenite would be governed by the amount of Sr found in the fluid from which these minerals crystallized. Since these minerals are proposed to have formed from the dissociation of celestine and/or strontian baryte, jørgensenite crystallized first due the great amount of Sr that was released. In such a scenario the Sr to monovalent cation ratio is too high, for it to be energetically favourable for the crystal structure to incorporate larger amounts of K and Na at the *Sr3*-site. This hypothesis is supported by the results presented in Fig. 6.2 and 6.7 where it can be seen that jarlite occur as a mantle surrounding a jørgensenite core, and it is also supported by the chemical measurements of Pauly and Nielsen (1992). This relationship seems to represent a change in the chemical composition of the fluid from which these minerals grew, into one where the number of monovalent cations

had increased, and the Sr content decreased. As mentioned in Section 7.6.4.1, bøgvadite found in this paragenesis seem to be enriched in terms of Ba, which supports a reduced concentration of Sr, which would be favourable for the crystallization of jarlite.

Additionally, the refined crystal structures indicate that the *Na2*-site in jørgensenite may contain smaller amounts of Mg (Table 7.3). These findings do support a solid solution series between jarlite and jørgensenite, as suggested by Pauly and Nielsen (1992) and Pauly et al (1997). This is further supported by the range in polyhedron volume found for the *Na2*-site in jørgensenite (Fig 6.13), and this range can be interpreted to represent a change from a Mg-dominated site, towards a Na-dominated site.

7.7 $^{87}Sr/^{86}Sr$ – signature

Since there is no evidence from petrography that jørgensenite and jarlite have undergone any form of recrystallization which could affect the initial $^{87}Sr/^{86}Sr$-ratio, it is likely that the recorded $^{87}Sr/^{86}Sr$-ratios can also be treated as initial ratios. This is however somewhat uncertain for stenonite, and there is a possibility that stenonite occur in several generations. Additionally, these minerals only contain minor trace amounts of Rb, which means that the content of ^{87}Sr is the same as when they first crystallized. From the four samples which were analysed, it can be seen than jørgensenite/jarlite and stenonite can be divided into two separate groups based on their $^{87}Sr/^{86}Sr$-ratios. The jarlite/jørgensenite have $^{87}Sr/^{86}Sr$ ratio of 0.708926, while stenonite have the somewhat higher ratio of 0.709718. These values resemble those of the cryolite ore (0.70977, 0.70877) and fluorite ore (0.7096), analysed by Blaxland (1976), and are significantly higher than the initial Sr-ratios of the Gardar intrusions.

Blaxland (1976) did not describe the paragenesis from which the cryolite ore and fluorite ore were extracted. According to the multi-stage model of Pauly and Bailey (1999), cryolite crystallized during both the first and the second stage of the deposit, whereas fluorite primarily crystallized during the second stage. Whether the cryolite analysed by Blaxland (1976) originate from the first or the second, holds implications as to how this similarity in $^{87}Sr/^{86}Sr$-ratio between jørgensenite/jarlite, stenonite and cryolite should be interpreted. It seems likely that the meaning of the description “cryolite ore”, is meant to resemble the pure cryolite formed during the first stage, and which acted as the main ore-deposit during the years of mining, which will be assumed in the following discussion.

As was described in Section 3.4.4, most of the Gardar magmas have initial $^{87}Sr/^{86}Sr$ ratios which indicate SCLM-type magma source (Upton et al., 2003; Köhler et al., 2009; Upton, 2013; Bartels et al., 2015; Hutchinson et al., 2021). However, the origin of the cryolite-deposit is still somewhat disputed. The magma source of the Ivigtut granite is believed to be mantle derived with some contribution from the assimilation of a crustal component (Blaxland, 1976; Pauly and Bailey, 1999). This theory relies on unpublished data mentioned by Pauly and Bailey (1999), from which they found an initial $^{87}Sr/^{86}Sr$ ratio of 0.705 for the "fresh granite". Their suggestion is in agreement with the range of initial $^{87}Sr/^{86}Sr$-ratios (0.705-0.710) suggested by Blaxland (1976), who also explained the $^{87}Sr/^{86}Sr$-ratio of cryolite as a product of the interaction between the granitic wall-rocks and an influx of ^{87}Sr-enriched fluids. This notion is also somewhat supported by Pauly and Bailey (1999), although their theory rests more on the proposed influence of immiscibility of melt fractions and post-magmatic fluids. Since the dataset for the "fresh granite" of Pauly and Bailey (1999) was never published, it is difficult to assess the quality and reproducibility of their results. Goodenough (1997) and Goodenough et al. (2000) recorded a range of $^{87}Sr/^{86}Sr$-ratios, but none of them provided any meaningful insight into the origin of the granitic wall-rocks, due to the high degree of ^{87}Sr-contamination (see Table 6.10).

There is however some debate surrounding the hypothesis of Pauly and Bailey (1999). Goodenough et al. (2000), Köhler et al. (2007) and Hutchinson et al. (2019) all agree upon that the main source of the cryolite deposit should be a reduced F^- and CO_3^{2-} , mantle-derived alkaline fluid, and that this fluid has undergone some form of mixing. Goodenough et al. (2000), proposed mixing with granitic country rocks, while Köhler et al. (2007) and Hutchinson et al. (2019) proposed mixing with a brine, derived from a meteoric fluid source. Their arguments rest on a wide variety of data.

- Goodenough et al. (2000) used the Sm-Nd-system together with REE-systematics to propose a mantle derived origin for the Ivigtut granite, with some assimilation of a crustal component. The high initial ε_{Nd} of the metasomatically altered granites was inferred to indicate metasomatism caused by a mantle-derived fluid.
- The fluid inclusions study of Köhler et al. (2007) found that the $\delta^{13}C$ of CO_2 resemble that of the mantle-derived carbon while $\delta^{18}O$ resemble an isotope exchange with a meteoric fluid source.

- Hutchinson et al. (2019) found that varying $\delta^{34}S$-signature of barytes and sulfides from the cryolite deposit could be explained by the hypothesis of Köhler et al. (2007).

These hypotheses are all in contrast to the mixing hypothesis of Pauly and Bailey (1999), in which they proposed that the cryolite deposit crystallized from a mixture of a granitic melt-fraction, post magmatic volatiles and leached material from the surrounding wall-rocks.

Figure 7.12 presents a plot of the initial $^{87}Sr/^{86}Sr$-ratios of several of the Gardar rocks of similar age to the proposed age of Ivigtut, versus time. Representative initial $^{87}Sr/^{86}Sr$-ratios of rocks of the Ketilidian and Archaen basement have also been provided, in addition to their respective evolution in $^{87}Sr/^{86}Sr$-ratio over time. The evolution in $^{87}Sr/^{86}Sr$-ratio of the depleted mantle have been modelled after Othman et al. (1984), and the "high" Rb-crust after Faure and Mensing (2005). The $^{87}Sr/^{86}Sr$-ratio of jørgensenite and stenonite are highlighted by the shaded area. This area also represents the "evolution" of $^{87}Sr/^{86}Sr$-ratio for jørgensenite and stenonite.

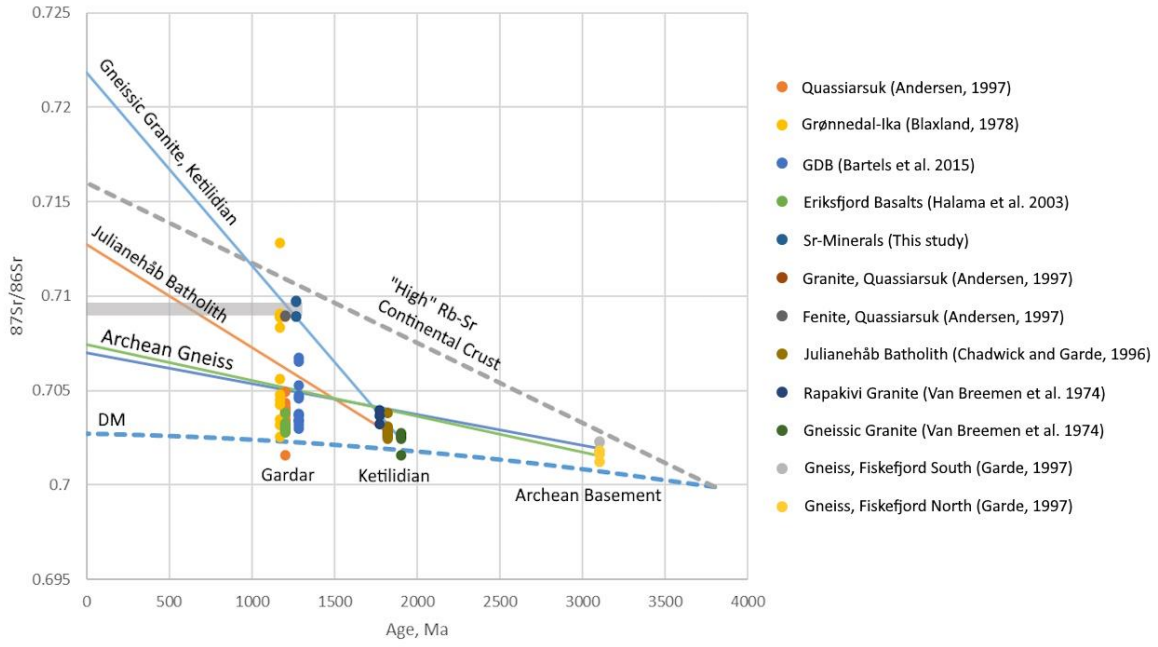

Figure 7.12: Plot of initial $^{87}Sr/^{86}Sr$-ratios for a selection of the Gardar intrusions. All the initial ratios have been recalculated based on a decay constant of $1.3972*10^{-11}$. See the text for a full description

The plot display that there are two distinct group of initial $^{87}Sr/^{86}Sr$-ratios for the selected Gardar magmas. The Grønnedal-Ika complex, the Quassiarsuk Complex (Andersen, 1997), the Eriksfjord basalt (Halama et al., 2003) as well as the Gardar Brown Dykes (Bartels et al. 2015) have initial $^{87}Sr/^{86}Sr$-ratios between 0.703 and 0.705, close to the evolution line of the depleted mantle and in agreement with their proposed mantle-derived magma source. The jørgensenite, stenonite, cryolite and fluorite from Ivigtut, as well as the basement granite and fenite from Quassiarsuk (Andersen, 1997), all plot closer to the theoretical evolution line of a "High" Rb-Sr continental crust.

This holds implications as to how to interpret the $^{87}Sr/^{86}Sr$-signature of jørgensenite and stenonite. The value itself indicate either a magma source derived from partial melting of the continental crust, or transport of radiogenic Sr leached from the wall rocks into a magma with less radiogenic Sr-isotope composition. The latter suggestion would imply that the continental crust was the primary source of Sr^{2+} in the fluid. This proposal is supported by the relationships between the different South-Greenlandic lithologies in Fig. 7.12, where it can be seen that the evolution line of the gneissic granites of a Ketilidian origin, transects the points of the Sr-minerals, and these rocks could therefore be considered a potential source.

However, the problem with the cryolite deposit is the comprehensive metasomatic alteration of the main granitic stock, which have altered the $^{87}Sr/^{86}Sr$-ratios, and consequently made the Sr-system an unreliable tool for the determination of the origin. However, this problem mainly affects whole-rock date, and unaltered, Sr-minerals could serve as a viable option when using the Sr-system to evaluate the origin of the deposit, if such minerals were found within the granite.

Highly heterogenous $^{87}Sr/^{86}Sr$-ratios and Rb-concentration in the wall rocks, have been documented by Blaxland (1976), Goodenough (1997), Pauly and Bailey (1999) and Goodenough et al. (2000), and has led these authors to suggest that a great deal of fluid mixing occurred at Ivigtut. This is supported by the multi-stage metasomatic alteration of the granite, and it is evident that different types of fluids have interacted with the wall-rocks. As a results, one cannot disregard the notion of mixing, and there is the possibility that initial $^{87}Sr/^{86}Sr$-ratios recorded for jørgensenite, stenonite, fluorite and cryolite, have been influenced by several sources of Sr^{2+}.

The similarity in initial $^{87}Sr/^{86}Sr^{+}$ between cryolite and jørgensenite, imply that these minerals have a common source of Sr^{2+} and that Sr^{2+} was introduced to the system during the early stages. Since the Sr^{2+} hosted in jarlite and jørgensenite seem to have originated from the replacement of celestine and strontian baryte, it also implies that the crystallization of these sulphates must have originated from the same source as the cryolite, without contamination from an external fluid. This is in contrast to the hypothesis of Hutchinson et al. (2019), in which they proposed that the baryte crystallized due to the late-stage influx of a brine, which would undoubtedly have changed $^{87}Sr/^{86}Sr$-signature. It is more likely that the system was closed from the onset of the crystallization of cryolite until the crystallization of jørgensenite, jarlite and stenonite. This also holds implications as to how to interpret the $^{87}Sr/^{86}Sr$-signature of jørgensenite, stenonite, cryolite and fluorite. If the initial $^{87}Sr/^{86}Sr$-ratio is a product of mixing between several sources of Sr^{2+}, then this mixing must have occurred before the cryolite deposit crystallized, and while it was somewhat homogenous.

The initial $^{87}Sr/^{86}Sr$-ratios of jørgensenite, stenonite, cryolite and fluorite does not necessarily rule out the hypotheses of Goodenough et al. (2000), Köhler et al. (2007) and Hutchinson et al. (2019) but could simply mean that the timeframe of Hutchinson et al. (2019) should be shifted to an earlier stage of the consolidation of the deposit. It therefore seems justified, that instead of interpreting the initial $^{87}Sr/^{86}Sr$-ratios towards a crustal source of Sr^{2+}, one should see the $^{87}Sr/^{86}Sr$-signature in light of the previous research and attest it to mixing between different sources. However, further studies are obviously required in order to present a conclusion on this matter.

8 Conclusions

The purpose behind this thesis was to investigate the nature of the two isostructural minerals jarlite and jørgensenite, and to provide a new and detailed insight into their crystal chemistry.

The new site-assignment has now made it possible to describe the crystal chemistry of jørgensenite and jarlite with a higher level of detail. The more detailed site-assignment also made it possible to accurately define the chemical difference between jarlite and jørgensenite. The difference between jarlite and jørgensenite should therefore solely be recognized as their respective content of Mg and Na at the *Na2*/*Mg*-site, and their general chemical formula should be recognized as,

$$(Na, Li)_2\ (Sr, Ba)_2\ (Sr, Ba, Ca)_4\ (Sr_{8-y}\ (K_a\ Na_b)_{a+b=y})_8\ (Na_x, Mg_y)_{x+y=2}\ Al_{12}F_{64}(OH, F)_4$$

where the ordering of cation sites are as follows; *Na1*, *Sr1*, *Sr2*, *Sr3*, *Na2*, *Al1+Al2*, and where x > y defines a jørgensenite, and x < y a jarlite.

This new classification scheme made it possible to identify a "new" mineral species, which should be recognized as the Ba-analogue of jørgensenite. Furthermore, it is proposed that jørgensenite, jarlite and the Ba-analogue should be considered a part of a larger group of isostructural Sr-aluminofluorides, which may also include calcjarlite, and several theoretical endmembers.

As to the crystal structure of jarlite and jørgensenite, it was found that the *Sr2*-site should be recognized to have a higher coordination number, than that which have been previously described. A coordination number of 11 seems more likely, and bonds between *Sr2*-site and *F8*-site were found to have a significant effect on the overall bond valence sums for the *Sr2*-site. Additionally, it was found that the crystal structure of jarlite and jørgensenite, do not contain any distinct *O*-site, and that OH^- and H_2O is incorporated through substitution primarily located at the *F9*-site. The new placement of O also provided a suitable size-based environment within the crystal structure, for the incorporation of OH^- and/or H_2O molecules.

It was also found that jørgensenite and jarlite occur as pseudomorphs after celestine and/or baryte, which holds the implication that the hypothesis of Pauly and Bailey (1999) are wrong,

and that these minerals grew from the dissociation of celestine and or/baryte and not from a fractionated fluid. This means that baryte and celestine should be recognized to have formed earlier than previously proposed. However, it seems unlikely that baryte and celestine are primary Ba- and Sr-phases.

Comparison of $^{87}Sr/^{86}Sr$-ratios for cryolite, fluorite, jørgensenite and stenonite indicate that the cryolite deposit should be treated as a closed system during it subsequent evolution from the formation of first stage cryolite through the later stages. As to the origin of the deposit, the high degree of fluid activity and mixing which is evident from the country rocks around Ivigtut, makes the interpretation of the initial $^{87}Sr/^{86}Sr$-ratio, and the subsequent source of Sr^{2+} inconclusive. The initial $^{87}Sr/^{86}Sr$-ratios could be attested to evolution from the partial melting or fluid leaching of the continental crust, but this would be in contrast to Goodenough et al. (2000), Köhler et al. (2007) and Hutchinson et al. (2019). Further research is obviously required.

9 Further Studies

The work on this thesis has unveiled that there still is a lot to learn about the Ivigtut cryolite deposit and its complex mineralogy. Additionally, several of the results and tentative conclusions presented in this thesis, would benefit to be further elaborated upon by future studies.

- The new mineral, which should be recognized as the Ba-analogue of jørgensenite, should be given a proper name, and it should be fully described. Its paragenesis with bøggildite needs to be investigated so as to obtain the knowledge of its crystallization environment.
- The proposed group of isostructural Sr-aluminofluorides should be further researched, and emphasis should be placed on how the different group members are related in terms of their crystal chemistry.
- It is also deemed necessary that calcjarlite is reevaluated in order for its crystal structure and crystal chemistry to be properly described. This will also help evaluating the validity of the proposed mineral group, and to establish its true relationship to jarlite.
- It has been made clear that there still is a lot to discover concerning the cryolite deposit. Our collective knowledge of one of the most interesting localities there is, would benefit greatly from a renewed petrological investigation of the different segments which made up the cryolite deposit. It has been evident from the work on this thesis that such studies would undoubtedly enhance our understanding of the mineralogical heterogeneity of the deposit as well as enhance our understanding of the processes which have taken place.
- As a continuation of the former point, there are several mineral occurrences which would benefit from further studies. The occurrence of baryte and celestine should be further studied, so as to provide insight into when these minerals crystallized, and to identify if there exist several generations of these phosphates. Our knowledge of stenonite would also benefit from a similar study, of which the goal should be to properly describe the different generations of stenonite, which has been inferred to exist through the work on this thesis.

Bibliography

Andersen, E. K., Ploug-Sørensen, G. (1991). «The structure of acuminite, a strontium aluminium fluoride mineral", in *Zeitschrift für Kristallographie*, **194**, 221-227

Andersen, T. (1997). "Age and petrogenesis of the Qassiarsuk carbonatite-alkaline silicate volcanic complex in the Gardar rift, South Greenland", in *Mineralogical Magazine*, **61**, 499-513

Andersen, T. (1997). "Age and petrogenesis of the Qassiarsuk carbonatite-alkaline silicate volcanic complex in the Gardar rift, South Greenland", *Mineralogical Magazine*, **61**, 499-513

Andersen, T. (2008). "Coexisting Silicate and Carbonatitic Magmas in the Qassiarsuk Complex, Gardar Rift, Southwest Greenland", in *The Canadian Mineralogist*, **46**, 933-950

Andersen, T. (2013). "Age, Hf isotope and trace element signatures of detrital zircons in the Mesoproterozoic Eriksfjord sandstone, southern Greenland: are detrital zircons reliable guides to sedimentary provenance and timing of deposition?", in *Geological Magazine*, **150**:3, 426-440

Atencio, D.; Andrade, M. B.; Bastos Neto, A. C.; Pereira, V. P. (2017). "Ralstonite renamed hydrokenoralstonite, coulsellite renamed fluornatrocoullselite, and their incorporation into the pyrochlore supergroup", *The Canadian Mineralogist*, **55**, 115-120

Atkins, P.; de Paula, J.; Keeler, J. (2018). *Atkins' Physical Chemistry, 11th edition*. Oxford University Press: Oxford

Bailey, J. C. (1980). «Formation of cryolite and other aluminofluorides: A petrological review", in *Bulletin of the Geological Society of Denmark*, **29**, 1-45

Balić-Žunić, T. (2014). "The crystal structure of bøgvadite ($Na_2SrBa_2Al_4F_{20}$), in *Mineralogy and Petrology*, **108**, 479-486.

Ball, Sydney H. (1923). «The Mineral Resources of Greenland" in *Meddelelser om Grønland*, nr. **63**.

Bartels, A.; Nielsen, T. F. D.; Lee, Seung R.; Upton, B. G. J. (2015). «Petrological and geochemical characteristics of Mesoproterozoic dyke swarms in the Gardar Province, South Greenland: Evidence for a major sub-continental lithospheric mantle component in the generation of the magmas" in *Mineralogical Magazine*, **79**:4, 909-939

Bastos Neto, A. C.; Pereira, V. P.; Ronchi, Luiz H.; de Lima, E. F.; Frantz, J. C. (2009). «The world-class Sn, Nb, Ta, F (Y, REE, Li) deposit and the massive cryolite associated with the

albite-enriched facies of the Madeira A-type granite. Pitinga mining district, Amazonas State, Brazil", *Canadian Mineralogist*, **47**:6, 1329-1357

Berthelsen, A. (1962). "On the geology of the country around Ivigtut, SW-Greenland", in *Geologische Rundschau*, **52**, 269-280

Berthelsen, A.; Henriksen, N. (1975). *Geological map of Greenland 1:100,000. Ivigtut 61 V.1 Syd. The Orogenic and Cratogenic Geology of a Precambrian Shield Area, descriptive text.* Copenhagen: Geological Survey of Greenland

Berzelius, J. J. (1824). "Undersökning af flusspatssyran och dess märkvärdigaste föreningar» in *Kongliga Vetenskapsacademiens Handlingar för år 1823*. P. A. Norstedt och Söner: Stockholm.

Blake, A. J. (2009a). "Practical aspects of data collection" in *Crystal Structure Analysis: Principle and Practice (2nd edition)*, edited by Clegg, William., Blake, Alexander., Cole, Jacqueline M., Evans, John S. O., Main, Peter., Parsons, Simon., Watkin, David J. Oxford: Oxford University Press

Blake, A. J. (2009b). "Background theory for data collection" in *Crystal Structure Analysis: Principle and Practice (2nd edition)*, edited by Clegg, William., Blake, Alexander., Cole, Jacqueline M., Evans, John S. O., Main, Peter., Parsons, Simon., Watkin, David J. Oxford: Oxford University Press

Blaxland, A. (1976). "Rb-Sr Isotopic Evidence for the Age and Origin of the Ivigtut Granite and Associated Cryolite Body, South Greenland", *Economic Geology*, **71**, 864-869

Blaxland, A. B.; Van Breemen, O.; Emeleus, C. H.; Anderson, J. G. (1978). "Age and origin of the major syenite centers in the Gardar province of south Greenland: Rb-Sr studies", *Geological Society of America Bulletin*, **89**, 231-244

Brese, N. E. and O'Keeffe, M. (1991). "Bond-Valence Parameters for Solids", *Acta Crystallographica*, **B47**, 192-197

Bridgewater, D.; Watson, J.; Windley, B. F. (1973). "The Archean Craton of the North Atlantic Region", in *Philosophical Transactions of the Royal Society of London:* "A Discussion on the Evolution of the Precambrian Crust", **273**:1235, 493-512

Brown, I. D. (2009). "Recent Developments in the Method and Applications of the Bond Valence Model", *Chemical Reviews*, **109**, 6858-6919

Bøgvad, R. (1933). "New Minerals From Ivigtut, Greenland" in *Meddelelser om Grønland*, **92**:8, 1-11.

Chadwick, B.; Garde, A. A. (1996). "Palaeoproterozoic oblique plate convergence in South Greenland: a reappraisal of the Ketilidian Orogen", in Brewer, T. S. (ed.), *Precambrian Crustal Evolution in the North Atlantic Region, Geological Society Special Publication,* **112**: 179-196

Coulson, I.M.; Goodenough, K. M.; Pearce, N. J. G.; Leng, M. J. (2003). "Carbonatites and lamprophyres of the Gardar Province – a "window" to the sub-Gardar mantle?", *Mineralogical Magazine,* **67**:5, 855-872

Elbo, J., G. (1948). "Cryolite and the Mine at Ivigtut, West Greenland" in *Polar Record,* **5**:35-36, 185-188.

Farrugia, L. J. (2012). "WinGX and ORTEP for Windows: an update", *Journal of Applied Crystallography*, **45**, 849-854

Faure, G.; Mensing, T. M. (2005). *Isotopes: Principles and Applications, 3rd edition*. John Wiley & Sons, inc: New Jersey

Finch, A. A.; Goodenough, K. M.; Salmon, H. M.; Andersen, T. (2001). "The petrology and petrogenesis of the North Motzfeldt Centre, Gardar Province, South Greenland", in *Mineralogical Magazine*, **65**:6, 759-774

Gagné´O. C.; Hawthorne, F. C. (2015). "Comprehensive derivation of bond-valence parameters for ion pairs involving oxygen", *Acta Crystallographica*, **B71**, 562-578

Gagné, O. C.; Hawthorne, F. C. (2016). "Bond-length distributions for ions bonded to oxygen: alkali and alkaline-earth metals", *Acta Crystallographica*, **B72**, 602-625

Garde, A. A. (1997). "Accretion and evolution of an Archaean high-grade grey gneiss - amphibolite complex: the Fiskefjord area, southern West Greenland", *Geology of Greenland Survey Bulletin* **177**.

Garde, A.A.; Hamilton, M.A.; Chadwick, B.; Grocott, J.; McCaffrey, K. J. W. (2002). "The Ketilidian Orogen of South Greenland: geochronology, tectonics, magmatism and fore-arc accretion during Paleoproterozoic oblique convergence", in *Canadian Journal of Earth Sciences,* **39**, 765-793.

Garrels, R. M.; Christ, C. L. (1965). *Solutions, Minerals and Equilibria*. Harper and Row: New York

Geller, S. (1971). "Refinement of the crystal structure of cryolithionite, $\{Na_3\}[Al_2](Li_3)F_{12}$", *American Mineralogist*, **56**, 18-23

Gladkochub, D. P.; Donskaya, T. V.; Sklyarow, E. V.; Kotov, A. B.; Vladykin, N.V.; Pisarevsky, S. A.; Larin, A. M.; Salnikova, E. B.; Saveleva, V. B.; Sharygin, V. V.; Starikova, A. E.; Tolmacheva, E.V.; Velikoslavinsky, S.D.; Mazukabzov, A.M.; Bazarova, E. P.; Kovach, V. P.; Zagornaya, N. Yu.; Alymova, N. V.; Khromova, E. A. (2017). "The unique Katugin rare-metal deposit (southern Siberia): Constraints on age and genesis", *Ore Geology Reviews*, **91**, 246-263

Goodenough, K. M. (1997). *Geochemistry of Gardar Intrusions in the Ivigtut area, South Greenland*. PhD thesis, Edinburg University, unpublished

Goodenough, K. M.; Upton, B. G. J.; Ellam, R. M. (2000). "Geochemical evolution of the Ivigtut granite, South Greenland: a fluorine-rich "A-type" intrusion", in *Lithos*, **51**, 205-221

Guiseppetti, G.; Tadini C. (1983). "Structural analysis and refinement of Bolovian creedite, $Ca_3Al_2F_8(OH)_2(SO_4)\cdot 2H_2O$: The role of the hydrogen atoms", *Neues Jahrbuch fur Mineralogie*, **1**, 69-78

Halama, R.; Wenzel, T.; Upton, B. G. J.; Siebel, W.; Markl, G., (2003). "A geochemical and Sr-Nd-O isotopic study of the Proterozoic Eriksfjord Basalts, Gardar Province, South Greenland: Reconstruction of an OIB signature in crustally contaminated rift-related basalts", in *Mineralogical Magazine*, **67**:5, 831-853

Hanor, J. S. (2000). "Barite-Celestine Geochemistry and Environments of Formation", *Reviews in Mineralogy and Geochemistry*, **40**:1, 193-275

Hawthorne, F. C. (1982). "The crystal structure of boggildite", in *Canadian Mineralogist*, **20**, 263-270

Hawthorne, F. C. (1983). "The crystal Structure of jarlite", in *Canadian Mineralogist*, **21**, 553-560.

Hawthorne, F. C. (1984). "The Crystal Structure of Stenonite and the Classification of the Aluminofluoride Minerals" in *Canadian Mineralogist*, **22**, 245-251.

Hawthorne, F. C., Burns, P. C. (1997). "The Crystal Structure of Jørgensenite" in *Canadian Mineralogist*, **35**, 1509-1513.

Hawthorne, F. C., Herwig, S. (2021). "A Structure Hierarchy for the Aluminofluoride Minerals", *The Canadian Mineralogist*, **59**, 211-241.

Hawthorne, F. C.; Ferguson, R. B. (1983). "The Crystal Structure of Pachnolite", *Canadian Mineralogist*, **21**, 561-566

Hutchinson, W.; Babiel, R. J.; Finch, A. A.; Marks, M. A. W.; Markl, G.; Boyce, A. J.; Stüeken, E. E.; Friis, H.; Borst, A. M.; Horsburgh, N. J. (2019). "Sulphur isotopes of alkaline

magmas unlock long-term records of crustal recycling on Earth", *Nature Communications*, **10**:4208, 12 pp

Hutchison, W.; Finch, A. A.; Borst, A. M.; Marks, M. A. W.; Upton, B. G. J.; Zerkle, A. L.; Stüeken, E. E.; Boyce, A. J. (2021). "Mantle sources and magma evolution in Europe's largest rare earth element belt (Gardar Province, SW Greenland): New insights from sulfur isotopes", in *Earth and Planetary Science Letters*, **568**, 1- 16

Imreh, J.; Mârza, I. (1978). "Baryt-Kristalle aus Tarna Mare (Rumänien)", *Tschermaks Mineralogische Und Petrofraphische Mitteilungen*, **25**, 165-169

Jarl, C. F. (1909). *Fabrikken Öresund 1859-1909: Kryolitindustriens historie og udvikling*. J. Jørgensen & Co.: København.

Johnstrup, F. (1878). *Gieseckes Rejse I Grønland*. Bianco Lunos Bogtrykkeri: København.

Kalsbeek, F.; Larsen, L. M.; Bondam, J. (1990). *Geological map of Greenland 1:500,000, Sydgrønland Sheet 1, Descriptive text.* Copenhagen: Geological Survey of Greenland

Kampf, A. R.; Colombo, F.; González Del Tánago, J. (2010). "Carlhintzeite, $Ca_2AlF_7 \cdot H_2O$, from the Gigante granitic pegmatite, Córdoba province, Argentina: description and crystal structure", *Mineralogical Magazine*, **74**:4, 623-632

Kiefer, David M. (2002). "Soda Ash, Solvay Style" in *Today's Chemist at Work*¸**11**:2, 87-88.

Koziol, A. (2004). "Experimental determination of siderite stability and application to Martian Meteorite ALH84001", *American Mineralogst*, **89**, 294-300

Kragh, H. (1999). «From curiosity to industry: The early history of cryolite soda manufacture" in *Annales of Science*, **52**:3, 285-301.

Kruse, F. (2016). "Historical Perspectives- The European Commercial Exploitation of Arctic Mineral Resources After 1500 AD" in *Polarforschung*, **86**:1, 15-26.

Köhler, J.; Konnerup-Madsen, J.; Markl, G. (2008). «Fluid geochemistry in the Ivigtut cryolite deposit, South Greenland", in *Lithos*, **103**, 369-392

Köhler, J.; Schönenberger, J.; Upton, Brian.; Markl, G. (2009). "Halogen and trace-element chemistry in the Gardar Province, South Greenland: Subduction-related mantle metasomatism and fluid exsolution from alkaline melts", in *Lithos*, **113**, 731-747

Lathinen, R; Garde, A. A.; Melezhik, V. A.; (2008). "Paleoproterozoic evolution of Fennoscandia and Greenladn", *Episodes, Journal of International Geoscienc*e, **31**:1, 20-28

Litvin, A.L.; Petrunina, A.A.; Ostapenko, S.S. (1980). "Crystal structure of usovite", *Dopovidi Akademii Nauk Ukrainskoi RSR, Seriya B, Geologichni Khimichni Ta Biologichni Nauki*: **3**, 47-80.

Lloyd, T. (1953). «Ivigtut Cryolite and Modern Greenland" in *Canadian Geographer*, **1**:3, 39-52.

Marks, M. A. W.; Markl, G. (2017). "A global review on agpaitic rocks", in *Earth-Science Reviews*, **173**, 229-258

Marocchi, M.; Bureau, H.; Figuet, G.; Guyot, F. (2011). "*In-situ* monitoring of the formation of carbon compounds during the dissolution of iron (II) carbonate (siderite)", *Chemical Geology*, **290**, 145-155

Massa, W. (2000). *Crystal Structure Determination*. Berlin: Spinger Verlag

McCreath, J. A.; Finch, A. A.; Simonsen, S. L.; Donaldson, C. H.; Armour-Brown, A. (2012). "Independent ages of magmatic and hydrothermal activity in alkaline igneous rocks: The Motzfeldt Centre, Gardar Province, South Greenland", in *Contribution to Mineralogy and Petrology*, **163**, 967-982

Meert, J. G.; Santosh, M. (2017). "The Columbia supercontinent revisited", in *Gondwana Research*, **50**, 67-83.

Mitolo, D.; Garavelli, A.; Balić-Žunić, T.; Acquafredda, P. (2013). «Leonardsenite, $MgAlF_5(H_2O)_2$, a new mineral species from Eldfell Volcano, Heimaey Island, Iceland", *The Canadian Mineralogist*, **51**, 377-386.

Momma, K.; Izumi, F. (2011). "VESTA 3 for the three-dimensional visualization of crystal, volumetric and morphology data", *Journal of applied crystallography*, **44**, 1272-1276

Müller, P. (2006). "Crystal structure refinement", in Müller, P. (ed.). *Crystal Structure Refinement: A Crystallographers Guide to SHELXL*. Oxford: Oxford University Press

Nordenskiöld, E. A. (1885). *Den Andra Dicksonska Expeditionen Till Grönland*. F. & G. Beijers Förlag: Stockholm

Othman, D. B.; Mireille, P.; Allègre, C. J. (1984). «Nd-Sr isotopic composition of granulites and constraints on the evolution of the lower continental crust", *Nature*, **307**, 510-515

Pauling, L. (1960). *The Nature of the Chemical Bond and The Structure of Molecules and Crystals: An Introduction to Modern Structural Chemistry, 3rd edition*. Cornell University Press: New York

Pauly, H. (1956). «Bøggildite. A new phosphate-flouride from Ivigtut, South Greenland", in *Grønlands Geologiske Undersøkelse,* **14**, 3-17

Pauly, H. (1962). "Stenonite, A New Carbonate-Fluoride from Ivigtut, South-Greenland" in *Meddelelser om Grønnland*, **169**:9, 1-29.

Pauly, H. (1986). "Cryolithionite and Li in the Cryolite Deposit Ivigtut, South Greenland", *Matematisk-fysiske Meddelelser,* **42**:1, 24pp

Pauly, H. (1992). "Topaz, prosopite and closing stages of formation of the Ivigtut cryolite deposit, South Greenland", in *Meddelelser om Grønland, Geoscience,* **28**, 22 pp.

Pauly, H. (1993). «Columnar and radiating aggregates with jarlite from the Ivigtut cryolite deposit, South Greenland" in *Bulletin of the Geological Society of Denmark,* **40**, 272-279.

Pauly, H.; Bailey, J. C. (1999). "Genesis and evolution of the Ivigtut cryolite deposit, SW Greenland" in *Meddelelser om Grønland,* **37**, 60 pp

Pauly, H.; Hawthorne, F. C.; Burns, P. C.; Ventura, G. D. (1997). "Jørgensenite, $Na_2(Sr,Ba)_{14}Na_2Al_{12}F_{64}(OH, F)_4$, A New Aluminofluoride From Ivigtut, Greenland" in *Canadian Mineralogist,* **35**, 175-179.

Pauly, H.; Nielsen, R. N. (1992). "Jarlite: Order-Disorder Structure Suggested by Optics, Results of New Analysis and Empirical Formula" in *Canadian Mineralogist,* **30**, 449-455.

Pauly, H.; Petersen, O. V. (1987). "Acuminite, a new Sr-flouride from Ivigtut, South Greenland", in *Neues Jahrbuch Für Mineralogie, Monatshefte*, **11**, 502-514

Pauly, H.; Petersen, O. V. (1988). "Bøgvadite, $Na_2SrBa_2Al_4F_{20}$, a new fluoride from the cryolite deposit, Ivigtut, S. Greenland", in *Bulletin of Geological Society of Denmark,* **37**, pp. 21-30.

Piper, J. D. A.; Thomas, D. N.; Share, S.; Rui, Z. Q. (1999). "The paleomagnetism of (Mesoproterozoic) Eriksfjord Group red beds, South Greenland: multiphase remagnitization during the Gardar and Grenville episodes", in *Geophysical Journal International*, **136**, 739-756

Poulsen, V. (1964). "The Sandstones of the Precambrian Eriksfjord Formation in South Greenland", in *The Geological Survey of Greenland,* **2**: 16 pp

Povarennykh, A.S. (1973) "On the new mineral species calcjarlite", *Konstitutsiya i Svoistva Mineralov*: **7**, 131-135.

Ratvik, A. P.; Mollaabbasi, R.; Alamdari, H. (2022). «Aluminium production process: from Hall-Héroult to modern smelters» in *ChemTexts*, **8**:10.

Raudsepp, M. (1995). "Recent Advances in the Electron-Probe Micro-Analysis of Minerals for the Light Elements" in *The Canadian Mineralogist*, **33**, 203-218

Rink, H. J. (1852). *Om Monopolhandelen paa Grønland*. Louis Klein: Copenhagen,

Seager, A. F.; Davidson, W. F. (1952). "Changes in habit during the growth of baryte crystals from the north of England", *Mineralogical magazine and journal of the Mineralogical Society*, **29**:217, 885-894

Sejersen, F. (2014). *Efterforskning og udnyttelse av af råstoffer i Grønland i historisk perspektiv: Baggrundspapir. Udvalget for samfundsgavnlig udnyttelse af Grønlands natourresourcer*. Copenhagen.

Shannon, R. D. (1976). "Revised Effective Ionic Radii and Systematic Studies of Interatomic Distances in Halides and Chalcogenides", *Acta Crystallographica*, **A32**, 751-767

Sheldrick, G. M. (2008). "A Short History of SHELX" in *Acta Crystallographica Section A: Foundations of Crystallography*, **64**:1, 112-122.

Sheldrick, G. M. (2015). "Crystal structure refinement with SHELXL", *Structural Chemistry*, **71**:1, 3-8

Soen, O. I.; Pauly, H. (1967). «A sulphide paragenesis with pyrrhotite and marcasite in the siderite-cryolite ore of Ivigtut, South Greenland", *Meddelelser om Grønland,* **175:**5, 60pp

Solberg, T. N. (1982). "Fluorine electron microprobe analysis: variations of X-ray peak shape" in *Microbeam Analysis*. San Francisco Press, Inc., San Francisco, California.

Starikova, A. E.; Sharygin, V. V.; Sklyarov, E. V. (2017). "Ba-Dominant Fluoroaluminates from the Katugin Rare-Metal Deposit (Transbaikalia, Russia)", *Doklady Akademii Nauk*, **472**:2, 180-184

Strøm Tejsen, A. (1977). «The History of the Royal Greenland Trade Department" in *Polar Record*, **18**:116, 451-474.

Sørensen, A. K. (2007). «Denmark-Greenland in the twentieth Century" in *Meddelelser om Grønnland*, **34**, 204

Thomsen, J. (1862). «Nogle meddelelser angaaende Kryolithindustrien» in *Tidsskrift for Physik og Chemi samt Disse Videnskabers Anvendelse*, **1**:1, 321-332

Upton, B. G. J. (2013). "Tectono-magmatic evolution of the younger Gardar southern rift, South Greenland", in *Geological Survey of Denmark and Greenland Bulletin*, **29**, 124 pp

Upton, B. G. J.; Emeleus, C. H.; Heaman, L. M., Goodenough, K. M., Finch, A. A. (2003). "Magmatism of the mid-Proterozoic Gardar Province, South Greenland: chronology, petrogenesis and geological setting", in *Lithos*, **68**, 43-65

Ussing, N. V. (1908) "Kryoliten ved Ivigut» in *Geografisk Tidskrift,* **19**:5, *194-200*

Ussing, N. V. (1912). "Geology of the country around Julianehaab, Greenland", in *Meddelelser om Grønland*, **38**, 426 pp

Van Breemen, O.; Aftalion, M., Allaart, J. H., (1974). "Isotopic and Geochronologic Studies on Granites from the Ketilidian Mobile Belt of South Greenland", *Geological Society of America Bulletin*, **85**, 403-412

Vignola, P.; Hatert, F., Bersani, D., Diella, V., Gentile, P., Risplendente, A. (2012). «Chukhrovite-(Ca), $Ca_{4.5}Al_2(SO_4)F_{13}{\cdot}H_2O$, a new mineral species from the Val Cavallizza Pb-Zn-(Ag) mine, Cuasso al Monte, Varese province, Italy", *European Journal of Mineralogy*, **24**:6, 1069-1076

Wegman, C. E. (1938). "Geological investigations in southern Greenland. Part 1. On the structural divisions of southern Greenland", in *Meddelelser om Grønland*, **113**, 148pp

Weil, M. (2015). "Crysal structure of the Fe-member of usovite", *Acta Crystalographica*, **E71**, 640-643

Weil, M.; Werner, F. (2001). "The thermal dehydration of magnesium aluminum pentafluoride dihydrate: crystal structure of $MgAlF_4(H_2O)_2$ and $MgAlF_5$", *Monatshefte fur Chemie*, **132**, 769-777

Wittig, N.; Webb, M.; Pearson, D. G.; Dale, C. W.; Ottley, C. J.; Hutchinson, M.; Jensen, S. M., Luguet, A. (2010). "Formation of the North Atlantic Craton: Timing and mechanisms constrained from Re-Os isotope and PGE data of peridotie xenoliths from S.W. Greenland", in *Chemical Geology*, **276**, 166-187

Appendixes

Appendix I: Sample Descriptions

Sample PAD-IG001

Euhedral celestine and/or strontian baryte makes up most of the matrix. Where this mineral should be placed in the solid solutions series between baryte and celestine have not been established, but the EDS-analysis indicate that its content of Sr is greater that its content of Ba. Fluorite is present and mainly found as anhedral fillings between the grains of celestine. The celestine grains seem to have multiple orientations, and most of the crystals seem to be orientated along the two diagonals of the thin section. The overall texture could be attributed to brecciation and fracturing. This is supported by the orientation of the celestine crystals, and that anhedral fluorite is found in the space in between celestine.

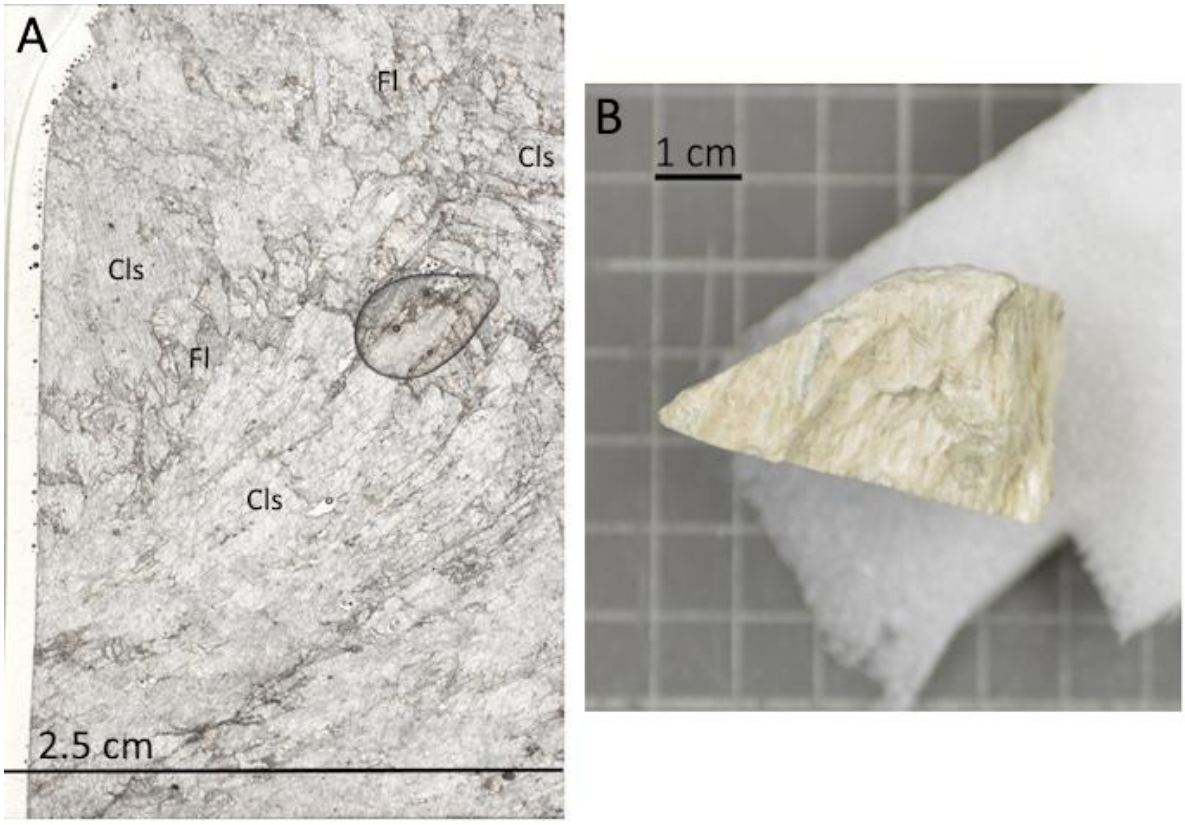

Figure AI-1: A presents a scan of the thin section in PPL, and B a photograph of the hand sample. Fl: Fluorite, Cls: Celestine

Sample PAD-IG002

The sample mainly consists of jørgensenite found as intergrown fan-shaped aggregates. Darker bands of an unidentified Al-silicate (most likely a K-mica) can be found throughout the sample, and these are mainly oriented along an E-W axis. These bands act as rims that make out jørgensenite, jarlite and bøgvadite pseudomorphs after celestine and/or strontian baryte. The pseudomorphs are highly elongated. Both single and double termination can be observed. Jørgensenite is found in paragenesis with euhedral fan-shaped aggregates of jarlite, anhedral bøgvadite and anhedral baryte. A few euhedral crystals of pyrite can be found dispersed within the matrix of jørgensenite.

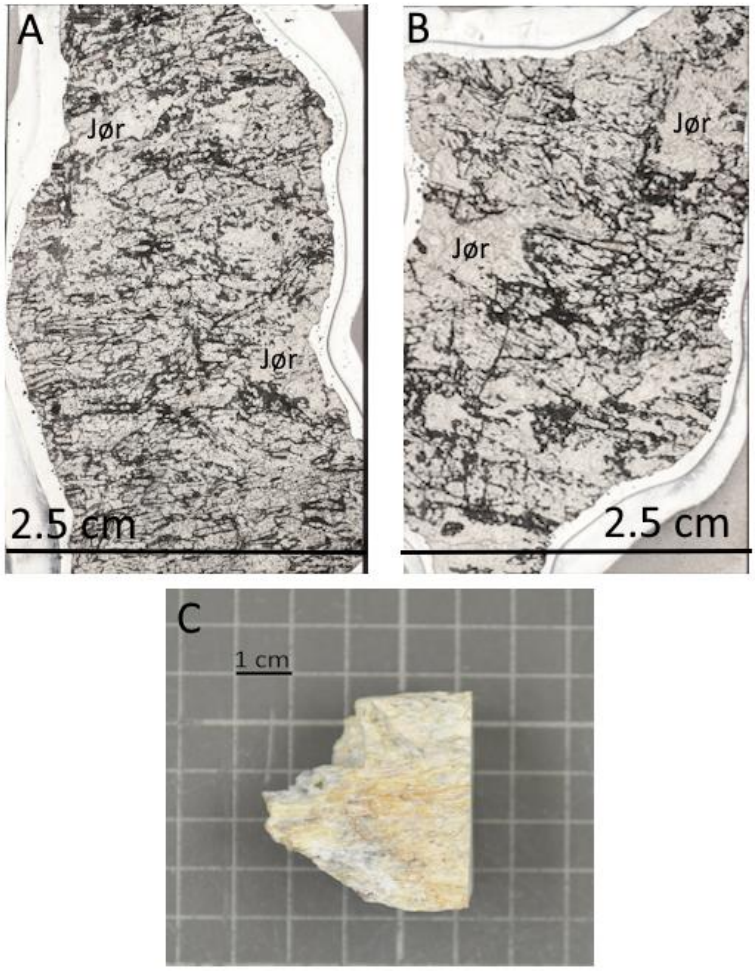

Figure AI-2: A and B presents scans of the thin sections PAD-IG002a and PAD-IG002b, B presents the hand sample. Jør: Jørgensenite. The dark bands displayed in A and B are the unknown Al-silicate.

Sample PAD-IG003

The grey mineral in Fig. AI-3B is cryolite and the pink bands are a mixture between cryptocrystalline topaz and fluorite, which occur together with jørgensenite. The topaz consists of a broader cryptocrystalline part, which evolves into localized, thin and radiating crystals. In the thin-section, the topaz can be recognized as the grey bands, and jørgensenite and fluorite are the white minerals found between these bands. The part containing cryolite is quite homogenous, and it is separated from the zone of jørgensenite by a small fractured and brecciated suture. The cryolite also contains smaller veins of hydrokenoralstonite.

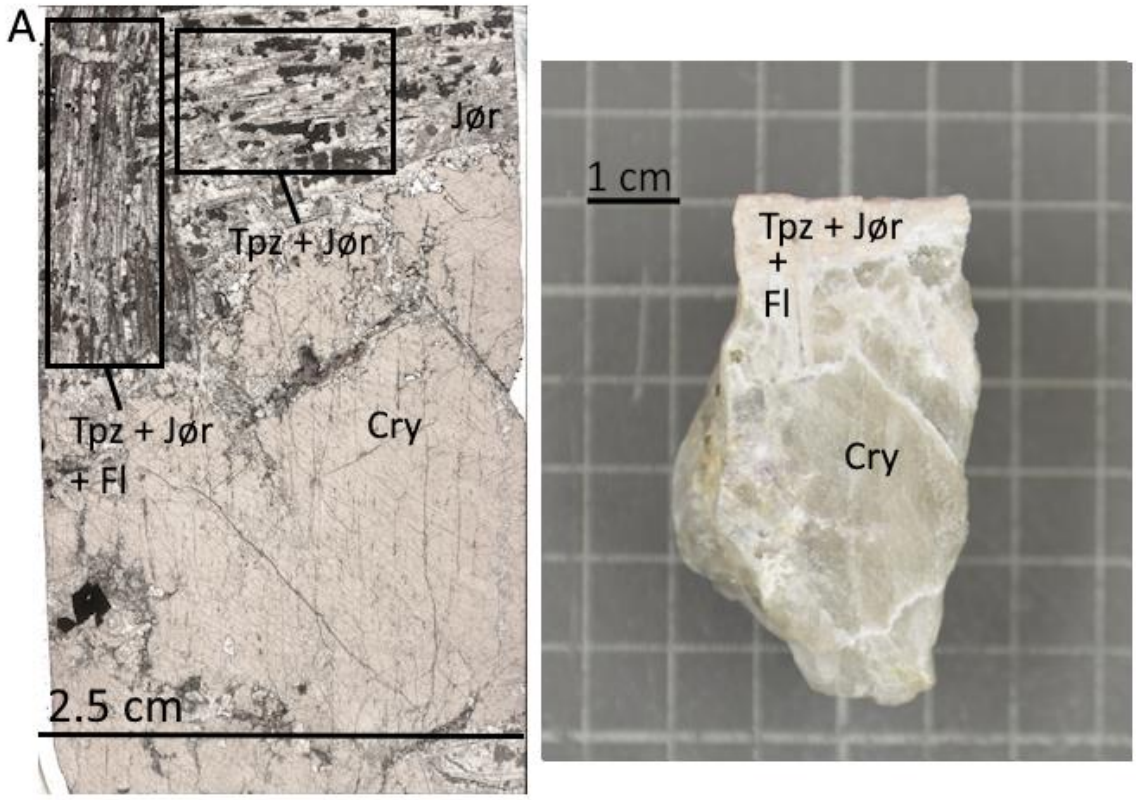

Figure AI-3: A presents a scan of the thin section and B a photograph of the hand sample. Tpz: topaz, Fl: Fluorite, Cry: Cryolite and Jør: Jørgensenite

Sample PAD-IG004

Jørgensenite and jarlite make up the majority of the sample (the grey coloured minerals in Fig. AI-4A) and occur as intergrowths of fan-shaped aggregates. Fluorite is found throughout the sample as the white mineral and occur as anhedral and irregular grains. Hydrokenrolastonite is found as both rims surrounding euhedral crystals of pyrite, as well as anhedral grains dispersed throughout the matrix of jørgensenite and jarlite. The anhedral character have been interpreted to be caused by growth restrictions inflicted by jarlite and jørgensenite. This sample also contain an unidentified Ca-Mg-Na-aluminofluoride. The proportion of elements is similar to that of fluornatrocoulsellite, a mineral which is structurally related to hydrokenoralstonite (Atencio et al. 2017). The fracture which is seen to transect the thin-section along a E-W axis, occurred when the thin-section was made.

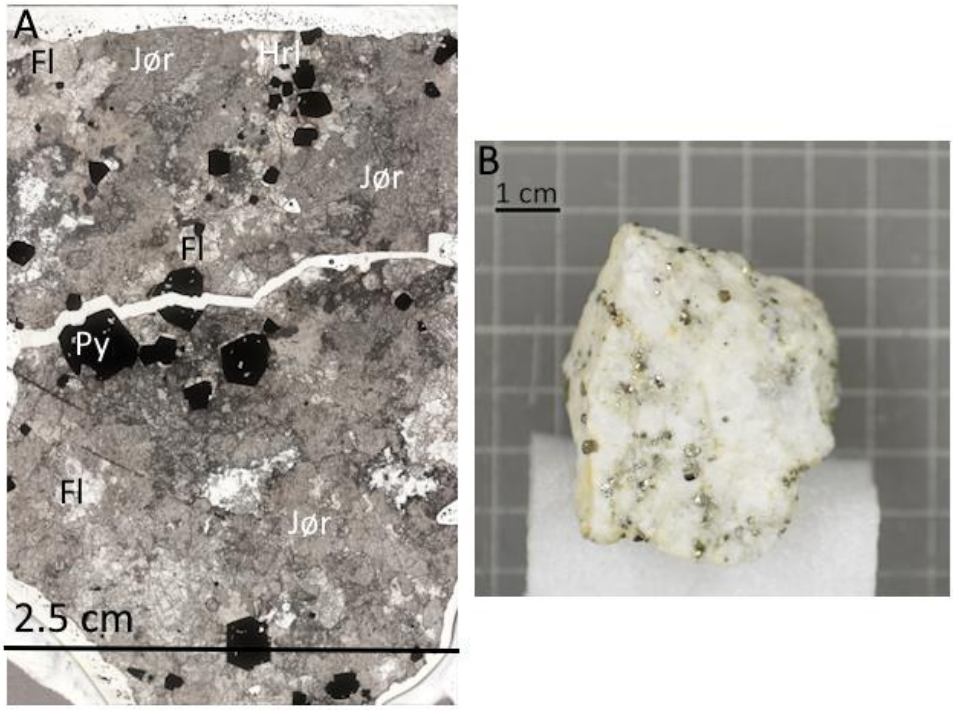

Figure AI-4: A presents a scan of the thin section and B a photograph of the hand specimen. Py: Pyrite, Fl: Fluorite, Hrl: Hydrokenoralstonite, and Jør: Jørgensenite

Sample PAD-IG005

The tan-coloured bands in Fig. AI-5A are cryptocrystalline topaz. Topaz is also found as the grey mineral in between these bands, while the white minerals are fluorite and a mixture of jørgensenite and jarlite. These bands somewhat resemble dendritical growth, which together with the cryptocrystalline nature, attest to a rapid crystallization of topaz. These bands also seem to contain a small transition in grain size, which can be viewed from the miniscule transition in the shade of the colour. Jørgensenite constitutes the majority of the matrix and occur as intergrowths of fan-shaped aggregates, together with miniscule grains of topaz. Fluorite is also found dispersed throughout the matrix as distinct cleavage fragments.

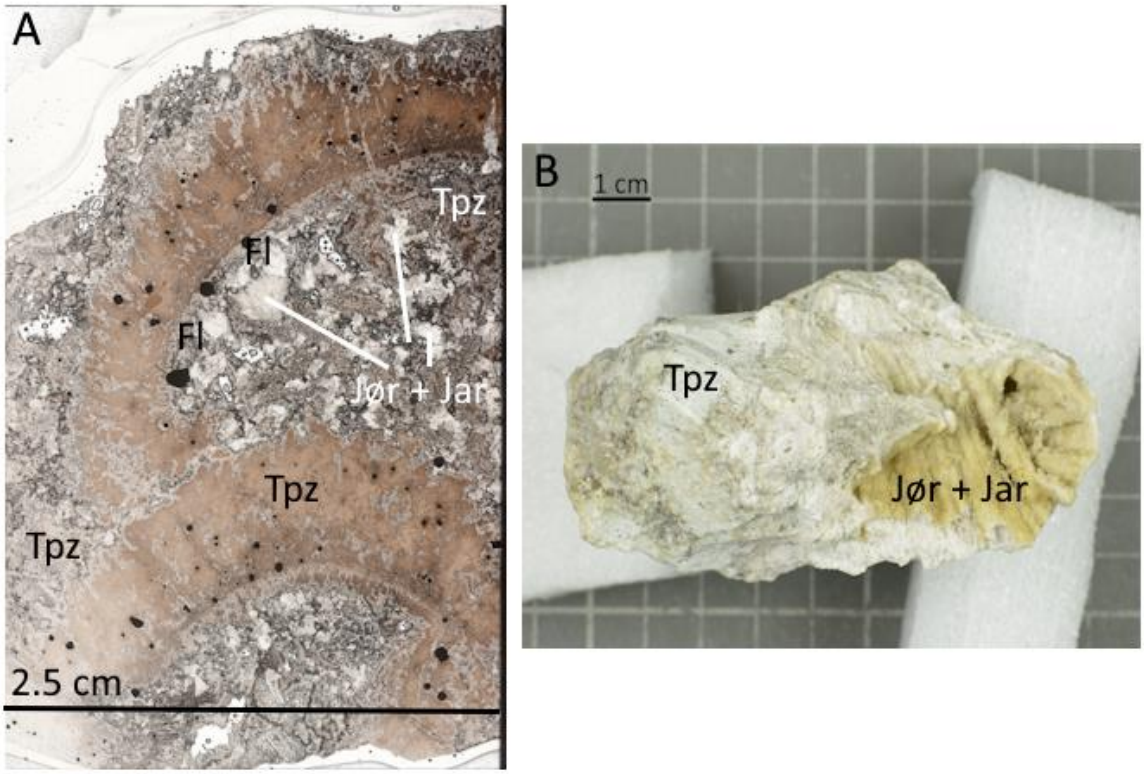

Figure AI-5: A presents a scan of the thin section, and B presents a photograph of the hand specimen. Fl: Fluorite, Tpz: Topaz, Jar: Jarlite and Jør: Jørgensenite

Sample PAD-IG006

Jørgensenite and jarlite occur as pseudomorphs after celestine, together with jarlite and bøgvadite. The rim surrounding the former crystals of celestine are made up of cryptocrystalline topaz and fluorite. The topaz rim displays the same type of dentritical texture as in Fig. AI-5, which can be attested to rapid growth. These are generally found as anhedral, irregular and slightly rounded bands. The cryptocrystalline topaz and fluorite can also be found dispersed throughout the matrix, which is dominated by intergrown fan-shaped aggregates of jørgensenite. Som of these fan-shaped aggregates of jørgensenite can also be seen to extrude into former voids and cavities, which have later been filled by pachnolite/thomsenolite. A few euhedral crystals of pyrite can be found heterogeneously dispersed throughout the sample.

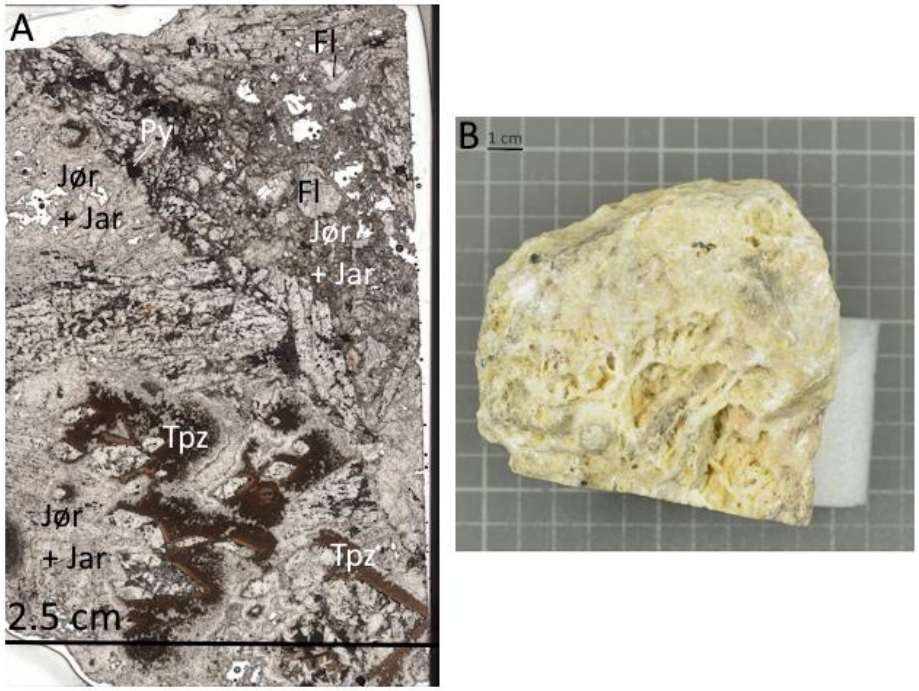

Figure AI-6: A presents a scan of the thin section and B presents a photograph of the hand specimen. Fl: Flourite, Py: Pyrite, Tpz: Topaz, Jar: Jarlite and Jør: Jørgensenite

Sample PAD-IG007

This sample is mainly made up of jørgensenite, which occur as fan-shaped aggregates, grown together to form a continuous matrix. Anhedral stenonite, fluorite, quartz and weberite can be found dispersed throughout this matrix. Fluorite can be found as angular fragments, which resemble cleavage faces and rounded, irregular fragments which displays an overall texture of corrosion. The anhedral fragments of stenonite are slightly rounded and irregular, and display a similar texture to that of fluorite. Stenonite is also found as a rim around a euhedral crystal of pyrite, with a sharp border to jørgensenite. Euhedral pyrite is heterogeneously dispersed throughout the matrix.

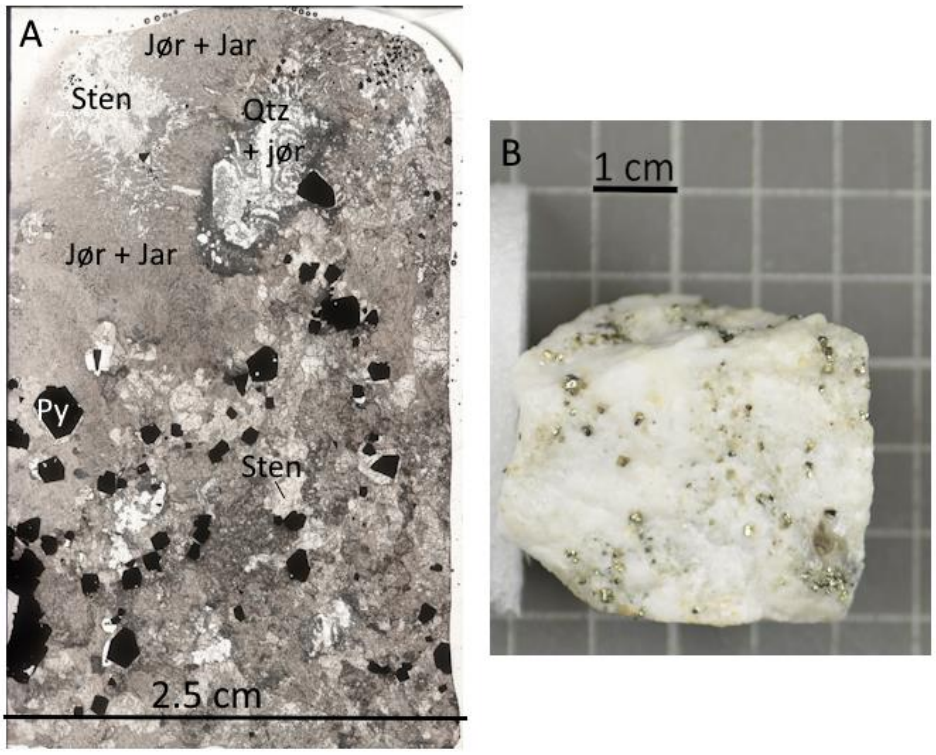

Figure AI-7: A presents a scan of the thin section and B presents a photograph of the hand specimen. Py: Pyrite, Qtz: Quartz, Sten: Stenonite, Jar: Jarlite and Jør: Jørgensenite

Sample PAD-IG008

The sample primarily consists of jørgensenite and jarlite, which occur both as fan-shaped aggregates, but also as distinct singular crystals. Euhedral to subhedral crystals of pyrite are dispersed throughout the matrix, together with some cleavage fragments of fluorite. Cryolite is found in the centre, as an anhedral and highly fractured grain.

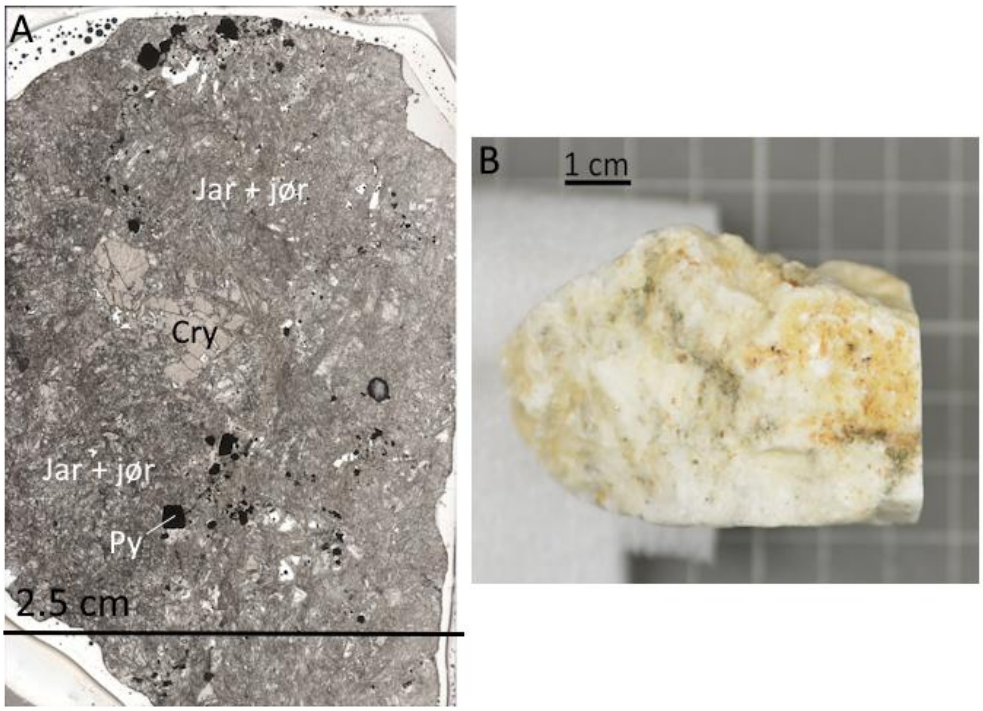

Figure AI-8: A presents a scan of the thin section and B presents a photograph of the hand specimen. Cry: Cryolite, Py: Pyrite, Jar: Jarlite and Jør: Jørgensenite

Sample PAD-IG009

The sample is made up of massive intergrowths of fan-shaped aggregates of jarlite, which dominate the sample. Interstitial, anhedral grains of cryolite and baryte can be found dispersed throughout the sample. Thin veins of topaz can be found to transect the sample. These veins contain brecciated fragments of quartz, sphalerite and an unidentified FeO.

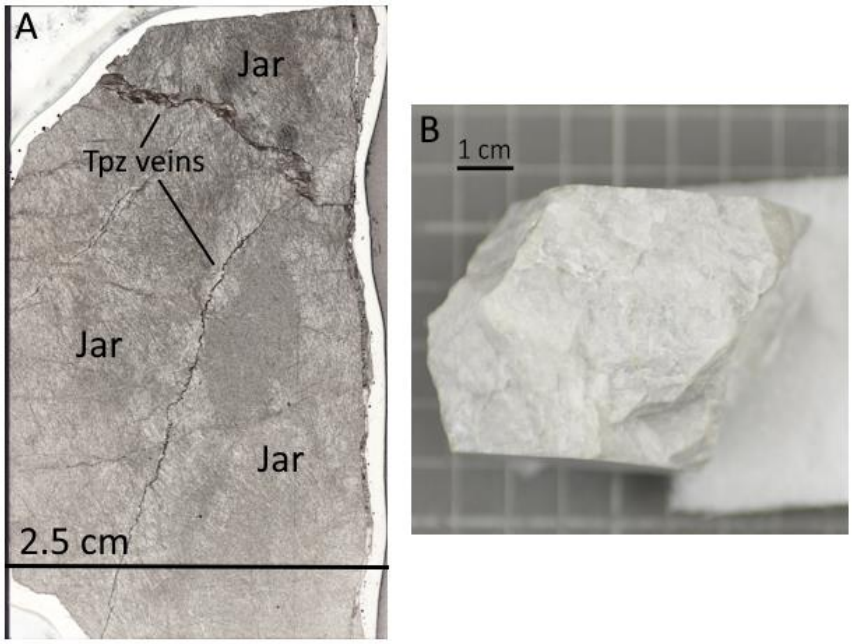

Figure AI-9: A presents a scan of the thin section and B presents a photograph of the hand specimen. Tpz: Topaz, Jar: Jarlite

Sample PAD-IG010

The sample is dominated by weberite and stenonite. Weberite occur as irregular and anhedral grains, and can be recognized as the grey mineral in Fig. AI-10A and B. Some of these grains have an angular shape which may be identified as cleavage fragments. Stenonite is found as the white coloured mineral and occur as several larger grains, with an irregular and anhedral shape. Pyrite, sphalerite and an unidentified K-mica can be found dispersed throughout this matrix. Sphalerite occur as anhedral grains, while pyrite occur as euhedral crystals. K-mica is found as euhedral, tabular crystals, and are mainly found dispersed within stenonite, in between the zones of sphalerite.

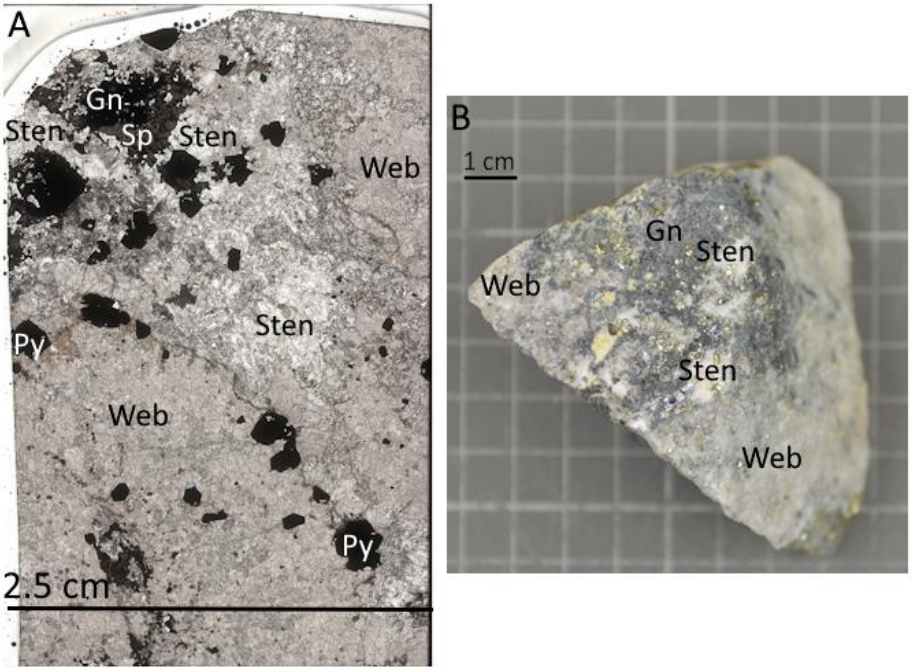

Figure AI-10: A presents a scan of the thin section and B presents a photograph of the hand specimen. Gn: Galena, Sp: Sphalerite, Py: Pyrite, Web: Weberite and Sten: Stenonite

Sample PAD-IG011

This sample mainly consist of fluorite and cryptocrystalline topaz. Jarlite occur as euhedral fan-shaped crystal aggregates, which seem to primarily have grown in cavitites which have later been filled by hydrokenoralstonite and/or pachnolite/thomsenolite. The cryptocrystalline topaz can be recognized by its brown colour, where the darker and lighter shade represents and increase in grains size from extremely fine grained (dark) to slightly less fine grained (light). Fluorite is found as the dominant white mineral and occur as bands of euhedral to subhedral crystals and cleavage fragments. Jarlite also occur as epimorphs after strontian baryte or celestine, where the preserved outline is defined by cryptocrystalline topaz and fluorite.

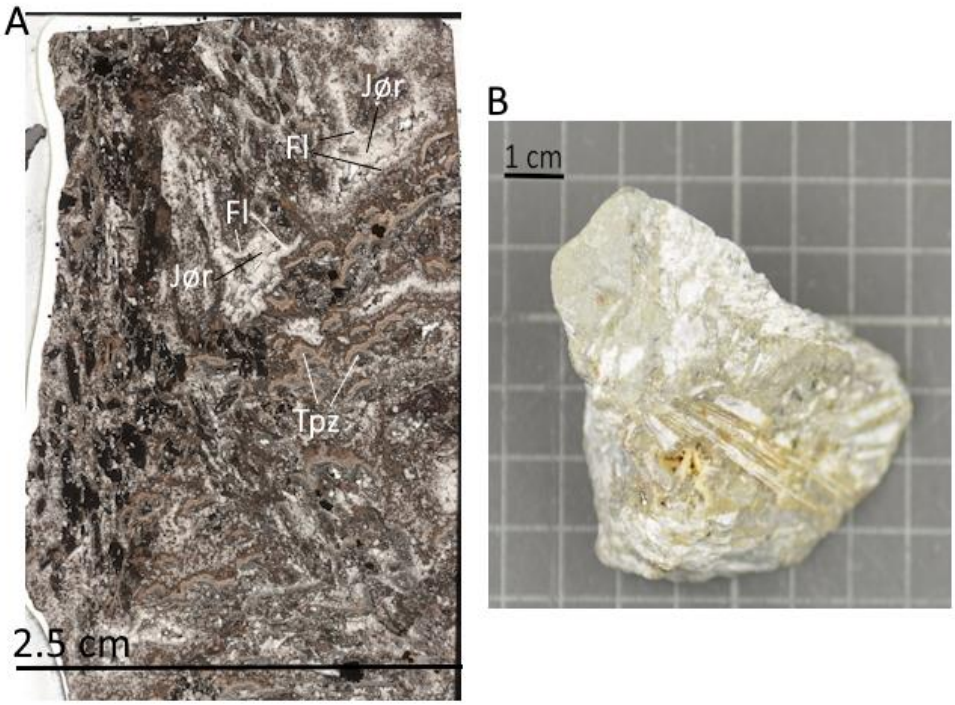

Figure AI-11: A presents a scan of the thin section and B presents a photograph of the hand specimen. Fl: Fluorite, Tpz: Topaz and Jør: Jørgensenite

Sample PAD-IG012

The majority of the sample is made up of jalite, which occur as intergrown fan-shaped aggregates. Anhedral and irregular grains of fluorite can be found dispersed throughout, and some can be found together with small, localized zone of cryptocrystalline topaz. A thin vein of pachnolite was also found to transect the sample. In the hand sample, jarlite seem to appear pale greenish, this is due to miniscule inclusions of fluorite. The zone of greenish jørgensenite is flanked by fluorite and topaz (Fig. AI-12). However, the thin section did not include the area outside of the zone of jørgensenite, so the full paragenesis is somewhat unknown. Notice the radiating texture of jørgensenite, visibly in Fig. AI-12.

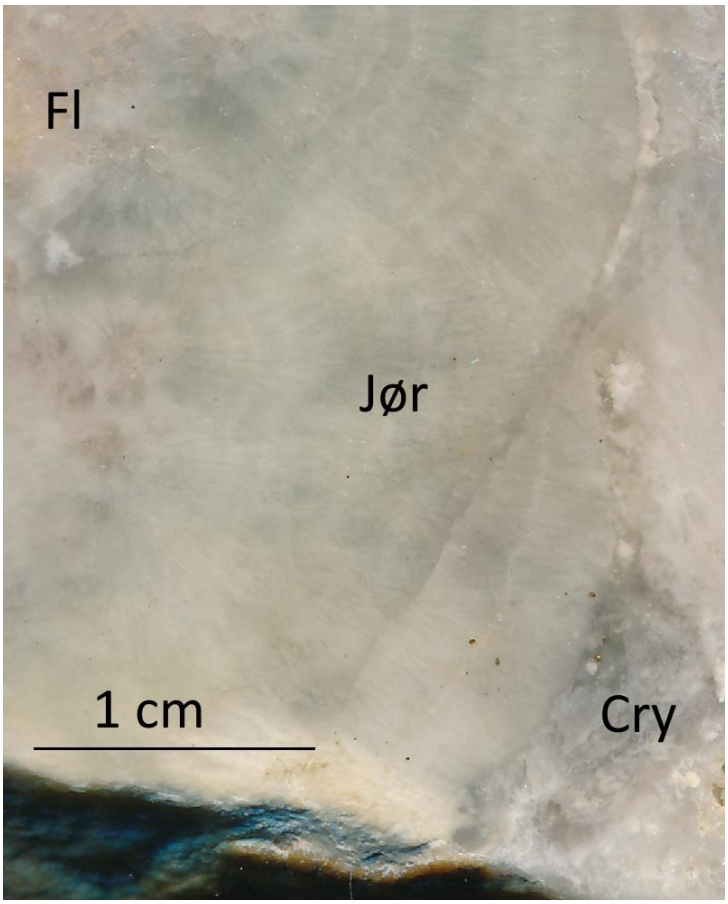

Figure AI-12: Presents a scan from which the thin section was made. Jør: Jørgensenite, Fl: Fluorite, Cry: Cryolite.

Sample PAD-IG013 to PAD-IG025

No thin sections were made from these samples, which means that the mineral assemblages of these samples remain somewhat enigmatic. These samples were mainly studied for their cavities and used as a source of jørgensenite and jarlite crystals for analysis with the SXRD.

When found in cavities, jarlite and jørgensenite occur in a similar manner as have been seen in the thin sections. They always occur as fan-shaped aggregates, and they are often found together with crystals of pachnolite/thomsenolite. Sample PAD-IG026 is different from the others, and jørgensenite is inferred to occur as massive intergrowths together with bøggildite (Bgg, the salmon-coloured mineral).

PAD-IG013

PAD-IG014

PAD-IG015

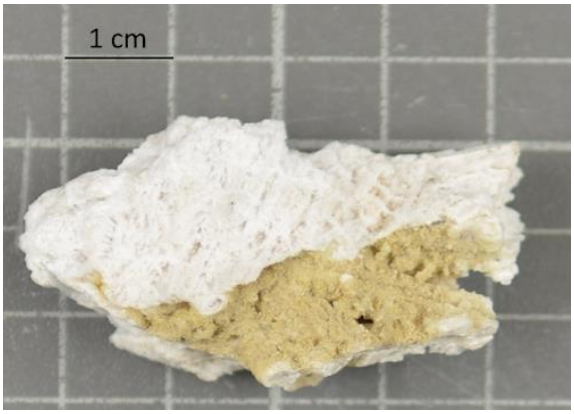

PAD-IG016

PAD-IG017

PAD-IG018

PAD-IG019

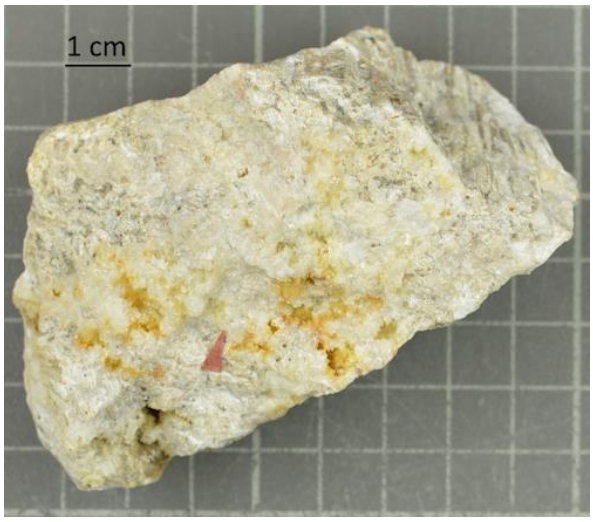

PAD-IG020

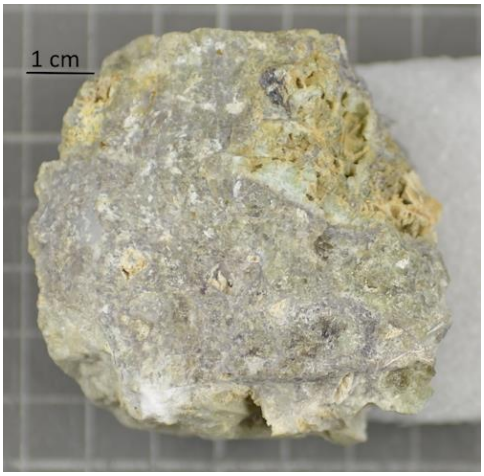

PAD-IG021

PAD-IG022

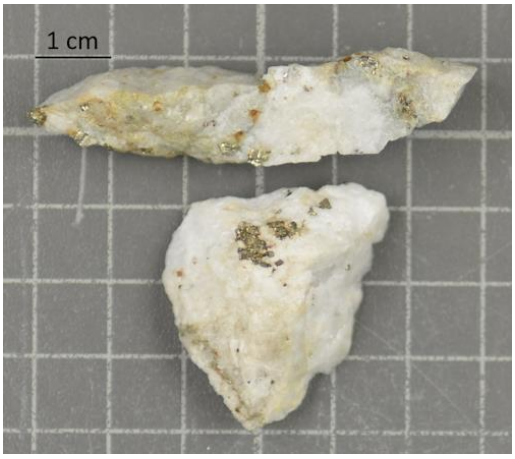

PAD-IG023

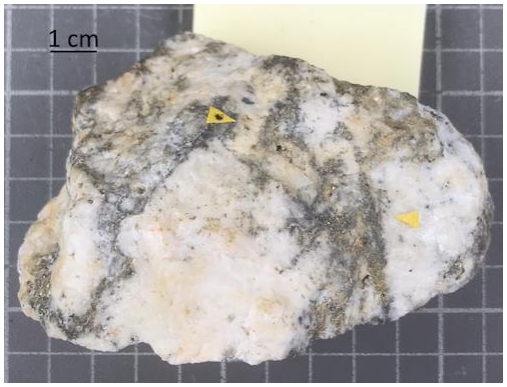

PAD-IG024

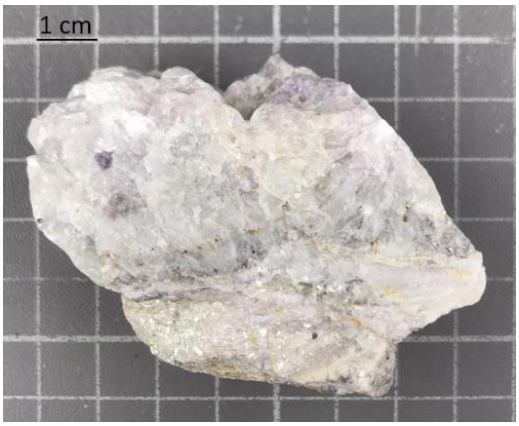

PAD-IG025

PAD-IG026

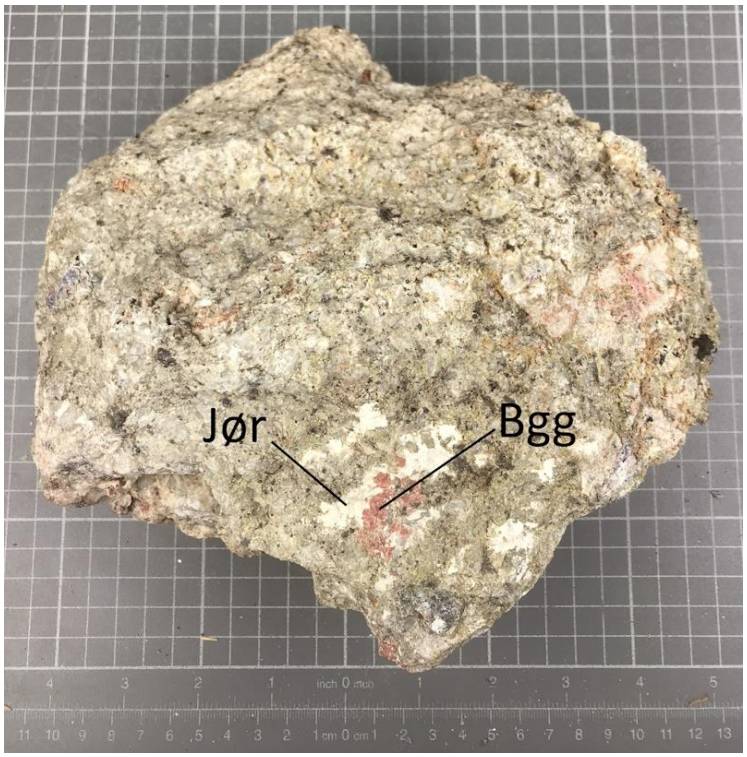

Appendix II: SXRD-settings

Table AII: SXRD-settings used when collecting crystal structure data

Mineral	Jør.	Jør.	Jør.	Jør.
Exp. Nr	557	711	729	730
Detector distance (mm)	34	34	40	34
Collection model	Hemisphere	Hemisphere	Hemisphere	Hemisphere
Exposure time (s)	25	15	20	7
Step (°)	0.3	0.3	0.3	0.3
Resolution (Å)	0.6	0.65	0.6	0.6
Redundancy	5	5	4.5	5
Temperature (K)	298	298	298	298

Table AII cont.: SXRD-settings used when collecting crystal structure data

Mineral	Jør.	Jør.	Jør.	Jar.
Exp. Nr	686	702	804	699
Detector distance (mm)	32	40	34	34
Collection model	Hemisphere	Sphere	Hemisphere	Hemisphere
Exposure time (s)	40	6	4	22
Step (°)	0.4	0.3	0.3	0.3
Resolution (Å)	0.65	0.6	0.6	0.7
Redundancy	3.5	3	5	-
Temperature (K)	298	298	298	298

Appendix III: Chemical Data

See the accompanying excel spreadsheet. Appendix III-1 contain the raw data collected from the EPMA. Appendix III-2 contain the raw data organized according to minerals. Appendix III-3 contain the *apfu*-values calculated from the raw data. Appendix III-4 contain the measured $^{87}Sr/^{86}Sr$-ratios from sample PAD-IG002, PAD-IG010, PAD-IG019 and PAD-IG022 as they were received from CELTIC, Cardiff University.

Appendix IV: Refinement data

Appendix IV-1 to Appendix IV-8 are the cif-files generated during crystal structure refinement. Be aware that, if these files are opened in VESTA, exp. 711, exp. 730 and exp. 804 are displayed with a different origin. The following origin shift transformations can be used, to display exp.711, exp. 730 and exp. 804 in accordance with a coherent origin of the unit cell:

Exp. 711: $\begin{pmatrix} 0 \\ 0 \\ 0.5 \end{pmatrix}$

Exp. 730: $\begin{pmatrix} 0.5 \\ 0 \\ 0 \end{pmatrix}$

Exp. 804: $\begin{pmatrix} 0.5 \\ 0 \\ 0.5 \end{pmatrix}$

The different origin of these experiments is due to some unidentified error but hold no implications towards the quality of the data, and the site-symmetry is identical to the other experiments.